UNIVERSITY OF CALIFORNIA
SANTA CRUZ

THE ROLE OF SEA ICE IN POLAR CLIMATE CHANGE: INVESTIGATING DISTINCT CAUSE-EFFECT RELATIONSHIPS IN EACH HEMISPHERE

A dissertation submitted in partial satisfaction of the
requirements for the degree of

DOCTOR OF PHILOSOPHY

in

EARTH AND PLANETARY SCIENCE

by

Zachary Snow Kaufman

December 2022

The Dissertation of Zachary Snow Kaufman
is approved:

Professor Nicole Feldl, Chair

Professor Patrick Chuang

Professor Christopher Edwards

Professor Claudie Beaulieu

Peter Biehl
Vice Provost and Dean of Graduate Studies

Table of Contents

List of Figures

List of Tables

Abstract

The Role of Sea Ice in Polar Climate Change: Investigating Distinct Cause-Effect Relationships in Each Hemisphere

by

Zachary Snow Kaufman

Earth's poles are uniquely sensitive to climate system perturbations; in recent decades, Arctic temperatures have warmed at twice the global average. Antarctic warming has been slower to emerge, but climate models project long-term changes in both polar regions, posing severe consequences for societies, ecosystems, and global weather patterns. Managing these consequences necessitates a detailed physical understanding of sea ice and its central role in governing the high-latitude energy budget. To address this need, my thesis investigates ice-ocean-atmosphere interactions in the polar regions. I quantify causal relationships among the physical processes shaping high-latitude climate, characterizing how sea ice both drives and responds to climate variability and change in each hemisphere. The results of my research provide physical insights towards more accurate climate models and guide future observations in these remote, data-sparse regions.

In Chapter Two (Kaufman et al. 2020), I study the relationship between Southern Ocean polynyas and high-latitude climate variability. These anomalous ice-free ocean regions, enclosed by the winter sea-ice pack, have been observed to occasionally release heat from the deep ocean to the overlying atmosphere. Yet, most standard resolution climate models represent these features poorly. I analyzed output from a fully coupled model that effectively simulates polynyas due to its

uniquely high-resolution seafloor bathymetry. I found that the reduction of surface heat fluxes during periods of full ice cover is not fully compensated by poleward heat transport. This imbalance increases ocean heat content, supplies polynya heat loss, and drives higher atmospheric temperatures. The results disentangle the complex processes that both enable polynyas' existence and respond to them, providing a robust physical description of these rare, but impactful, events. This research was conducted in collaboration with the Climate, Ocean, and Sea Ice Modeling (COSIM) group at Los Alamos National Laboratory, where the sea ice model is developed.

In Chapter Three (Kaufman and Feldl 2022), my research addresses polar climate dynamics in the Arctic, where I analyze the atmosphere's response to increased carbon dioxide concentrations. During polar winter, the Arctic's lower atmosphere warms more than the air aloft; this bottom-heavy vertical warming structure reduces radiative cooling to space and increases the regional climate sensitivity. However, the physical processes that set the warming structure have remained unclear. Using output from a 21st century warming simulation, I quantified the relative influence of various Arctic heating sources, identifying sea-ice loss as the dominant mechanism driving bottom-heavy winter warming. This interseasonal effect is mediated by changes in Arctic clouds and air-sea energy fluxes. By uncovering the causes of vertically non-uniform warming, my results provide key constraints on future Arctic climate change projections.

The final project of this thesis, Chapter Four, seeks to clarify what climate conditions enable the Warm Arctic-Cold Eurasia pattern, a notable feature of historical temperature observations. Observed Eurasian cooling is often attributed to sea-ice loss, implying an anthropogenic cause. However, comprehensive climate

change simulations do not produce Eurasian cooling, and the observational record is too short to rule out a role for unforced atmospheric variability. I reconcile this discrepancy by identifying atmospheric blocking over the Ural mountains as a robust driver of the Warm Arctic-Cold Eurasia pattern across a range of background climate states. By accounting for distinct transient responses to Ural blocking variability in observations and models, I am able to bring their seemingly divergent midlatitude temperature trends into agreement.

A common challenge in each of these projects is defining the routes of causality between coupled physical processes. I address this challenge with causal discovery techniques, which provide an alternative to computationally expensive model perturbation experiments. These statistical techniques identify causal mechanisms in any time series, observational or simulated, and were an essential component of my research approach. By integrating statistical reasoning with climate dynamics theory, I am able to advance understanding of the distinct complex systems comprising Earth's two polar regions.

To Segre,

My Home Through Thick and Thin

Acknowledgments

My journey into climate dynamics began in a rather surprising way. I'd spent my undergraduate years working as a geochemist, studying polar climate through the lens of marine sedimentology. But when I first visited UCSC, Nicole showed me a video loop of the atmospheric circulation, a beautiful visual that I come back to over and over again. I also learned about the power of models as tools to understand the climate system. I was sold, and decided to begin my PhD studying Earth's climate with computational models, a world that was comparatively new to me. I am thankful that the EPS department had the confidence in me to make this pivot, allowing me to pursue my curiosities and venture into a new field of research.

Nicole's dedication as a research mentor has empowered me in so many ways as a scientist. The physical concepts and research tools for climate modeling were unfamiliar to me at first, but her guidance in weekly meetings helped me hit the ground running. She immediately identified that my scientific intuition was well-suited for statistical analysis, and encouraged me to use this intuition to develop new research methods. Still, I was always reminded to never lose sight of the geophysical theory that laid the groundwork of my scientific understanding. Most importantly, Nicole's feedback and dedication to quality research was never overly prescriptive, and I was always given the freedom and encouragement to think creatively and chart my own research path.

Patrick, Chris, and Claudie have been great committee members. In particular, the classes they taught were an invaluable resource for my research. Claudie's time series analysis expertise helped me refine my methods. Chris's geophysical

fluid dynamics course demystified many mathematical concepts for me. And I've always appreciated Patrick's reminders to have a healthy skepticism of climate model output, especially when it comes to clouds. Outside the lab, I must also note my appreciation for Patrick's culinary expertise. His restaurant blog is incredible, and thanks to him I will never forget the important table etiquette and techniques for eating good ramen.

My Department of Energy collaborators, Wilbert Weijer and Milena Veneziani, have been an important part of my PhD journey. Though we only worked in-person together at Los Alamos National Laboratory for three months, they've included me in their high-latitude research projects to this day, for which I am grateful. The more recent years of my PhD were also graced by a growing team of atmospheric scientists, with Mark England, Hayes Devaney, and Po-Chun Chung joining the lab. It was great to be able to test my research talks and ideas on them each week, and to be inspired by their fresh perspectives. I am also thankful that I was able to team up with Mason Leandro when travelling to conferences. Though our fields of research were quite different, he has always been a trustworthy partner that made the chaos of conference centers much easier (and fun) to be a part of.

During my PhD, I spent over five years living with other UCSC graduate students. Colleen Murphy, Szilard Gyalay, Coby Abrahams, Kelian Dascher-Cousineau, Calvin Munson, Araceli Serrano, Susan Pit, Alba Rodriguez, and Jake Tidwell are brilliant scientists, but more importantly, they've been my friends through thick and thin, and we endured many challenges, including a global pandemic, together. Additionally, my mountain bike buddies, Cory, Jeff, and Joe, will always be near and dear to my heart as highlights of my time in Santa Cruz.

None of this would've been possible without my family. Mom, Dad, and Kona were always by my side, through the highs and lows, to motivate and encourage me. And lastly, Tracey, my best friend. Your love and support means more than I can possibly put into words, and I can't wait to see what adventures we embark on next.

Previously published material:

The text of this dissertation includes reprints of the following previously published material:

Chapter Two: Kaufman, Zachary S., Nicole Feldl, Wilbert Weijer, and Milena Veneziani. "Causal interactions between Southern Ocean polynyas and high-latitude atmosphere–ocean variability." Journal of Climate 33, no. 11 (2020): 4891-4905.

Chapter Three: Kaufman, Zachary S., and Nicole Feldl. "Causes of the Arctic's Lower-Tropospheric Warming Structure." Journal of Climate 35.6 (2022): 1983-2002.

Chapter 1

Introduction

The trajectory of anthropogenic climate change is often framed in terms of global mean warming. This framing is reflected in international policy goals, such as the Paris Climate Accord, which seek to limit global mean warming below a certain target threshold (e.g. less than 2°C by 2100). However, climate change impacts and risks are not evenly distributed across the globe. In particular, Earth's spatial pattern of warming is polar amplified: For a given change in atmospheric CO_2, the associated radiative forcing on Earth's surface tends to produce larger temperature changes at the poles than at lower latitudes. Polar amplification is a fundamental feature of climate change, seen in observations (England et al. 2021), future projections (Holland and Bitz 2003), and paleoclimate records (Masson-Delmotte et al. 2006). To better understand this important phenomenon, my thesis work studies polar climate change and variability, focusing on sea ice and its coupled interactions with the atmosphere and ocean.

The importance of sea ice for producing polar-amplified warming has been recognized since the earliest studies of the greenhouse effect. Arrhenius (1896),

for instance, predicted polar-amplified warming would result from increased atmospheric CO_2 due to the albedo effects of retreating ice cover. This consequence of sea-ice retreat, now commonly referred to as the ice-albedo feedback, drives stronger surface absorption of solar radiation in the polar regions during summer, causing additional warming. Since the advent of general circulation models in the twentieth century, climate change simulations have also highlighted sea-ice warming impacts in winter, when little solar radiation reaches the poles (Manabe and Stouffer 1980). Under such conditions, sea ice acts as an insulator, decoupling the cold polar atmosphere from the relatively warm underlying ocean. As a result, newly exposed ocean can become an additional heat source to the polar atmosphere in the cold seasons.

Despite these well-established insights, many scientific challenges continue to hamper high-latitude climate predictability. Due to its remoteness, observations of many polar climate features, such as sea-ice extent, are restricted to approximately forty years of reliable satellite data, making it difficult to distinguish externally forced trends from internal variability. Relatedly, climate model simulations feature persistent biases in the polar regions, struggling to represent key observed features of the high-latitude system. For instance, climate models do not simulate opposing trends in Antarctic and Arctic sea ice observed over recent decades, which could relate to biases in thermohaline properties and/or wind stress changes in the Southern Ocean (Purich et al. 2016). The non-local, non-linear interactions between atmosphere, ocean, and sea ice also make it difficult to isolate individual processes' contribution to polar-amplified warming, leading to large uncertainty in future projections. Addressing these challenges are a central theme of my thesis work.

In Chapter Two, I investigate variability in Antarctic sea ice. Unlike the Arctic, signals of polar amplification have yet to robustly emerge in observed Antarctic sea-ice trends. This hemispheric asymmetry can be partially be attributed to the ocean's meridional overturning circulation in the high-latitude Southern Ocean, where wind-driven upwelling of unmodified water from depth is expected to delay warming throughout the region (Armour et al. 2016). However, delayed warming alone cannot explain recent Antarctic sea-ice variability, such as its weak positive trend from 1979-2011, or the subsequent abrupt decline in 2016 (Meehl et al. 2019). Moreover, climate change simulations suggest that Southern Hemisphere sea-ice retreat should have already emerged in the historical period, contradicting observations (Turner and Comiso 2017). Clarifying the dominant mechanisms controlling observed Antarctic sea-ice variability is therefore needed. My Southern Hemisphere research seeks to characterize deep convection events, which sporadically ventilate the Southern Ocean's deep-ocean heat reservoir through large openings in the winter sea-ice pack known as open-ocean polynyas. I make use of recently developed high-resolution modeling capabilities, which resolve these elusive sea-ice features with unprecedented realism. Open-ocean polynyas are rare, but impactful events that lend insight into the modes of Southern Ocean circulation variability that could be operating alongside anthropogenic forcing.

In Chapters Three and Four, I turn my attention to the Arctic, the most rapidly warming region on the planet. Along with the aforementioned ice-albedo feedback, polar amplification in the Arctic is often attributed to changes in poleward atmospheric heat transport, as well as the the positive lapse rate feedback, which is associated with climatological boundary-layer temperature inversions in the Arctic

atmosphere (Pithan and Mauritsen 2014). Uncertainty in the magnitude of Arctic climate feedbacks arises because these processes do not operate independently, and their interactions are a key driver of divergent Arctic warming projections (Roe et al. 2015). In Chapter Three, I use a set of twenty-first century climate change simulations to disentangle these Arctic warming mechanisms, assessing the relative contributions of sea-ice loss and heat transport changes for setting the Arctic atmosphere's vertical warming structure.

The consequences of Arctic-amplified warming may extend beyond the high latitudes. Recent climate studies have highlighted the hypothesis that Arctic sea-ice loss alters the midlatitude atmospheric circulation, leading to more frequent extreme weather events over the densely populated Northern Hemisphere continents (Barnes and Screen 2015). The socioeconomic implications of this proposed Arctic-midlatitude connection are substantial, but scientific consensus on its existence has not been reached. In particular, modeling studies often suggest that the influence of sea-ice loss on midlatitude weather is indistinguishable from natural climate variability (Cohen et al. 2020). In Chapter Four, I seek to reconcile these divergent interpretations, where I develop a statistical tool that enables direct comparison of Arctic-midlatitude interactions in models and observations.

Policymakers' ability to manage the consequences of polar climate change, from rising sea levels to changing weather patterns, is dependent on improving regional climate predictability. In the Arctic, rapidly declining sea ice exposes new economic resources and shipping routes, necessitating a detailed understanding of where and how quickly newly open water will appear. In the Antarctic, the instability-prone West Antarctic Ice Sheet may have large future contributions to sea-level

rise, but predicting the timing and magnitude of ice sheet melt requires a better understanding of how Antarctic warming trends will progress. The research detailed in this thesis advances our physical understanding of the polar regions, providing scientific contributions to reduce these important uncertainties.

Chapter 2

Causal Interactions Between Southern Ocean Polynyas and High-Latitude Atmosphere-Ocean Variability

This chapter is a slightly modified reprint of work previously published as Kaufman, Zachary S., Nicole Feldl, Wilbert Weijer, and Milena Veneziani. "Causal interactions between Southern Ocean polynyas and high-latitude atmosphere–ocean variability." Journal of Climate 33, no. 11 (2020): 4891-4905.

Abstract

Weddell Sea open-ocean polynyas have been observed to occasionally release heat from the deep ocean to the atmosphere, indicating that their sporadic appearances may be an important feature of high-latitude atmosphere–ocean variability. Yet, observations of the phenomenon are sparse and many standard-resolution

models represent these features poorly, if at all. We use a fully coupled, synoptic-scale preindustrial control simulation of the Energy Exascale Earth System Model (E3SMv0-HR) to effectively simulate open-ocean polynyas and investigate their role in the climate system. Our approach employs statistical tests of Granger causality to diagnose local and remote drivers of, and responses to, polynya heat loss on inter-annual to decadal time scales. First, we find that polynya heat loss Granger causes a persistent increase in surface air temperature over the Weddell Sea, strengthening the local cyclonic wind circulation. Along with responding to polynyas, atmospheric conditions also facilitate their development. When the Southern Ocean experiences a rapid poleward shift in the circumpolar westerlies following a prolonged negative phase of the southern annular mode (SAM), Weddell Sea salinity increases, promoting density destratification and convection in the water column. Finally, we find that the reduction of surface heat fluxes during periods of full ice cover is not fully compensated by ocean heat transport into the high latitudes. This imbalance leads to a buildup of ocean heat content that supplies polynya heat loss. These results disentangle the complex, coupled climate processes that both enable the polynya's existence and respond to it, providing insights to improve the representation of these highly episodic sea ice features in climate models.

2.1 Introduction

Shortly after passive microwave satellite observations began in the 1970s, a large region of open ocean appeared for three consecutive winters in a typically ice-covered region of the Weddell Sea (Carsey 1980). These anomalous ice-free

regions enclosed by the winter sea-ice pack have since come to be known as open-ocean polynyas. The initial observation in the Weddell Sea ranged in size from $2-3\times10^5$ km^2 from 1974-1976 and was maintained by a heat supply from sustained ocean convection reaching depths of up to 3000 m (Gordon 1982). Reanalysis-based reconstructions of the Weddell polynyas have shown that the tapping of the deep-ocean heat reservoir, combined with intense air-sea interaction over the anomalously ice-free ocean, delivered large quantities of heat to the atmosphere (Moore et al. 2002). More recent wintertime observations of smaller polynyas over the Maud Rise seamount during 2016 and 2017 illustrate that these sea-ice features can be influenced by high-latitude atmospheric circulation anomalies and strong polar cyclones over the Weddell Sea (Francis et al. 2018; Jena et al. 2019; Cheon and Gordon 2019; Campbell et al. 2019). While both the 1974-1976 and 2016-2017 events demonstrate connections between deep convection and interannual high-latitude climate variability, observations of open-ocean polynyas in the Southern Hemisphere high latitudes are still sparse. Important questions remain regarding how polynya heat loss may have influenced the atmosphere before satellite observations began, as well as how their seemingly rare appearances may relate to current and future high-latitude climate.

Recent multidecadal trends in the Southern Ocean are in stark opposition to the precipitous sea-ice decline occurring simultaneously in the Arctic. From 1979-2011, Antarctic sea-ice extent exhibited a positive trend and sea surface temperatures (SSTs) around the continent decreased (Fan et al. 2014). The surface cooling trend reversed in 2016, associated with anomalous atmosphere-ocean variability (Meehl et al. 2019; Wang et al. 2019). This trend reversal seems to coincide

with the reappearance of an open-ocean polynya in winters of 2016 and 2017, though a clear, physical link between these phenomena has not yet been established. The warming response to anthropogenic greenhouse gas forcing is expected to be delayed in the near-surface Southern Ocean south of the Antarctic Circumpolar Current (Armour et al. 2016). However, the mechanisms underlying the observed SST cooling trend remain unclear; in the region, many historical hindcast simulations feature a warming bias relative to observations during this recent time period (Kostov et al. 2018). This hemispheric asymmetry necessitates a better understanding of Southern Ocean variability, including variability associated with polynya heat loss, that could be operating alongside global anthropogenic forcing.

Both natural climate variability and anthropogenic trends have been suggested to influence ocean, ice, and atmospheric conditions that, in turn, control polynyas and deep convection in the Southern Ocean. For instance, under preindustrial conditions, several climate model simulations feature natural oscillations in deep convection on centennial timescales (Latif et al. 2013; Martin et al. 2013; Cabré et al. 2017). When convection is absent, annual-mean surface air temperature and SST decrease across the Southern Ocean. The absence of polynyas in recent decades may also be related to externally forced variability. For instance, the Southern Ocean surface has undergone a recent freshening trend, which inhibits convective mixing and polynyas by stratifying the water column. The freshening has been related to increased melting from Antarctic glaciers (Bintanja et al. 2015), an intensification of the global hydrological cycle (Durack et al. 2012), and increased precipitation from a positive trend in the Southern Annular Mode (SAM) since 1979 (Gordon et al. 2007). However, the connection between SAM variability and high-

latitude precipitation has since been questioned (Spensberger et al. 2020). Furthermore, recent observations have suggested that positive SAM anomalies can instead promote deep convection through enhanced wind-driven upwelling of high-salinity water in the Weddell Sea (Campbell et al. 2019). The connection between observed, externally forced surface freshening and the reduction of deep convection is supported by trends in the Coupled Model Intercomparison Project phase 5 (CMIP5). Of the 36 CMIP5 models examined in De Lavergne et al. (2014), the 25 models that feature Southern Ocean deep convection become increasingly stratified as the sea surface freshens under anthropogenic forcing. Convection ceases fully in all of the initially convective models by the year 2300.

Despite these insights into high-latitude ocean dynamics, until very recently, fully coupled models have lacked the resolution to explicitly resolve open-ocean polynyas that are spatially or temporally consistent with observations. This shortcoming is an important obstacle to understanding how the ocean, atmosphere, and sea ice interact in the Southern Hemisphere. Models vary widely in their representation of Southern Ocean deep convection, both spatially and temporally (De Lavergne et al. 2014), which may influence the degree to which sea ice and SST respond to anthropogenic freshwater forcing (Armour and Bitz 2015). Inconsistent representation of deep convection may also affect atmospheric variability, since the amount of anomalously open water during austral winter will impact the magnitude of air-sea heat flux (Moore et al. 2002). Our study seeks to improve understanding of coupled high-latitude climate processes by placing emphasis on polynyas and their interaction with the atmosphere. We analyze these interactions in the context of the long-term buildup of the deep ocean heat reservoir, which preconditions the

Southern Ocean for deep convection.

Advances in state-of-the-art modeling capabilities have provided new opportunities to study polynya heat loss. Recently, a fully-coupled synoptic-scale preindustrial control simulation of the Energy Exascale Earth System Model version v0.1 (E3SMv0) has effectively resolved Weddell Sea open-ocean polynyas that are consistent with observations in their spatial extent and location. Prior research with this model has addressed the preconditioning requirements for Maud Rise polynyas (Kurtakoti et al. 2018), while results from a similar Community Earth System Model (CESM) configuration (Small et al. 2014) have addressed the local atmospheric response (Weijer et al. 2017). Our research builds on this previous work through a larger scale investigation: we use polynya heat loss as a metric to investigate high-latitude climate variability through coupled ocean-ice-atmosphere interactions. We draw connections between polynya heat loss variability and three important climate processes in the Southern Hemisphere mid/high-latitudes: (i) surface temperature and heat flux anomalies, (ii) the zonal wind pattern over the Weddell Sea, and (iii) the poleward transport of heat and its partitioning between the atmosphere and the ocean. We show that all three processes are significantly impacted by polynya heat flux variability, highlighting the importance of correctly resolving these highly episodic features as models gain higher resolution.

We address the challenge of determining causality in coupled systems, where feedback processes are often present. Along with impacting the atmosphere, polynyas can themselves be influenced by atmospheric processes. For instance, idealized simulations have induced Weddell Sea polynya formation by applying additional westerly wind-stress forcing, resulting in a spin-up of the Weddell Gyre (Cheon et al.

2014; Cheon et al. 2018). Such modeling experiments preclude a wind response to polynyas. We instead assess coupled processes through the statistical framework of Granger causality. This statistically robust tool can identify causal relationships in any time series, observational or simulated. It also accounts for memory in the climate system, an important consideration when performing lagged regressions with geophysical time series (McGraw and Barnes 2018). In this framework, the word "causality" strictly refers to quantifying statistical predictability, rather than true causality. The method is nonetheless useful for disentangling drivers from responses in ocean-ice-atmosphere interactions. Following prior work in the Arctic (Matthewman and Magnusdottir 2011; Kretschmer et al. 2016; Samarasinghe et al. 2018), we analyze the degree to which Weddell Sea polynyas drive and/or respond to climate variability in a comprehensive setting, enabling new insights into the elusive role that Weddell Sea convection can have in the high-latitude climate system.

2.2 Methods

A high resolution configuration of the E3SMv0 model (E3SMv0-HR) was run for 131 years under fixed radiative forcing conditions representative of the year 1850. The ocean component is the Parallel Ocean Program, version 2 (POP2), configured at a nominal 0.1° resolution. It is coupled to a sea-ice model component at the same resolution, the Los Alamos Sea-Ice Model version 4 (CICE4). The atmosphere component is the Community Atmosphere Model, version 5 (CAM5), configured at a nominal 0.25° resolution. The land component is the Community Land Model, version 4.5 (CLM4.5), configured using the same grid as the atmosphere

model. All fields considered in this study were saved as monthly averages. Notably, we find that a companion run at 1° ocean and atmosphere resolutions does not simulate strong open-ocean convection.

In E3SMv0-HR, we define an open-ocean polynya as a fully enclosed region of ice-free ocean (sea-ice fraction less than 15%) that persists through all 3 months of maximum sea-ice extent in the Southern Hemisphere: August, September, and October (ASO). By this definition, 52 out of 127 years (41%) in the E3SMv0-HR simulation feature open-ocean polynyas, a more common occurrence than what is seen in the observational record. That said, episodes of major Weddell Sea polynyas are interspersed by periods of stronger stratification that persist for many decades, matching the post-1976 drought of Weddell Sea polynyas. Our simulation therefore differs from the convecting CMIP5 models that exhibit chronically weak stratification in the Weddell Sea, where mean September mixed-layer depths often exceed 2000 m (De Lavergne et al. 2014). Both the location and spatial extent of the simulated polynyas agree well with observations to date. The polynyas form exclusively in the Weddell Sea, centered around the location of the Maud Rise seamount (65°S, 2.5°E), with a median size of 1.71×10^5 km^2, approximately 68% of the mean polynya area observed during the 1974-1976 event. Smaller open-ocean polynyas with an area on the order of 10^4 km^2, comparable in size to the open-ocean polynyas observed in 2016 and 2017, appear sporadically in the first four decades of the simulation (e.g., years 24-27, 31-35). The simulation's larger polynyas propagate westward through the Weddell Sea, occurring consecutively in three distinct episodes associated with deep ocean convection, each lasting 10-15 years. These episodes also feature patches of open water that extend to the sea-ice edge, forming large em-

bayments. These features do not meet the conventional definition of an open-ocean polynya; embayments are larger, not fully enclosed by sea-ice, and have not been seen observationally in austral winter. However, in E3SMv0-HR, they appear to be driven by the same convective process and release heat to the atmosphere in a similar manner as polynyas. Thus, given the necessity of continuous time series and the utility of a binary classification, we classify the 52 years containing polynyas and/or embayments as "polynya years" through visual inspection, and classify the remaining 80 years as "non-polynya years".

After identifying open-ocean polynyas, we relate their occurrence to several metrics of the high-latitude energy budget. Upward surface heat flux (F) for a given year is defined as the ASO averaged sum of the turbulent and radiative heat fluxes: net shortwave radiative flux ($FSNS$), net longwave radiative flux ($FLNS$), latent heat flux ($LHFLX$), and sensible heat flux ($SHFLX$) in units of W m^{-2}:

$$F = SHFLX + LHFLX + FLNS - FSNS \tag{2.1}$$

where $SHFLX$, $LHFLX$, and $FLNS$ are positive upward, $FSNS$ is positive downward, and the $LHFLX$ term is modified to account for the latent heat of fusion from frozen precipitation. Accordingly, the sum of these terms is positive when heat is lost from the ocean and taken up by the atmosphere. F is calculated for each grid cell. We isolate the seasonal quantity since open-ocean polynyas are only active during the months of maximum sea-ice extent in the Southern Hemisphere.

The mean state of poleward heat transport in the atmosphere (AHT) and ocean (OHT) is quantified as a function of latitude. We follow the convention of northward transport defined as positive, and southward transport defined as nega-

tive (e.g., Trenberth and Caron 2001). AHT is calculated as the meridional cumulative integral of the top-of-atmosphere radiative heat flux (F_T, positive downward) and surface heat flux (F, positive upward):

$$AHT(\phi, t) = 2\pi R_e^2 \int_{-\pi/2}^{\phi} ([F_T] + [F]) \cos(\phi) d\phi' \tag{2.2}$$

where both flux terms are calculated as zonal means (denoted by brackets), ϕ is latitude, and R_e is the Earth's radius. On the timescales relevant to our study, we assume atmospheric heat storage is negligible.

While the effective ocean heat transport is commonly calculated as a residual between the total and atmospheric transport, it does not allow for a proper diagnosis of heat transport and storage. In particular, the timescale of variability in OHT changes when considering heat storage. This consideration is important for time series analysis of the heat transport components, as well as diagnosing the relative response times of the atmosphere and ocean to a perturbation, such as the occurrence of an open-ocean polynya. Therefore, rather than use the cumulative sum formulation of Equation 2.2, we explicitly calculate OHT at each latitude as:

$$OHT(\phi, t) = R_e \cos(\phi) \int_{z_{bot}}^{0} \int_{0}^{2\pi} \rho c_p \theta V \, dz d\lambda \tag{2.3}$$

where the integration is carried out over the total ocean depth ($z_{bot} < z < 0$) and longitude (λ), ρ is seawater density (10^3 kg m^{-3}), c_p is specific heat of seawater at constant pressure (3850 J kg^{-1}K^{-1}), θ is the ocean potential temperature, and V is the ocean meridional velocity. The product θV is a diagnostic variable that is calculated at every model timestep and saved as monthly averages.

To supplement our analysis of ocean heat transport, we additionally infer ocean heat content south of a latitude band as the difference between ocean heat transport (OHT, positive northward) and the meridional cumulative integral of surface heat flux (F, positive upward), where both terms are integrated over time:

$$OHC(\phi, t) = -\int_0^t OHT(\phi, t)dt' - 2\pi R_e^2 \int_0^t \int_{-\pi/2}^{\phi} [F]\cos(\phi)d\phi' dt' \tag{2.4}$$

Finally, we diagnose two-way predictive causality between polynya heat loss and the climatic processes of interest, combining a vector autoregressive model framework with Granger causality. The general equation for a bivariate (n=2), lag-one vector autoregressive (VAR-1) model can be written as:

$$\begin{bmatrix} y_{1,t} \\ y_{2,t} \end{bmatrix} = \begin{bmatrix} c_1 \\ c_2 \end{bmatrix} + \begin{bmatrix} a_{1,1} & a_{1,2} \\ a_{2,1} & a_{2,2} \end{bmatrix} \begin{bmatrix} y_{1,t-1} \\ y_{2,t-1} \end{bmatrix} + \begin{bmatrix} e_{1,t} \\ e_{2,t} \end{bmatrix} \tag{2.5}$$

where $y_{n,t}$ are stationary time series of endogenous predictor/response variables, c_n are the model intercepts, $a_{n,n}$ are regression coefficients, and $e_{n,t}$ are independent, identically distributed error terms, calculated as the residual difference between observed and expected values of $y_{n,t}$. Though VAR models can generally accommodate more than 2 variables, we solely conduct bivariate analyses, as in Equation 2.5. Other causal inference techniques are better adapted to connecting larger numbers of variables in a single model (Runge et al. 2017) and our bivariate approach offers the advantage of simple, straightforward interpretability.

VAR model analysis requires stationary time series. To fulfill this requirement in each variable, we subtract the climatological mean for each month in the seasonal cycle and divide by the entire time series' standard deviation. Any long-

term linear trend is removed. After applying these changes, each time series represents normalized climatological anomalies, and parameters $a_{n,n}$, c_n can be solved using ordinary least-squares estimation. As a simple example, Equation 2.5 has a maximum lag, or lag order, of 1 timestep. However, in our analysis, the optimal maximum lag order is determined statistically by the Akaike Information Criterion (AIC). The AIC is a measure of relative log-likelihood, and is calculated for each model over 1,2, ... $12\,(t_{max}/100)^{1/4}$ possible maximum lag orders, where t_{max} is the length of the time series. The lag-order that minimizes the AIC is selected as the best fit and used for subsequent analysis. Our formulation in Equation 2.5 focuses on lagged relationships and does not allow for instantaneous connections.

Following the framework of Samarasinghe et al. (2018), we then use our VAR model to test for Granger causality between each variable, in both directions. To accomplish this task, we designate a restricted model and unrestricted model for each response variable in $y_{n,t}$, utilizing different subsets of the parameters in the pre-fitted VAR model (Eq. 2.5) . The restricted model is an autoregression of the response variable against itself (Eq. 2.6), and the unrestricted model is a multiple linear lagged regression of the response variable against both itself and the predictor variable (Eq. 2.7):

$$y_1'(t) = c_1 + \sum_{i=1}^{\infty} a_{1,1,i}(y_1(t-i)) \tag{2.6}$$

$$y_1''(t) = c_1 + \sum_{i=1}^{\infty} a_{1,1,i}(y_1(t-i)) + \sum_{i=1}^{\infty} a_{1,2,i}(y_2(t-i)) \tag{2.7}$$

where i denotes individual lags, and the single/double apostrophes on the

L.H.S. distinguish restricted/unrestricted predicted values from observed values. In the case of Equation (2.7), $y_2(t)$ can be said to Granger cause $y_1(t)$ if two conditions are fulfilled:

1. At least one regression coefficient of the predictor, $y_2(t)$, must be significant according to a two-sided t test.

2. The unrestricted model must be able to explain more variance in $y_1(t)$ than the restricted model, according to an F-test on the residuals.

If the null hypothesis of no Granger causality is rejected at the 5 percent level, the sign and magnitude of the predicted anomalies in $y_1(t)$ can be found using the sum of $y_2(t)$'s regression coefficients. As an example, let Equation 2.7 be produced from a VAR-12 model with $i = 1$ month and $a_{1,2,1} + a_{1,2,2} + ...a_{1,2,12} = 0.5$. If Granger causality exists, then a one standard deviation anomaly in $y_2(t)$ predicts a 0.5 standard deviation anomaly in $y_1(t)$. To test Granger causality in the other direction, one simply exchanges the place of $y_1(t)$, $y_2(t)$, and their coefficients in Equations 2.6 and 2.7. We present results from bivariate VAR models regressing polynya heat loss with surface temperature, zonal near-surface wind, mixed-layer salinity, atmospheric heat transport, and ocean heat transport.

2.3 Results

2.3.1 Changes in Atmospheric Surface Properties

We analyze changes in the ocean-to-atmosphere surface heat flux (F) by calculating the ASO composite difference between polynya years and non-polynya

years (Fig. 2.1a). Poleward of the ASO climatological sea-ice edge, the Weddell Sea features a significant increase in upward surface heat flux during polynya years, with an average 12 W m^{-2} increase in the region where open-ocean polynyas occur. This region is denoted by the polynya mask in Fig. 2.1 and subsequent visualizations, calculated as the area where an open-ocean polynya occurs at least once in the simulation (embayments not included). The mask's surface area (3.9×10^6 km^2) is larger than the simulation's largest polynya (6.6×10^5 km^2). Accordingly, the mask's shape reflects the year-to-year spatial variability in large polynyas as they propagate westward from the Maud Rise region.

The increase in heat loss over the Weddell Sea is also accompanied by a decrease of similar magnitude, north/northeast of the climatological sea-ice edge. These two opposing changes have statistical significance primarily in the Atlantic/Indian Ocean sectors. The mechanism underlying this poleward shift in the surface heat flux, as well as its relationship to meridional heat transport, are analyzed in sections 2.3.2 and 2.3.3.

To compare how the turbulent and radiative components comprising F (Eqn. 2.1) contribute to these changes, we next calculate the composite difference for the turbulent sensible and latent heat fluxes only (Fig. 2.1b). Both the magnitude and spatial pattern of the composite difference are similar to what is seen in Figure 2.1a, indicating that the turbulent heat fluxes are the primary contributors to polynya heat loss. Sensible and latent turbulent fluxes each contribute roughly 10 W m^{-2} to the average anomaly over the polynya mask in Figure 2.1b. The small differences that exist between Figure 2.1a and Figure 2.1b are explained by enhanced shortwave absorption during polynya years, which damps ocean heat loss

south of the sea-ice edge. As turbulent fluxes transfer heat from the ocean to the atmosphere, sea-ice fraction and surface albedo decrease in and around the polynya, thus allowing more shortwave radiation to be absorbed at the surface. At all locations, the difference in net longwave radiative flux is negligible. This somewhat counterintuitive result is consistent with prior work using a similar model. Weijer et al. (2017) found that an increase in upward longwave radiation over a polynya is balanced by an equivalent increase in downwelling longwave radiation, which is associated with a warmer, moister atmosphere over polynyas and an optically thicker cloud deck.

Figure 2.1c shows the composite difference in ASO-average surface temperature between polynya years and non-polynya years. In the months of maximum sea-ice extent, there are large, significant temperature increases of 10-12 K over the entirety of the Weddell Sea region where polynyas occur. In general, the largest differences occur poleward of the sea-ice edge, but smaller increases appear throughout the Southern Ocean, extending northward up to 40°S. These changes are also statistically significant in the smaller, annual mean composite difference (not shown), where the maximum temperature change is 3K. In the Weddell Sea, this temperature change is consistent with prior analysis of open-ocean convection in a lower-resolution simulation (Cabré et al. 2017). In both the ASO-average and the annual average, significant differences in surface temperature are more spatially extensive than the significant differences in ocean heat loss. Furthermore, polynya years consistently show an increase in surface temperature in all regions where a significant difference is found.

The polynya mask region straddles the border between the prevailing mid-

latitude westerlies (positive U) and the much weaker polar easterlies (negative U). Figure 2.1d shows that, in the Weddell Sea sector, both midlatitude westerlies and polar easterlies undergo a significant increase in speed during polynya years. It is worth noting that large-scale, albeit not statistically significant, composite differences in wind speed also exist outside the Weddell Sea. In polynya years, midlatitude westerlies exhibit a poleward shift in the East Pacific/Atlantic sectors and an equatorward shift in the Indian/West Pacific sectors.

2.3.2 Granger causality Between Polynya Heat Loss, Surface Temperature, Wind, and Mixed-Layer Salinity

In the previous section, we determine concurrent relationships between polynya heat loss, surface temperature, and near-surface zonal wind. However, the system is complex and strongly coupled, obscuring the direction of causality. In this section, we use a combination of bi-variate vector autoregressive (VAR) models and Granger causality to explore the time-lagged causal relationships that can exist between these processes. The spatial maximum of ocean heat loss (F) in the Weddell Sea motivates the additional definition of polynya heat loss (F_p) as the spatial average of F within the polynya mask. Since the maximum increase is centered over the polynya mask, F_p can be used as a time series that characterizes the heat loss attributable to open-ocean polynyas. Autocorrelation and coupling between surface temperature and polynya heat loss are explored with a Granger-VAR approach. In each grid cell, we design a bi-variate vector autoregressive (VAR) model between surface temperature (T_s) and our index time series F_p. Here, both time series have monthly resolution. After building the statistical models, a Granger causality test

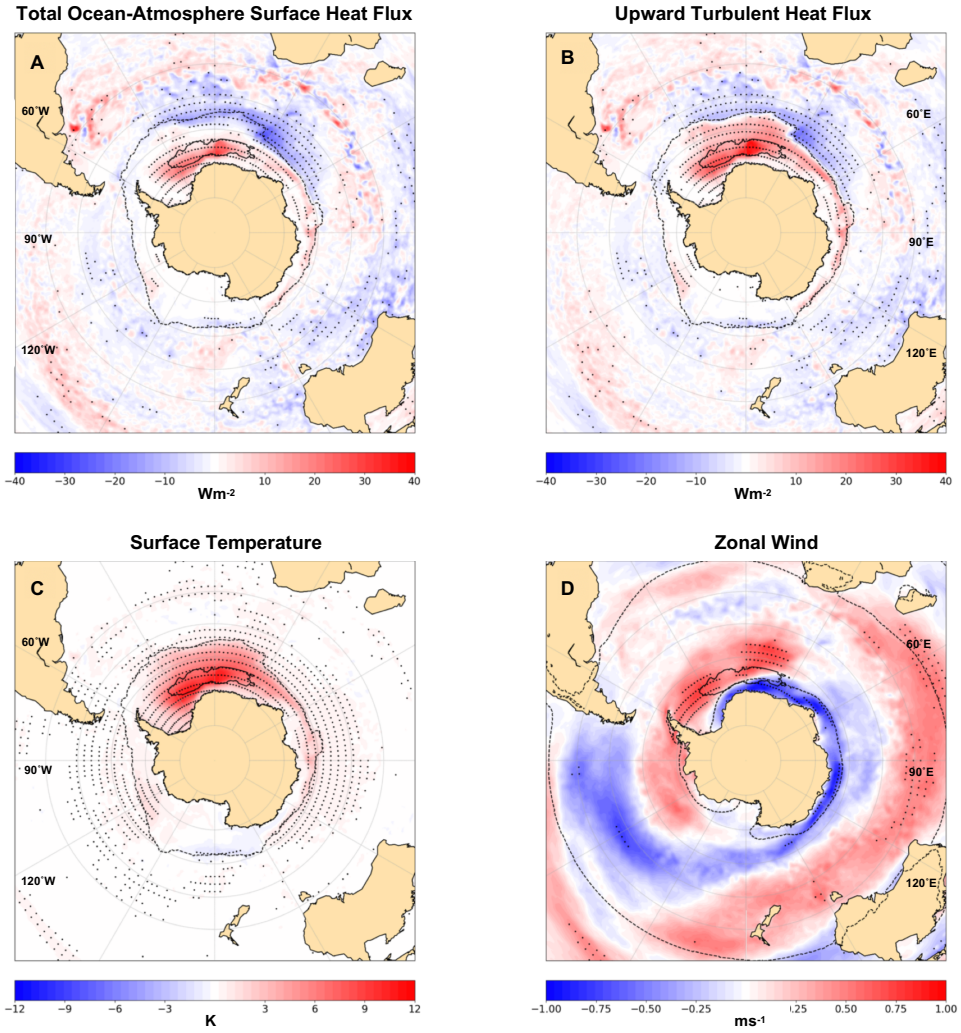

Figure 2.1: The August, September, and October (ASO) seasonal average composite difference between polynya years and non-polynya years for a) total ocean-atmosphere surface heat flux b) upward turbulent heat flux, c) surface temperature, and d) near-surface zonal wind (U), where red (positive) colors indicate an eastward wind anomaly, and blue (negative) colors indicate a westward wind anomaly. The solid black contour denotes the polynya mask. In a), b), and c), the dotted black contour represents the 15% ASO-average sea-ice fraction contour. In d), the dotted black contours represents the borders where ASO-average, climatological zonal wind shifts from positive (westerly) to negative (easterly). Stippling indicates the 95% statistical significance level for a Student's t-test that the mean of polynya and non-polynya years are different.

is conducted in both directions for each model and each grid cell, providing a spatial perspective on the coupling between the two quantities.

To aid our evaluation of the Granger-VAR analysis, we first examine the

temporal relationship between the polynya heat loss and surface temperature time series (Fig. 2.2a). Along with polynya heat loss, we define an accompanying time series of high-latitude surface temperature ($T_{s,hl}$) as the spatial average of all grid cells poleward of 55°S, including Antarctica. Since most of the temperature differences between polynya years and non-polynya years occur poleward of 55°S (Fig. 2.1c), it is a useful boundary for assessing changes in the Southern Hemisphere equator-to-pole temperature gradient. $T_{s,hl}$ and F_p are correlated throughout the entirety of the simulation ($r = 0.6$), and positive anomalies in both time series peak during polynya years. During the longest consecutive appearances of open-ocean polynyas, $T_{s,hl}$ and F_p will increase for several years at a time, with the temperature time series sustaining a positive anomaly until the polynyas cease appearing. When these positive anomalies are sustained, peaks in $T_{s,hl}$ typically lag peaks in F_p by 2-3 years.

The Granger causality tests in each grid cell are largely consistent with this initial examination: increases in F_p predict a positive anomaly in surface temperature ($[F_p \rightarrow T_s]$, Fig. 2.2b). For each grid cell where Granger causality exists, the AIC selects maximum lag orders ranging from 12-24 months, with a mean of 19 months. The lags explaining the most variance are at 1-3 months and 12-14 months. These peaks reflect the immediate response to polynya heat loss, as well as the tendency for open-ocean convection to occur for multiple consecutive winters. In other words, if polynya heat loss causes positive surface temperature anomalies in one year, it is more likely to do so again the next year. The lagged regressions between the response term (T_s) and predictor term (F_p) are relatively constant across the 12-24 month maximum lag order. By contrast, the autoregressions of surface temperature against itself are large in the first 1-2 months, and then decay to zero. Therefore, the

effect of polynya heat loss on surface temperature has a longer timescale than the memory of surface temperature. The total predicted anomalies in surface temperature are highest over the western Weddell Sea and uniformly positive throughout the rest of the Weddell Sea sector. Most of the changes are confined poleward of the ASO sea-ice edge. The magnitude of the predicted anomalies is consistent with the annual mean composite difference between polynya years and non-polynya years, but smaller than the ASO-composite difference (Fig. 2.1c). The smaller predicted anomalies reflect that the Granger-VAR analysis utilizes all months in the year, not just the season of maximum polynyna heat loss. Fig. 2.2c shows the results of the Granger Causality test in the other direction: $[T_s \rightarrow F_p]$. Temperature has less power in predicting polynya heat loss than vice-versa, with the exception of the polynya mask region itself. This difference confirms that the anomalous open water during polynya years is heating the atmosphere through a deep ocean heat source.

Next, coupling between polynyas and near-surface zonal wind (U) is quantified by constructing additional bi-variate VAR models in each grid cell: ($[F_p$, $U]$,Fig. 2.3a, 2.3b). As with $[F_p, T_s]$, these models also use monthly time stepping intervals, with a similar 12-24 month maximum lag order selected by the AIC. The spatial pattern of Granger causality in the Weddell Sea shows that polynya heat loss and Weddell Sea zonal wind are coupled over this approximate 2-year window of predictability. In this bivariate VAR model, enhanced subpolar westerly winds are a response, rather than a driver, of polynya heat loss (Fig. 2.3a). The $[F_p \rightarrow U]$ causality test predicts enhanced subpolar westerlies from 60°S to 50°S, with similar meridional boundaries as the polynya mask region. This regionally confined intensification of the westerly wind is accompanied by an intensification of the easterlies

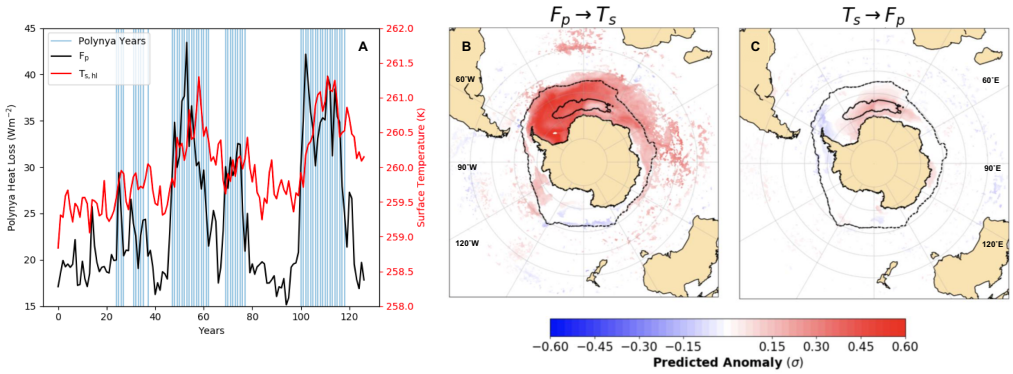

Figure 2.2: a) August, September, and October (ASO) average times series of polynya heat loss (F_p, black line) and annual average surface temperature poleward of 55°S ($T_{s,hl}$, red line) for each year in the 127-year simulation. Vertical blue lines denote polynya years. b) and c) Granger causality between heat loss in the polynya mask region (F_p) and surface temperature (T_s). The causality test in each panel is designated by the predictor variable (left of arrow) and response variable (right of arrow). Shaded values are only shown where Granger causality is found. Predicted anomalies represent the change in the response variable that is predicted by a 1 standard deviation anomaly in the predictor variable, calculated as in Equation 2.7. Solid black and dotted black contours are shown as in Figure 2.1a, 2.1b, and 2.1c.

directly south of the polynya mask. Taken together, this meridionally confined region of predictability is consistent with the zonally asymmetric wind anomaly shown in Fig. 2.1d: an enhanced cyclonic wind circulation in the Weddell Sea and a locally enhanced temperature gradient between the polynya mask and the surrounding seasonal sea-ice region. The westerly wind anomaly is also spatially correlated with the region of enhanced ocean heat uptake in Fig. 2.1a. We consider the possibility that westerly wind anomalies promote northward Ekman advection and anomalous cooling of the surface ocean north of the polynya on yearly timescales. However, this mechanism should be accompanied by negative subpolar surface temperature anomalies and northward sea-ice expansion, which is not seen in the E3SMv0-HR simulation. Instead, we hypothesize that the anomalous ocean heat gain north of the ice edge is promoted by advection of anomalously warm and moist air that

has passed over a polynya, and by enhanced heat transfer rates due to larger wind speeds.

Granger causality in the $[U \rightarrow F_p]$ direction is found through a large extent of the Southern Ocean. Polynya heat loss is predicted by circumpolar easterly wind anomalies near the Antarctic continent, while also being predicted by westerly wind anomalies occurring in more northern latitudes of the Southern Ocean's Atlantic/Indian sectors (Fig. 2.3b). Though the westerly wind anomalies are not circumpolar in nature, the spatial pattern of Granger causality is nonetheless suggestive of the SAM's negative phase: a northward shift in the westerly wind belt. The average VAR model lag order for this test is 18 months, leading us to hypothesize that the equatorward shifted westerlies (prolonged negative SAM, Fig. 2.3b) precondition the Weddell Sea for open-ocean convection during non-polynya years. We seek to identify the long-term preconditioning mechanism by calculating the contemporaneous relationship between Southern Hemisphere surface conditions and monthly Weddell Sea wind stress curl anomalies, but during non-polynya years only (Fig. 2.4). The mean Weddell Sea wind stress curl is negative, so a positive anomaly indicates a weaker, less cyclonic wind stress curl, and vice versa. Our use of this metric is motivated by a prior examination of E3SMv0-HR; Kurtakoti et al. (2018) found that non-polynya years generally feature positive wind stress curl anomalies in the Weddell Sea, which then become negative immediately prior to open-ocean convection. We find that these positive wind stress curl anomalies are associated with increased westerlies equatorward of 60°S, consistent with a negative phase of the SAM (Fig. 2.4a). Therefore, we verify that the simulated Weddell Sea wind stress curl anomalies are negatively correlated with the SAM index, as has been

shown in observations (Campbell et al. 2019). During the months of maximum sea-ice extent (August, September, and October), the wind stress curl anomalies are positively correlated with sea-ice fraction in the Weddell Sea, while being negatively correlated with upward surface heat flux (F) over the seasonal sea-ice region (Fig. 2.4b, 2.4c). For a 1 σ positive wind stress curl anomaly, upward surface heat flux reductions in the Weddell Sea are on the order of 10 W m^{-2}, while, in the same areas, sea-ice fraction increases in the range of 5 to 10 percent per grid cell. The prolonged negative SAM identified in Fig. 2.3b is therefore associated with reduced surface heat loss in non-polynya years. As will be shown in section 2.3.3, this reduced surface heat loss leads to a buildup of high-latitude ocean heat content that Granger causes polynya heat loss on interannual timescales.

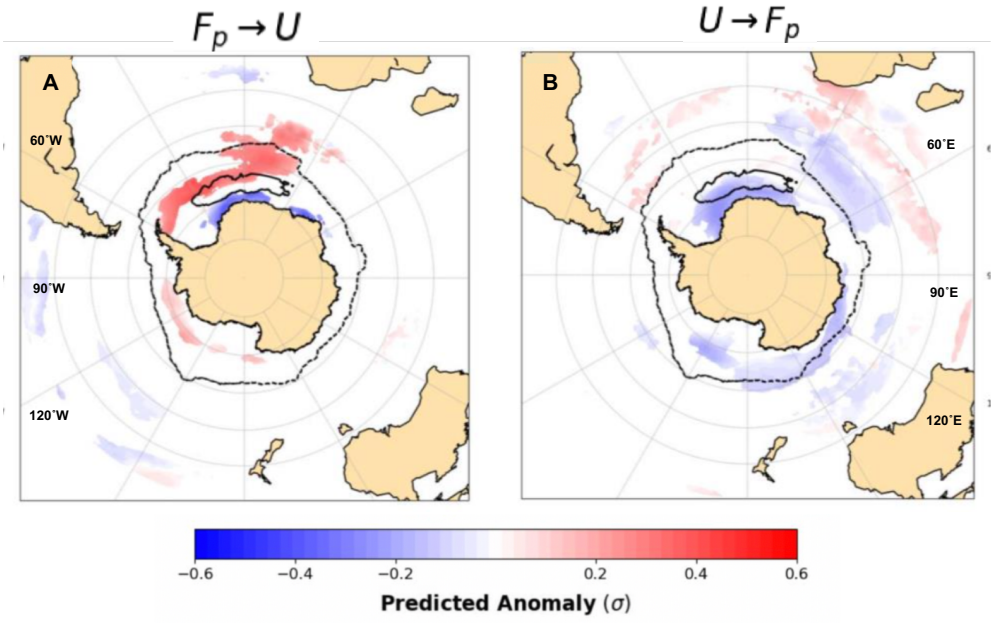

Figure 2.3: a) and b): Granger causality between heat loss in the polynya mask region (F_p) and zonal wind (U), shown as in Figure 2.2. Red (positive) colors indicate an eastward wind anomaly, and blue (negative) colors indicate a westward wind anomaly.

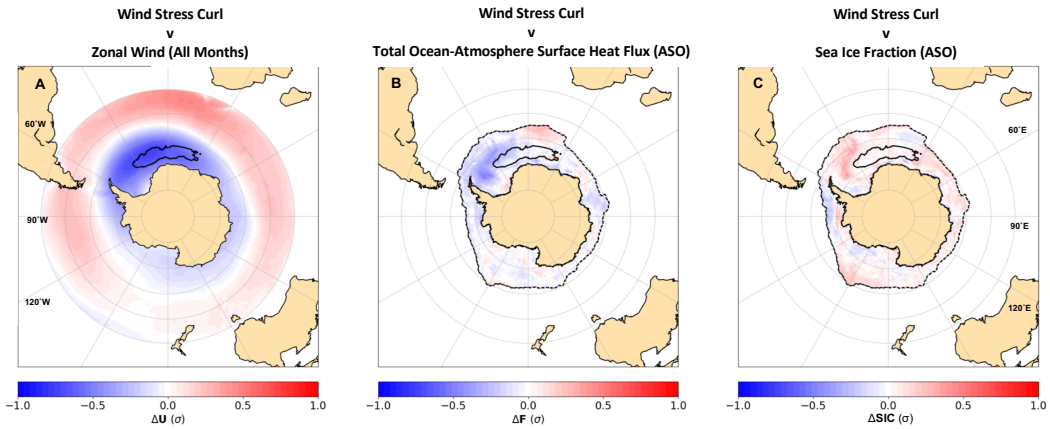

Figure 2.4: Lag-0 regression of monthly wind stress curl anomalies, averaged over the Weddell Sea (55°W-40°E, 55°S-73°S), on a) zonal wind (U, all months), b) total ocean-atmosphere surface heat flux (F, August, September, October (ASO)), and c) sea-ice concentration (SIC, ASO) for non-polynya years only. Shaded values indicate the change in each metric associated with a 1 σ positive wind stress curl anomaly, where positive values indicate less cyclonic (weaker) wind stress curl. Solid black and dotted black contours are shown as in Figure 2.1a, 2.1b, and 2.1c.

We further explore the role of large-scale zonal wind variability by examining its relationship with approximated high-latitude mixed-layer salinity ($SALT$) anomalies, averaged over the top 100 m of the water column. Our interest in the role of salinity is motivated by observations (Campbell et al. 2019) and model simulations (Cheon et al. 2014) that demonstrate the triggering of deep convection by high $SALT$ anomalies concurrent with the opposite, positive phase of the SAM (poleward shifted westerlies). First, we find that positive SALT anomalies both within and upstream of the polynya mask region predict polynya heat loss on lag-order time scales of 18-24 months ([$SALT$, F_p], Fig. 2.5a). The lag-order timescale and upstream predictive region are suggestive of westward-propagating, high-salinity anomalies that often precede polynya episodes in E3SMv0-HR, initially identified in Kurtakoti et al. (2018). Given this resemblance, we proceed to represent these upstream anomalies with a single time series of SALT, horizontally averaged over the Eastern Weddell

Sea ($SALT_{EWS}$), in particular over the region 62°S - 68°S, 15°E - 60°E (denoted by the dashed box in Fig. 2.5). Then, as with [F_p, U], we relate this single time series of mixed-layer salinity anomalies to the time series of zonal wind anomalies in each grid cell. [$SALT_{EWS} \rightarrow U$] (Fig. 2.5b) displays a similar pattern of Granger causality to [$F_p \rightarrow U$] (Fig. 2.3a), though the regression coefficients are smaller. This similar wind pattern further supports the role of mixed layer salinity east of the polynya region in predicting polynya formation. By contrast, [$U \rightarrow SALT_{EWS}$] (Fig. 2.5c) displays a different pattern of Granger causality from [$U \rightarrow F_p$] (Fig. 2.3b): positive salinity anomalies are predicted by an *intensification* of the circumpolar westerly winds between 70°S and 50°S. As suggested by past observations and model experiments, the zonal wind pattern in Figure 2.5c, which is representative of the SAM's positive phase, imposes a negative wind stress curl over the Weddell Sea basin (Cheon et al. 2014; Cheon et al. 2018; Campbell et al. 2019). It is also worth noting that this zonal wind pattern only Granger causes salinity anomalies in the upstream region ($SALT_{EWS}$); U does not predict salinity anomalies when they are averaged over the polynya mask region (not shown). Again, this distinction implies that salinity anomalies are first introduced upstream of the polynya mask before being advected westward.

Several mechanisms could explain the generation of positive salinity anomalies in the Eastern Weddell Sea. First, the negative wind stress curl spins up the Weddell Gyre circulation; and indeed, polynya heat loss is predicted by a stronger barotropic streamfunction in the Weddell Sea (not shown). This strengthening pulls in more salty water from the Antarctic Circumpolar Current in the southern branch of the Weddell Gyre. However, this causal pathway is somewhat complicated by

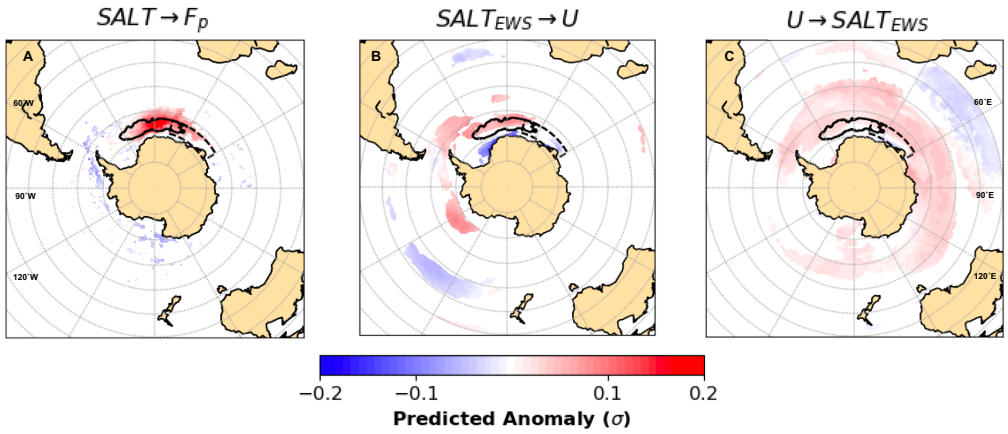

Figure 2.5: a) Granger causality between approximate mixed-layer salinity ($SALT$) in each model grid cell and polynya heat loss. b) and c): Granger causality between approximate mixed-layer salinity in the Eastern Weddell Sea ($SALT_{EWS}$), and zonal wind (U) in each model grid cell. The dotted black box denotes the averaging region for $SALT_{EWS}$.

the fact that the optimal lag order of the predicted anomalies in Figure 2.5c is only about 2 months, hence much shorter than the 18-24 months in Figure 2.5a. This lag order seems too short to be consistent with this advective mechanism. Alternatively, it is conceivable that the upstream salinity anomalies are caused by wind-driven upwelling. To investigate this possibility, we estimate Ekman suction velocities from wind stress curl. Excepting the coastal region, Eastern Weddell Sea Ekman vertical velocities are approximately 0.5 m day^{-1} in the annual mean and exhibit small positive anomalies prior to polynya years (not shown). However, these small anomalies (.05 m day^{-1}), if sustained over several months, would only produce approximately 5 m of additional vertical displacement, which seems to be insufficient to elevate the core of the Weddell Deep Water to the surface. We conclude that other wind-driven processes may play an additional role in introducing the upstream salinity anomalies, such as anomalous brine rejection and ice production along the coast.

In summary, we show that large-scale zonal wind variability Granger causes

both polynya heat loss and positive upper-ocean salinity anomalies in the Weddell Sea. The distinct timescales and spatial patterns that we isolate suggest a complex relationship between SAM variability and open-ocean convection. First, a prolonged negative phase of the SAM (Fig. 2.3b) preconditions the polynya mask region for open-ocean convection by inhibiting upward surface heat flux during non-polynya years (Fig. 2.4). Then, a poleward intensification of the westerlies (Fig. 2.5c) acts as a short-term trigger for deep convection by spinning up the Weddell Gyre circulation and introducing positive salinity anomalies that destratify the water column (Fig. 2.5a). This relationship between open-ocean convection and large-scale zonal wind patterns was not initially evident in the composite difference between polynya years and non-polynya years (Fig. 2.1d), likely because a composite difference does not distinguish between the zonal wind variability that predicts polynya heat loss (Fig. 2.3b) and the more localized zonal winds that respond to polynya heat loss (Fig. 2.3a).

2.3.3 Changes in Poleward Heat Transport and Ocean Heat Content

Lastly, we move outside the Weddell Sea to analyze larger-scale changes in meridional heat transport and ocean heat content during polynya years, as well as the relative partitioning of transport between the atmosphere and the ocean. In our initial analysis, we find that atmosphere (AHT) and ocean (OHT) heat transport are negatively correlated poleward of 60°S and positively correlated equatorward of 60°S (Fig. 2.6). The correlation values increase when we use decadal, rather than annual averages, reflecting the decreasing importance of oceanic heat storage on

longer timescales. Short-term variability in OHT is thus likely buffered by heat storage, while long-term variability is compensated by surface fluxes. This distinction motivates a switch from monthly time series resolution to annual resolution in the Granger causality analysis for heat transport; a VAR model with monthly time steps would require an excessive lag order to capture multidecadal variability in the ocean. We accordingly conduct Granger-VAR analysis for AHT, OHT, and F_p using yearly time step intervals, with separate VAR models being constructed at each latitude. The composite difference in heat transport anomalies between polynya and non-polynya years is shown in Fig. 2.7, along with the significant Granger causality results and VAR model lag orders.

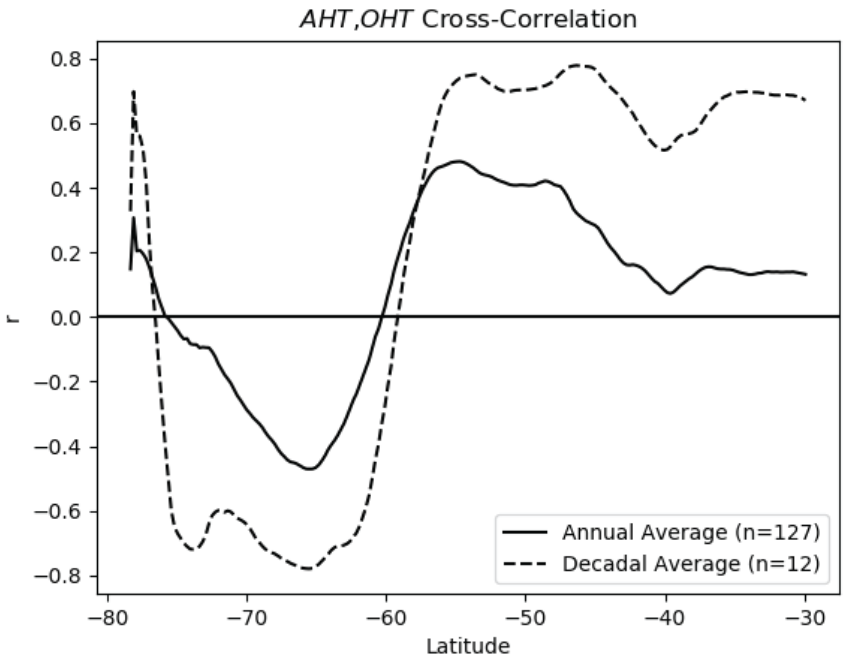

Figure 2.6: Instantaneous cross-correlation (r) between atmospheric heat transport (AHT) and ocean heat transport (OHT), calculated at each latitude between 30°S and the Antarctic continent for both annually averaged (solid line) and decadally averaged (dashed line) time series.

First, no significant Granger causality is found in the $[AHT \rightarrow F_p]$ direction or the $[OHT \rightarrow F_p]$ direction (not shown). In other words, polynya heat loss is not predicted by changes in meridional heat transport in the atmosphere or ocean. Second, we find a decrease in poleward atmospheric heat transport predicted by polynya heat loss, shown with the $[F_p \rightarrow AHT]$ causality test (Fig. 2.7a). Polynya heat loss predicts a positive anomaly in AHT (poleward weakening) between 70°S and 40°S, on a timescale of 1 year. The sign of the predicted atmospheric response, as well as the maximum composite difference around 60°S, suggests that the changes in atmospheric heat transport are connected to the reduced meridional temperature gradient described in section 2.3.2, and an associated reduction in dry static energy transport. Reduced atmospheric heat transport in response to polar-amplified warming has also been seen in the Arctic (Hwang et al. 2011). A small subset of VAR models for $[F_p \rightarrow AHT]$ have a larger lag-order between 50°S and 40°S, a notable visual irregularity. Given that a relatively fast response time is expected in the atmosphere, we interpret this different lag-order as a statistical outlier associated with the AIC selection algorithm, rather than a distinct geophysical process.

Finally, we find that significant Granger causality is also found with the $[F_p \rightarrow OHT]$ test, which predicts a negative anomaly (poleward strengthening) of ocean heat transport south of 60°S, and a weakening of ocean heat transport north of 60°S (Fig. 2.7b). The changing sign of the predicted response with latitude is consistent with a poleward shift in the ocean heat flux convergence. The predicted behavior of ocean heat transport also resembles the zonal mean turbulent heat flux anomalies (Fig. 2.1a), which display a similar poleward shift. The lag-order of the OHT VAR models is spatially distinct: the window of predictability is 5-6 years

in the high latitudes, and 1 year in the midlatitudes. This maximum lag order difference may reflect separate mechanisms for the predicted ocean heat transport change in each region. In the high latitudes, it likely takes several years for polynyas to deplete the deep ocean heat reservoir associated with open-ocean convection in the Weddell Sea, and for the ocean to replenish the reservoir. Accordingly, there would be a relatively long response time for ocean heat transport to compensate polynya heat loss in the high latitudes. By contrast, the faster midlatitude OHT changes predicted by polynya heat loss are likely mediated by the atmosphere. As seen in our analysis of Fig. 2.3a, the localized zonal wind response to polynya heat loss can promote anomalous ocean heat gain north of the climatological sea-ice edge, despite the concurrent reduction in poleward atmospheric heat transport (Fig. 2.7a). This atmospherically-driven heat gain is consistent with the midlatitude OHT response. In summary, poleward ocean heat transport reduction in the midlatitudes represents the fast response to polynya heat loss, whereas ocean heat transport enhancement in the high latitudes represents the slow response to polynya heat loss.

Our finding that meridional heat transport anomalies do not drive polynya heat loss, but are rather a response to it, is counterintuitive; prior modelling studies of Weddell Sea deep convection suggest that a buildup of the high-latitude ocean heat reservoir is an important precondition for the occurrence of a polynya (Latif et al. 2013; Cabré et al. 2017). Therefore, to clarify our understanding, we conduct a similar Granger causality test for the ocean heat content south of 65°S ($[F_p, OHC]$), where OHC is calculated as the cumulative temporal integral of advective and surface heat fluxes according to Eq. 2.4. The results for these causality tests are shown in Figure 2.8. As expected, ocean heat content features a negative anomaly

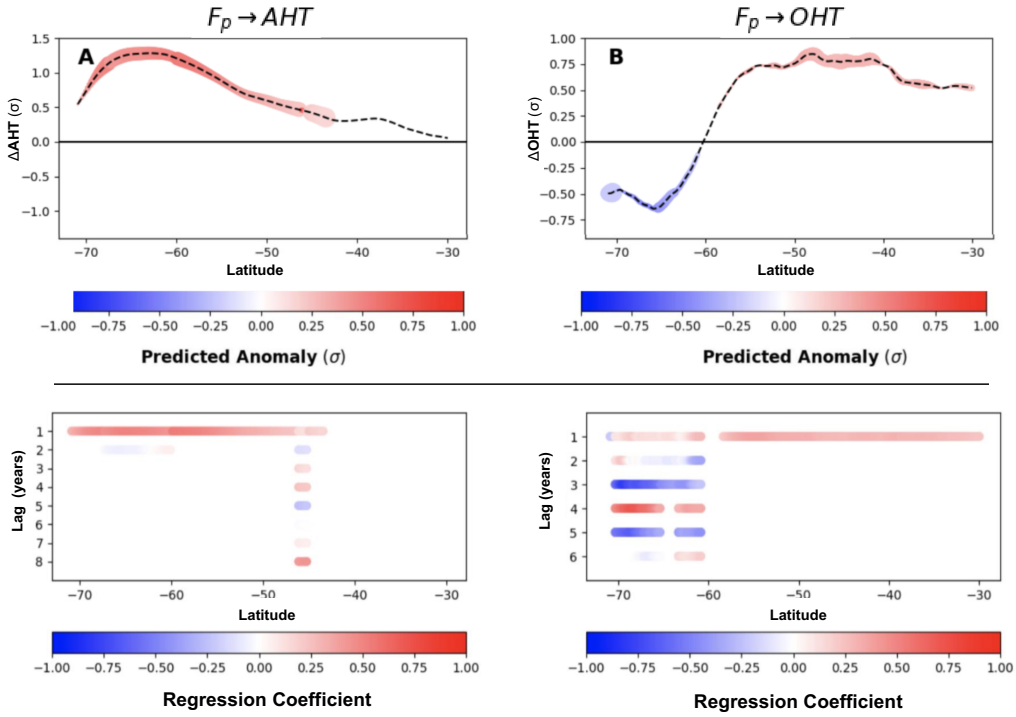

Figure 2.7: Composite difference in a) atmospheric heat transport (AHT) and b) ocean heat transport (OHT) between polynya years and non-polynya years (dashed lines). Since the magnitude of heat transport varies significantly with latitude, differences are normalized by subtracting the original time series mean and dividing by the standard deviation at each latitude. If Granger causality is found at a latitude band, lagged regression coefficients from the associated VAR model are shown for individual lags (bottom panel) and as a sum (top panel) with colors. Positive (red) values indicate a northward transport anomaly. For each latitude, the color points in the top panel (predicted anomalies) are larger when the autocorrelation of the response variable is larger.

in the high latitudes during polynya years, which is driven by polynya heat loss ($[F_p \rightarrow OHC]$; Fig. 2.8a). Most importantly, however, ocean heat content is also a predictor of polynya heat loss in the high-latitudes ($[OHC \rightarrow F_p]$; Fig. 2.8b), with a decadal buildup of heat predicting stronger polynya heat loss. Since OHC is inferred here from the difference between OHT and the meridional integral of F, we can assess the relative contribution of these two terms to the total OHC. Fig. 2.8c shows that the buildup of the heat reservoir south of 65°S is driven by a persistent

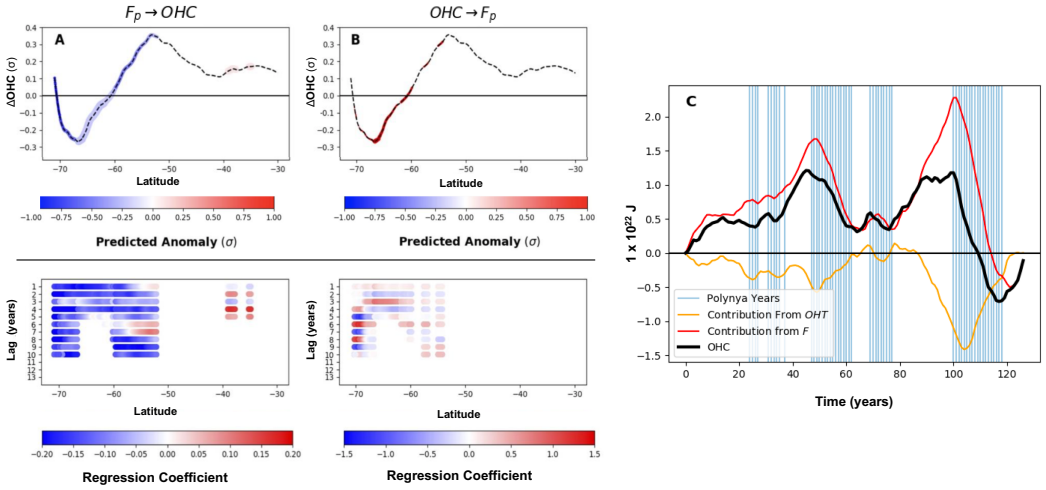

Figure 2.8: a) and b) Granger causality between F_p and ocean heat content (OHC), shown as in Figure 2.7, where OHC is reconstructed from the cumulative time integral of advective and surface heat fluxes (Equation 2.4). c) Time series of the transport and surface flux contributions to ocean heat content south of 65°S. The red, orange, and black lines represent the three terms in Equation 2.4. Blue lines denote polynya years, as in Figure 2.2a. The OHC time series are detrended for the Granger causality tests in a) and b), but not for the lines displayed in c).

reduction in ocean heat loss (positive OHC anomalies) before polynya years, when more sea ice can insulate the ocean and prevent heat escape. This heat buildup is counteracted by a reduction in poleward ocean heat transport (negative OHC anomalies). Hence, surface heat flux changes dominate the total trend in ocean heat content.

2.4 Summary and Discussion

We apply statistical causal inference techniques to a high-resolution, fully coupled climate model, drawing robust connections between polynya heat loss and several metrics of atmosphere-ocean variability in the high-latitude climate system. Under pre-industrial conditions, we find that upward turbulent heat fluxes shift poleward during polynya years, promoting enhanced ocean heat loss from the Wed-

dell Sea, a reduction in the meridional temperature gradient, and an intensification of the Weddell Sea cyclonic wind circulation. Polynya heat loss also has remote impacts on meridional energy transport: poleward heat transport decreases in the atmosphere, while ocean heat flux convergence anomalies closely track the upward turbulent heat flux anomalies. Finally, our statistical analyses disentangle the local wind response to polynya heat loss from the larger-scale atmospheric variability that controls open-ocean convection. In agreement with prior model simulations as well as observations, our predictive causality models show that polynya formation is influenced by zonal wind variability representative of the SAM (Campbell et al. 2019; Cheon et al. 2014; Cheon et al. 2018). Open-ocean polynyas in E3SMv0-HR show the capability to both drive and respond to atmospheric variability in the Weddell Sea.

As with the 1974-1976 Weddell polynyas, the Maud Rise seamount appears to be a critical bathymetric feature for triggering open-ocean polynyas and setting the site of deep convection in our simulation (Holland 2001). In E3SMv0-HR, the dynamical impact of Maud Rise is a direct consequence of its accurate representation by the fine model resolution (Kurtakoti et al. 2018). The resulting spatial structure of sea-ice reduction and increased surface temperature sets a zonally asymmetric pattern of the atmospheric response, i.e., strengthened zonal winds over the Weddell Sea during polynya years (Fig. 2.3a).

We find bi-directional Granger causality between polynya heat loss and zonal wind, showing that changes in Southern Hemisphere atmospheric circulation both drive and respond to open-ocean convection, with the coupled relationship being mediated by upper-ocean salinity and sea ice. This result suggests that future

investigations of atmosphere-ocean-ice variability in the Southern Ocean, whether through targeted modeling experiments or observational analysis, should acknowledge the potential bi-directional causality between these climate processes. For instance, idealized experiments perturbing the westerly wind field over the Southern Ocean have produced polynyas through a wind-driven spin-up of the Weddell Gyre, promoting Ekman divergence of the surface waters in the Weddell Sea (Cheon et al. 2014; Cheon et al. 2018). While our analysis is consistent with the results of these experiments, we also find that the Weddell Sea subpolar westerlies are enhanced in response to polynya heat loss. In our study, detailed statistical analysis allows us to reveal this coupled relationship.

The meridional heat transport response to polynya heat loss (Fig. 2.7) can offer insight into the interannual, episodic nature of open-ocean convection in E3SMv0-HR. We see that, north of 60°S, the ocean does not compensate the decrease in poleward atmospheric heat transport, a behavior one might have expected from the compensation theory of Bjerknes (1964). In the high-latitudes, our analysis of ocean heat content illustrates that each episode of polynya heat loss is preceded by periods of reduced surface heat flux, larger sea-ice coverage in the Weddell Sea, and a buildup of the deep ocean heat reservoir. In this model, it thus appears that sea-ice cover alone can lead to heat buildup and a periodic occurrence of polynyas, despite counteracting anomalies in ocean heat transport. Future examinations of this process will be key for constraining the intervals between deep convection events, which vary by two orders of magnitude (1 year to 100 years) among the 25 convecting CMIP5 models (De Lavergne et al. 2014).

While it is unknown what hydrographic changes preceded the 1974-1976

Weddell polynyas, Campbell et al. (2019) argue that the warming trend of Weddell Deep Water in recent decades is insufficient to trigger the small open-ocean polynyas observed in 2016 and 2017. They diagnose a 0.03 K/decade warming trend of Weddell Deep Water (WDW) from 2002 through 2016, consistent with the 0.032 K/decade mean trend observed between 1977-2001 by (Smedsrud 2005). In E3SMv0-HR, this rate is on the order of 0.1 K/decade for non-polynya years. It is certainly possible that our model unrealistically limits surface heat loss, either due to biases in freshwater forcing (Stössel et al. 2015), or unrealistically weak mixing of the Southern Ocean under sea ice (Heuzé et al. 2013). Even so, any warming trend must reflect an imbalance between surface heat loss and lateral heat supply; and any process that further limits surface heat loss, like anthropogenic freshwater forcing (De Lavergne et al. 2014), would tend to increase this imbalance. Therefore, unless the ocean advective heat supply will adjust and neutralize the heat content buildup, an episodic release of the stored heat will happen eventually. Future simulations of open-ocean polynyas will need to include both anthropogenic forcing and a longer simulation time to fully resolve these ambiguities.

Fortunately, the improved representation of open-ocean polynyas in E3SMv0-HR appears to be clearly tied to the resolution of the model components (Kurtakoti et al. 2018). As resolution continues to improve among other fully coupled models, so too should the representation of deep convection in the Weddell Sea. New opportunities will become available to study how polynya heat loss influences high-latitude climate variability, as well as how this variability imprints onto the regionally distinct responses to anthropogenic climate change. Our statistical analysis of a preindustrial-control simulation can be used to motivate and inform future model

experiments studying this important aspect of the climate system.

Chapter 3

Causes of the Arctic's Lower-Tropospheric Warming Structure

This chapter is a slightly modified reprint of work previously published as Kaufman, Zachary S., and Nicole Feldl."Causes of the Arctic's Lower-Tropospheric Warming Structure." Journal of Climate 35.6 (2022): 1983-2002.

Abstract

Arctic amplification has been attributed predominantly to a positive lapse rate feedback in winter, when boundary-layer temperature inversions focus warming near the surface. Predicting high-latitude climate change effectively thus requires identifying the local and remote physical processes that set the Arctic's vertical warming structure. In this study, we analyze output from the CESM Large Ensem-

ble's 21st century climate change projection to diagnose the relative influence of two Arctic heating sources, local sea-ice loss and remote changes in atmospheric heat transport. Causal effects are quantified with a statistical inference method, allowing us to assess the energetic pathways mediating the Arctic temperature response and the role of internal variability across the ensemble. We find that a step-increase in latent heat flux convergence causes Arctic lower-tropospheric warming in all seasons, while additionally reducing net longwave cooling at the surface. However, these effects only lead to small and short-lived changes in boundary layer inversion strength. By contrast, a step-decrease in sea-ice extent in the melt season causes, in fall and winter, surface-amplified warming and weakened boundary-layer temperature inversions. Sea-ice loss also enhances surface turbulent heat fluxes and cloud-driven condensational heating, which mediate the atmospheric temperature response. While the aggregate effect of many moist transport events and seasons of sea-ice loss will be different than the response to hypothetical perturbations, our results nonetheless highlight the mechanisms that alter the Arctic temperature inversion in response to CO_2 forcing. As sea ice declines, the atmosphere's boundary-layer temperature structure is weakened, static stability decreases, and a thermodynamic coupling emerges between the Arctic surface and the overlying troposphere.

3.1 Introduction

Global climate change is characterized by an Arctic-amplified pattern of surface warming. This warming pattern is a robust feature of climate models sub-

jected to increases in CO_2 (Manabe and Stouffer 1980; Holland and Bitz 2003), and observed Arctic temperatures have warmed at twice the global average in recent decades (Serreze et al. 2009; England et al. 2021). However, considerable uncertainty remains regarding the underlying mechanisms of the Arctic Amplification phenomenon (Smith et al. 2019). Accurate predictions of future warming trends require understanding of the various feedback mechanisms acting at high latitudes. The surface albedo feedback associated with sea-ice loss has long been understood to shape polar climate sensitivity: melting snow and sea ice increases the surface absorption of solar radiation, leading to additional warming (Manabe and Wetherald 1975). However, the changes in sea ice are largest in summer, while Arctic near-surface warming trends are largest in winter (Lu and Cai 2009), when shortwave radiative fluxes are small. This discrepancy highlights an additional positive feedback, the high-latitude lapse rate feedback, which is associated with the Arctic's surface-amplified warming in the cold season (Winton 2006). More generally, the lapse rate feedback describes the effect of vertically nonuniform tropospheric warming on the efficiency of radiative cooling to space.

The surface-amplified warming characteristic of a positive lapse rate feedback arises in the Arctic due to stable stratification of the wintertime boundary layer, which inhibits upward mixing of thermal anomalies away from the surface (Bintanja et al. 2011). Compared to vertically uniform warming, this bottom-heavy structure necessitates larger surface temperature increases to drive the change in outgoing longwave radiation that balances anthropogenic CO_2 forcing (i.e., a positive lapse rate feedback). This situation can be contrasted with the tropics, where deep convection leads CO_2-forced warming to maximize in the upper troposphere, producing

more efficient radiative cooling and a negative lapse rate feedback. Therefore, the spatial pattern of lapse rate changes drives Arctic amplification in fully coupled climate models (Pithan and Mauritsen 2014; Stuecker et al. 2018), as well as hemispheric asymmetries in projected polar warming, where the Arctic exhibits greater warming than the Antarctic (Hahn et al. 2020).

Though the physical basis for the positive high-latitude lapse rate feedback is well established, its coupled interactions with other aspects of the climate system remain unclear. From a local perspective, quantifying the warming contribution of the Arctic lapse rate feedback is challenging because of its interdependent relationship with sea ice. Reductions in ice cover during the warm season can lead to a buildup of heat in the newly exposed ocean, delaying freeze-up in fall and winter (Serreze et al. 2007b; Serreze et al. 2009; Boeke and Taylor 2018). This stored heat can then be released to the overlying near-surface atmosphere via enhanced upward turbulent heat fluxes (Manabe and Stouffer 1980; Bintanja and Linden 2013; Dai et al. 2019; Feldl et al. 2020). Supporting this coupled mechanism, modeling experiments that disable or suppress the ice-albedo feedback have shown a corresponding reduction in the polar lapse rate feedback (Graversen et al. 2014a; Feldl et al. 2017a).

In addition to local feedbacks, remote processes may also influence Arctic warming through the poleward transport of heat and moisture. Though 21st century climate change simulations project only small increases in net atmospheric heat transport into the Arctic, compensating decreases in dry static energy transport (Hwang et al. 2011) and increases in latent heat transport (Held and Soden 2006) can be much larger. Beyond the effect of latent heating upon condensation, remotely sourced moisture can contribute to Arctic warming through the water vapor and

cloud feedbacks, which increase the infrared opacity of the atmosphere and tend to strengthen downward longwave radiative fluxes (Lee et al. 2017; Yoshimori et al. 2017; Graversen and Langen 2019). These impacts of latent heat transport on the surface radiation budget have been implicated in Arctic warming and sea ice trends (Park et al. 2015a; Park et al. 2015b; Gong et al. 2017). Further, a tropical mechanism causing Arctic warming has been identified in models forced by prescribed tropical sea surface temperatures (SSTs, Ding et al. 2014; Dong et al. 2019). The tropically excited Arctic warming mechanism has been used to explain observed wintertime near-surface Arctic warming, where anomalous deep convection over the West Pacific promotes Rossby wave propagation towards higher latitudes during the La Niña phase of the El Niño Southern Oscillation (Lee 2012; Liu and Barnes 2015; Baggett and Lee 2017). Finally, remotely sourced Arctic warming can be accomplished by anomalous ocean heat transport, which has been shown to drive multi-year sea-ice declines in many climate models, particularly along continental shelves (Auclair and Tremblay 2018). However, meridional energy flux convergence into the Arctic is dominated by the atmospheric component (Serreze et al. 2007a), which is the primary focus of our study.

The complex interplay between local feedbacks and remote heat transport hampers efforts to isolate an individual process' contribution to Arctic warming. Overcoming this difficulty requires identifying the changes in the Arctic troposphere that are ultimately local or remote in origin. As demonstrated by Feldl et al. (2020), a partitioning of the lapse rate feedback into upper and lower contributions reveals that lower-tropospheric warming is strongly tied to climatological sea-ice extent and sea-ice loss, enhancing the positive lapse rate feedback, while remotely driven

increases in heat transport warm the mid-troposphere, weakening the lapse rate feedback in subpolar latitudes. Similar interactions between the lapse rate feedback and atmospheric heat transport have been previously noted by Feldl et al. (2017b) and Stuecker et al. (2018). Crucially, this remote influence on the high-latitude lapse rate feedback does not preclude a warming influence on the Arctic surface due to the aforementioned moist transport effects. Direct attributions of polar atmospheric temperature change in a single-column model emphasize the role of CO_2 and water vapor in warming the surface and atmospheric heat transport in warming the mid- and upper troposphere, with compensating behavior by the dry heat transport in the presence of a surface heat source (Henry et al. 2021). Lastly, it is well established that enhanced atmospheric heat transport is able to produce Arctic amplification in simulations that have meridionally uniform radiative feedbacks (Merlis and Henry 2018; Armour et al. 2019), suppress the ice-albedo feedback (Graversen and Wang 2009), or lack sea ice altogether (Alexeev et al. 2005), though there is some evidence that this response may be due in part to the idealized nature of the simulations (Kim et al. 2018). Attributions of polar amplification are thus represented differently across models of varying complexity and for different attribution methods.

A pressing challenge in climate science is to understand how sea ice and atmospheric circulation interactively set the Arctic's vertical warming structure during the 21st century. Using a statistical causal inference approach, we evaluate coupled relationships and causal pathways between time series of sea-ice concentration, Arctic atmospheric temperatures, surface energy fluxes, and meridional heat flux convergence from output of the Community Earth System Model. Though CO_2 forcing is the ultimate driver of Arctic warming, we seek to identify and quantify

the proximate causes and mediating pathways between sea-ice and heat-transport perturbations and the eventual warming response in a comprehensive model. Such pathways are uncovered using causal network learning algorithms that analyze large numbers of interdependent time series variables at once (Pearl et al. 2000; Spirtes et al. 2000). These novel statistical techniques are just beginning to be applied to the study of Arctic climate (Kretschmer et al. 2016) and their adaptation for geoscience applications is a new and active area of research (Runge et al. 2019). By evaluating the Arctic's temperature inversion in a fully coupled setting, we account for two-way relationships amongst the physical processes of interest. This is a crucial feature of our analysis, as sea ice and atmospheric circulation do not control Arctic climate independently; sea-ice loss, for instance, can itself drive circulation changes in both the atmosphere (Screen et al. 2018; McGraw et al. 2020) and the ocean (Tomas et al. 2016). Our statistical approach therefore disentangles the atmosphere-ocean-ice interactions underlying the high-latitude lapse rate feedback and Arctic amplification.

3.2 Methods

3.2.1 Climate Model Output and Diagnostics

This study is conducted with output from the Community Earth System Model Large Ensemble (CESM-LE, Kay et al. 2015). The CESM-LE climate change simulation is initialized from an equilibrium preindustrial control state, then subjected to historical greenhouse-gas forcing from 1920 to 2005 and projected forcing from 2005-2100 using the RCP8.5 climate forcing scenario. For our analyzed climate

fields, we utilize output spanning 1986-2100. Over this time period, the CESM-LE simulates forty ensemble members with the same underlying physics, but each member's air temperature fields are given slightly differing initial conditions, providing a tool to assess the role of internal variability in climate change projections. By applying our analysis across ensemble members, we can analyze both the forced climate response, represented by the ensemble mean, and internal variability, represented by the ensemble spread.

Our data-driven, causal inference approach applies time series analysis to the CESM-LE model output, where the variables of interest are simultaneously represented in a large, inclusive network for each ensemble member. Causal network input consists of ten spatially averaged time series, which track various aspects of the high-latitude climate system. Each variable and its spatial averaging domain is listed in Table 3.1. Four atmospheric variables are used, two of which represent Arctic temperatures at different altitudes in the troposphere, and two that represent components of meridional energy transport into the high latitudes. Surface energy fluxes and sea-ice extent are represented by the remaining six time series variables. In this section, we provide a physical description of each term within the context of the RCP8.5 scenario.

In all ensemble members, the annual-mean Arctic warming response to RCP8.5 forcing is largest below 850 hPa, dictated primarily by changes in the wintertime vertical temperature structure (Fig. 3.1a). At the end of the 20th century, the Arctic is characterized by stable stratification in the boundary layer; temperature increases with height throughout the lower portion of the atmosphere in all seasons, with strong inversions occurring in winter (DJF) and spring (MAM). By the

Variable	Vertical Domain	Horizontal Domain
Sensible Heat Flux Convergence ($-\nabla_{850} \cdot c_p[\overline{vT}]$)	850 hPa	70°-90°N
Latent Heat Flux Convergence ($-\nabla_{500} \cdot L[\overline{vq}]$)	500 hPa	70°-90°N
Boundary Layer Atmospheric Temperature (T_{850})	850 hPa	1986-1996 annual mean sea-ice edge (15% concentration contour)
Boundary Layer Inversion Strength	T_{850} - T_{2m}	1986-1996 annual mean sea-ice edge (15% concentration contour)
Net All-Sky Longwave Radiative Flux (LW_{net})	Surface	1986-1996 annual mean sea-ice edge (15% concentration contour)
Net All-Sky Shortwave Radiative Flux (SW_{net})	Surface	1986-1996 annual mean sea-ice edge (15% concentration contour)
Shortwave Cloud Radiative Effect (SW_{CRE})	Surface	1986-1996 annual mean sea-ice edge (15% concentration contour)
Longwave Cloud Radiative Effect (LW_{CRE})	Surface	1986-1996 annual mean sea-ice edge (15% concentration contour)
Turbulent Heat Flux	Surface	1986-1996 annual mean sea-ice edge (15% concentration contour)
Sea-Ice Extent	Surface	1986-1996 annual mean sea-ice edge (15% concentration contour)

Table 3.1: List of the causal network input variables described in Section 3.2.1, along with the spatial averaging region used for each time series. Where relevant, parenthesized variable names denote abbreviations used in subsequent figures. Note that turbulent heat flux is defined as the sum of sensible and latent heat flux at the surface.

end of the 21st century, surface-amplified warming fully erodes the boundary-layer temperature inversions in fall (SON) and winter (DJF), with winter experiencing the largest change in inversion strength. Hence, to characterize the vertically non-uniform Arctic temperature changes, our causal networks include 850 hPa temperature (T_{850}) and inversion strength variables, where inversion strength is estimated as the difference between T_{850} and near-surface (2m) temperature.

Changes in remotely sourced heat and moisture into the high latitudes are evaluated using the horizontal convergence of latent and sensible heat fluxes, $-\nabla \cdot L\mathbf{v}q$ and $-\nabla \cdot c_p\mathbf{v}T$, respectively. At a given pressure (p) level, the meridional convergence of zonal mean heat flux is then given by:

$$-\nabla_p \cdot L[\overline{vq}] = \frac{-1}{R\cos\phi}\frac{\partial}{\partial\phi}(L[\overline{vq}]\cos\phi) \tag{3.1}$$

$$-\nabla_p \cdot c_p[\overline{vT}] = \frac{-1}{R\cos\phi}\frac{\partial}{\partial\phi}(c_p[\overline{vT}]\cos\phi) \tag{3.2}$$

where L is the latent heat of vaporization (2.51×10^6 J kg^{-1}), c_p is the specific heat capacity of air at constant pressure (1004 J kg^{-1} K^{-1}), v is meridional wind, q is specific humidity, R is Earth's radius, ϕ is latitude, brackets denote a zonal mean, and overbars denote a time average. Diagnostic variables $\overline{vq}$ and $\overline{vT}$ are calculated online during simulation at each model time step (30 minutes) to take cyclonic effects into account, then saved as monthly means. However, analogous transport terms involving geopotential height and zonal wind are not provided for CESM1-LE. Due to this data limitation, we neglect the geopotential energy contribution to dry static energy flux convergence (Eqn. 3.2), which contributes approximately 29% of the annual mean convergence in the Arctic troposphere (Cardinale et al. 2021). Since we use zonal means in Eqns. 3.1 and 3.2, the averaging domain for our two transport terms must be defined in terms of latitude (Table 3.1). Finally, we neglect the latent heat of freezing for the case of solid precipitation (Eqn. 3.1), following prior assessments of Arctic latent heat flux convergence in CESM1 (Graversen and Langen 2019).

Climatological, mass-weighted vertical profiles of the two heat flux convergence components, as well as their distinct responses to RCP8.5 forcing, are shown in Figure 3.1b,c. In the Arctic midtroposphere (800-400 hPa), increases in latent heat flux convergence (Eqn. 3.1) occur in every season over the 21st century, with ensemble-mean changes on the order of 1 Wm^{-2} (Fig. 3.1b). Sensible heat flux convergence (Eqn. 3.2) trends are largest between 950 and 600 hPa, with ensemble-mean decreases on the order of 10 Wm^{-2} that are largest in winter and

spring (Fig. 3.1c). The forced changes in latent heat flux convergence are more robust, despite their smaller magnitude, because the forced changes in sensible heat flux convergence lie largely within the internal variability. Taken together, midtroposphere changes reflect a large-scale response to anthropogenic forcing, where latent heat flux convergence follows a strengthened meridional humidity gradient (not shown) and sensible heat flux convergence follows a weakened meridional temperature gradient (Fig. 3.1a). At lower altitudes, below 800 hPa, decreases in net heat flux convergence suggest an additional influence from local surface conditions. For instance, the atmospheric response to sea-ice loss has been connected to enhanced local moisture export from the Arctic (Singh et al. 2017) and equatorward mixing of thermal anomalies over adjacent continents (Deser et al. 2010), consistent with the change from sensible heat flux convergence to divergence in winter under RCP8.5 forcing (Fig. 3.1c). We aim for our causal networks to evaluate changes in heat and moisture at heights where RCP8.5 trends are largest. The networks therefore employ time series of latent heat flux convergence at 500 hPa and sensible heat flux convergence at 850 hPa. For both components, Arctic heat flux convergence is defined as the average over 70°-90°N, following prior research on atmospheric energy transport in CESM1 (Graversen and Langen 2019).

Sea-ice extent is defined in terms of its total Northern Hemisphere surface area, which is calculated as an area-weighted sum of grid cell sea-ice concentration. The change in sea-ice extent over the 21st century is shown in Figure 3.2a for the ensemble mean. By 2100, fall (SON) sea-ice coverage is completely lost in the Northern Hemisphere (< 0.1 million km^2) for all ensemble members, while the central Arctic remains ice-covered in the remaining seasons. Spring (MAM) retains

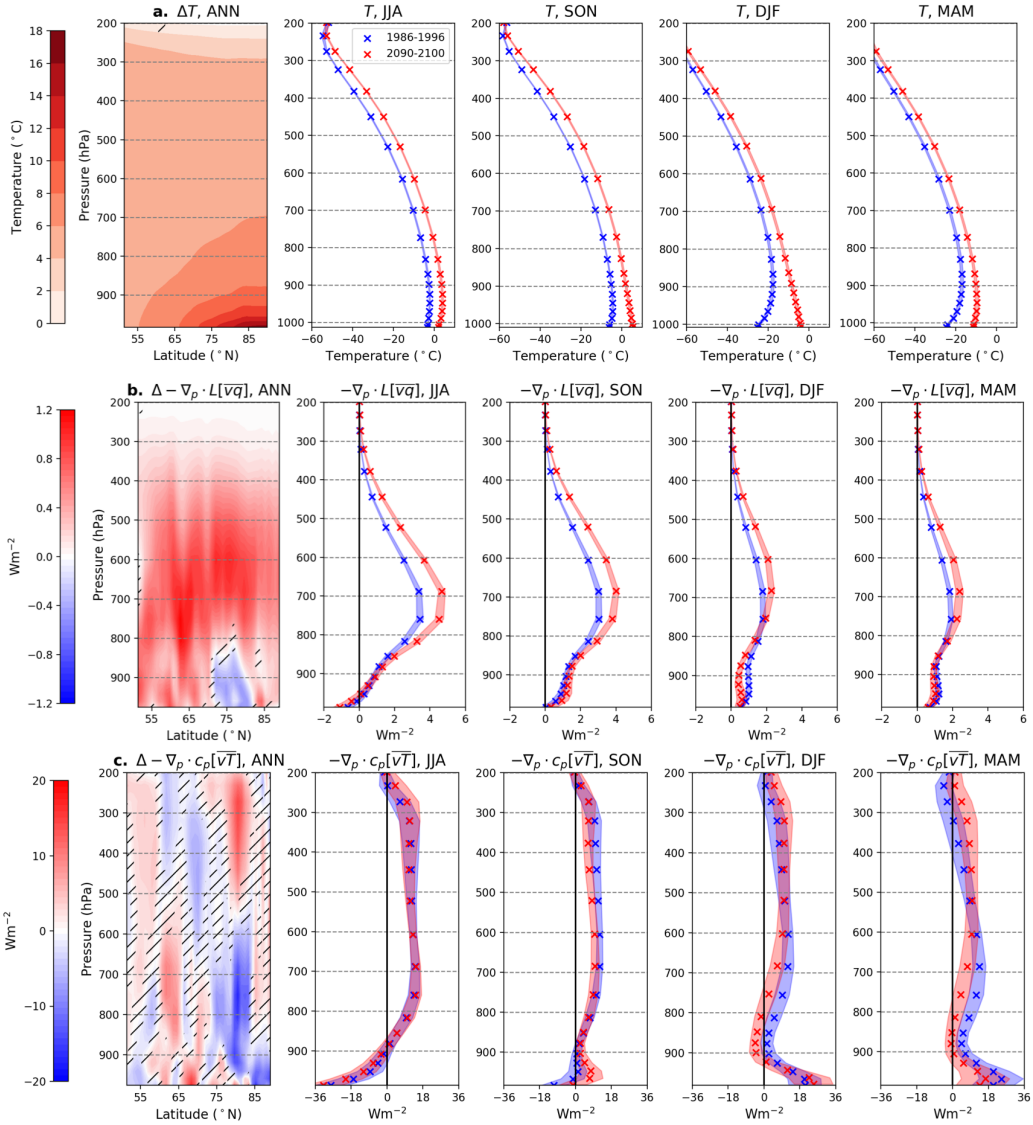

Figure 3.1: The 21st century, RCP8.5-forced change in (a) atmospheric temperature (T), (b) zonal-mean latent heat flux convergence ($-\nabla_p \cdot L[\overline{vq}]$), and (c) zonal-mean sensible heat flux convergence ($-\nabla_p \cdot c_p[\overline{vT}]$) in the Community Earth System Model, Large Ensemble (CESM-LE).The leftmost column shows the extratropical zonal-mean, annual-mean difference between the 2090-2100 and 1986-1996 climatologies, where color represents the ensemble-mean change, and hatching represents regions where the forced change is insignificant compared to internal variability (two-sided Student's t-test, $p = 0.05$). The remaining columns show the Arctic-average (as defined in Table 3.1) climatologies in 1986-1996 (blue) and 2090-2100 (red) for each season, where x's indicate the ensemble mean and envelopes indicate the ensemble spread ($\pm$ 2σ). In (b) and (c), heat flux convergences are mass-weighted by the pressure thickness ($\frac{dp}{g}$) at each model level (hybrid sigma coordinates).

the largest sea-ice area in 2100 (12.3 - 14.2 million km^2), largely due to slower melt rates relative to summer (JJA) and winter (DJF). To coherently assess the atmospheric response to sea-ice loss, all surface and lower-tropospheric variables are averaged over ocean areas with at least 15% sea ice in the 1986-1996 annual mean (black line, Fig. 3.2). This limitation excludes high-latitude regions that are perennially ice free at the start of the 21st century, but includes areas that become seasonally ice free under RCP8.5 forcing (blue regions, Fig. 3.2a). All regimes within this spatial domain feature an increase in surface heat uptake in summer (JJA, Fig. 3.2b) and release to the atmosphere in fall and winter (SON and DJF, Fig. 3.2b). Decreases in inversion strength closely follow the increases in upward surface heat flux (SON and DJF, Fig. 3.2c), which occur poleward of the climatological ice edge. Significant inversion strength changes thus take place over both regions that are ice-covered (i.e., the central Arctic) and ice-free (i.e., Hudson Bay) by 2100. This spatial pattern of surface and lower-tropospheric changes are robust across ensemble members and across smaller thresholds for defining the ice line (5% and 10%, not shown).

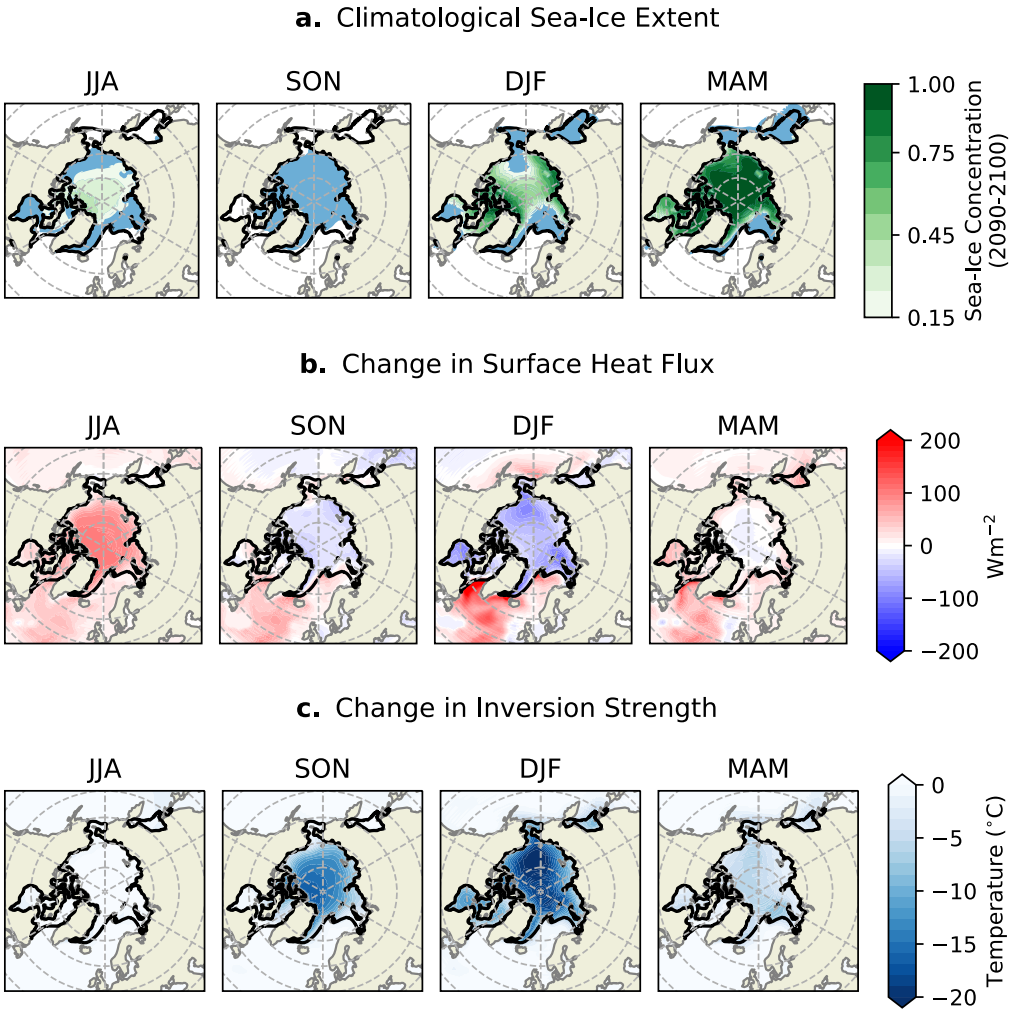

Figure 3.2: The 21st century, RCP8.5-forced change in (a) sea-ice extent, (b) net surface heat flux (SW_{net} - LW_{net} - Turbulent Heat Flux; positive down), and (c) boundary layer inversion strength (T_{850} - T_{2m}) over ocean regions in the Community Earth System Model, Large Ensemble (CESM-LE). In all maps, the black line represents the annual mean, ensemble mean sea-ice edge at the start of the study period (1986-1996), which corresponds to the spatial averaging domain defined in rows 3-10 of Table 3.1. In (a), the 2090-2100 ensemble-mean climatological sea-ice concentration is shown with green contours for each season. Blue regions indicate where seasonal sea ice concentrations are greater than 15% in the 1986-1996 climatology. In (b) and (c), ensemble mean changes in surface heat flux (b) and inversion strength (c) are shown as the difference between the 2090-2100 and 1986-1996 climatologies. Latitude circles (dashed) are shown in 10° intervals for 50°-90°N.

For the causal network inputs listed in Table 3.1, the surface energy budget is described using five variables. The sum of surface sensible and latent turbulent

heat fluxes provide the first surface variable, upward turbulent heat flux. The second and third surface time series represent the shortwave radiation budget: net shortwave radiative flux at the surface and shortwave (SW_{net}) cloud radiative effect (SW_{CRE}), with the latter quantity calculated as the difference between all-sky and clear-sky net surface shortwave flux. Net longwave surface flux (LW_{net}) and cloud radiative effect (LW_{CRE}) are calculated similarly to the shortwave variables, where a positive LW_{CRE} is a surface warming tendency, consistent with the climatological effect of Arctic clouds. Throughout this study, all surface energy budget terms are defined as positive down (into the surface).

3.2.2 Causal Networks

Causal networks are constructed from the ten aforementioned time series, using a linear application of Pearl's causal effect theory (Pearl 2013; Runge et al. 2015a). To compare the impact of local and remote warming sources simultaneously, we must select a temporal resolution that accommodates both the short (daily) timescale of variability for midtroposphere heat flux convergence, as well as the longer (monthly) timescale of variability for Arctic sea-ice extent. We find that averaging daily CESM-LE output into weekly (i.e., quarter-monthly, as in Kretschmer et al. (2016)) timesteps best accomplishes this goal. Assessing causal relationships also requires stationary time series input, so we next remove the anthropogenic trend from each variable. The trend is estimated as a second-order polynomial and subtracted from the data, applied separately for each week in the seasonal cycle. Then, each variable is divided by its standard deviation. The resulting time series input consists of weekly standardized anomalies with constant mean

and variance, shown in Figure 3.3 for a characteristic ensemble member. Temporal periodicity remains present when there are large seasonal differences in the magnitude of anomalies, which is especially apparent in the shortwave surface fluxes (Fig. 3.3f,g). This seasonality is a key consideration throughout our analysis. In general, anomalies are an order of magnitude smaller than CO_2-forced trends over 1986-2100. Sensible heat flux convergence (Fig. 3.3a) is the one exception to this relationship, as its 21st century trends are smaller than its anomalies. The process of constructing causal networks from these time series occurs in two phases. First, we identify the robust, time-lagged causal relationships between each variable in a CESM ensemble member. Then, we quantify causal effects using a linear vector autoregressive (VAR) model.

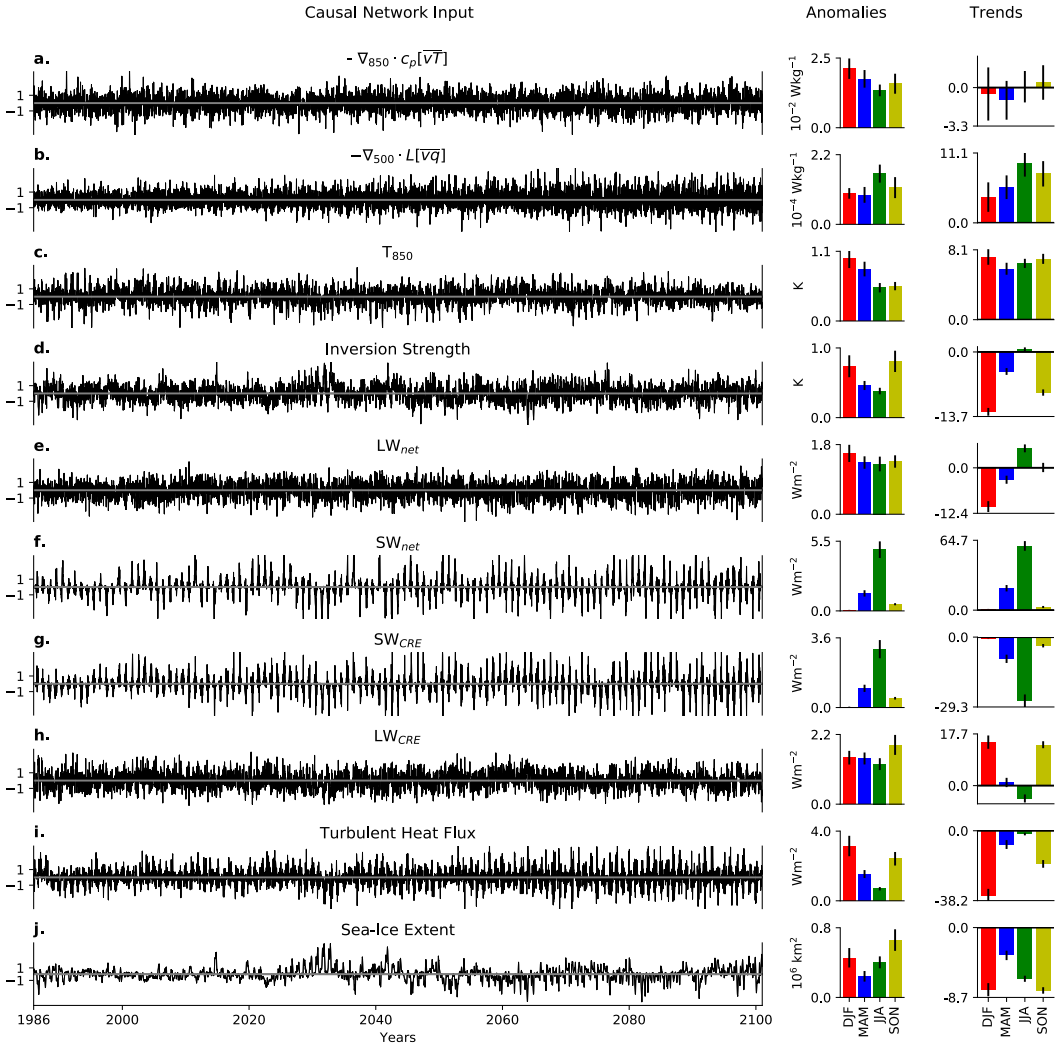

Figure 3.3: Weekly time series of causal network inputs, standardized and detrended, shown for a characteristic ensemble member in the Community Earth System Model, Large Ensemble (CESM-LE). Rows a-j represent the spatially averaged variables defined in Table 3.1. For each variable, barplots display the magnitude of ensemble-mean 1σ anomalies and RCP8.5 trends (1986-2100) for each season. Barplot errorbars represent the ensemble spread, calculated as in Figure 3.1. Trends in all surface energy budget terms (rows e-i) are signed positive down (into the surface). Note that mass weighting is not applied to sub-monthly heat flux convergences (rows a and b), so trends and anomalies are shown in W kg^{-1}. Products $\overline{vq}$ and $\overline{vT}$ are calculated as weekly averages from daily diagnostic output for v,q, and T at 850 hPa and 500 hPa.

Causal links between each variable are identified using the PC-algorithm

adapted for time series, named after its creators Peter Spirtes and Clark Glymour (PC-Stable, Spirtes et al. 2000). For each input variable, the algorithm begins by calculating every possible time-lagged linear auto-correlation and cross-correlation over a pre-determined time window, or maximum lag ($\tau_{\max}$). The linear lagged correlation measure is defined as:

$$\rho(X_i(t-\tau), X_j(t)) \tag{3.3}$$

where ρ is the Pearson correlation coefficient, τ is a time lag (weeks), $X_j(t)$ is one of the ten input time series variables defined in Section 3.2.1, and $X_i(t-\tau)$ are lagged time series with a potential causal influence on $X_j(t)$. Contemporaneous links are not considered in this study. The significance of ρ is assessed with a pre-defined significance threshold, α, and if ρ is found to be insignificant, then we conclude that $X_i(t-\tau)$ does not cause $X_j(t)$ and remove it from the set of possible links. We test several values for α and find $\alpha = 0.01$ provides the optimal balance between network simplicity and network connectivity. Our choices for $\tau_{\max}$ are discussed in Section 3.3.1.

While $X_i(t-\tau)$ may be unconditionally correlated with $X_j(t)$, the relationship could be confounded by the influence of another network variable. Therefore, after the initial lagged correlation test, the PC-algorithm tests the remaining significant links a second time, conditioned on the influence of a third process, Z_1:

$$\rho(X_i(t-\tau), X_j(t)|Z_1) \tag{3.4}$$

where $Z_1 \neq X_i(t-\tau)$ is the auto or cross-link possessing the strongest unconditional correlation with $X_j(t)$ in Eqn. 3.3. The vertical line in Eqn. 3.3 denotes removing the linear influence of Z_1 from both $X_i(t-\tau)$ and $X_j(t)$ and testing the correlation

between their residuals. If Z_1 makes the formerly significant link insignificant, the two variables are said to be conditionally independent, and the link is subsequently removed. This process is repeated over n iterations by adding an increasingly stringent number of conditions, Z_2, Z_3, ..., Z_n to the partial correlation tests until no more links can be removed. The PC-algorithm finishes when it converges to a final set of significant links for each variable, which are subsequently considered the causes of $X_j(t)$. This designation is based on the causal Markov condition, which states that X_j is independent of all network variables, except X_j's effects, when conditioned on the causes of X_j (Spirtes et al. 2000). The PC-algorithm thus accounts for all indirect and confounding causal connections in the complex network, assuming all relevant variables for the system are included. This assumption, which is usually violated to some degree in practice, emphasizes the importance of the variable selection process, as well as the need for prior physical knowledge about the system in question.

Finally, after uncovering each variable's causal predictors with the PC-algorithm, we quantify causal effects following Runge et al. (2015a), using a VAR model:

$$\mathbf{X}(t) = \sum_{\tau=1}^{\tau_{\max}} \Phi(\tau)\mathbf{X}(t-\tau) + \epsilon_t \tag{3.5}$$

where $\mathbf{X}$ is a vector of shape (N, t) containing time series for N variables, Φ is a standardized regression coefficient matrix of shape $(N, N, \tau_{\max})$, and ϵ_t are independent, identically distributed error terms, which describe the uncorrelated probability distributions of each causal network variable's anomalies (Fig. 3.3). An individual regression coefficient, or link coefficient, $\Phi_{j,i}(\tau)$, indicates the expected change in

variable $X_j(t)$ caused by a hypothetical 1σ perturbation in $X_i(t-\tau)$ with all other variables held constant. $\tau_{\max}$ refers to the time domain over which link coefficients are added. The VAR model defined in Eqn. 3.5 bears some resemblance to Green's Functions used in prior polar climate studies (Kostov et al. 2017), which quantify a climate variable's response to a hypothetical step-increase in a given forcing. However, Eqn. 3.5 additionally utilizes causal inference to account for coupled interactions modulating the response. For instance, $\Phi_{j,i}(\tau) = 0$ unless $X_i(t-\tau)$ causes $X_j(t)$, as determined by the PC-algorithm. This key feature of matrix Φ frees the VAR model from having to fit negligible parameters, thus allowing it to accommodate a large number of variables. The link coefficient structure in Φ also serves as the causal network, tracing pathways between an imposed perturbation to any variable and the expected temperature response. We construct these networks for each CESM ensemble member using Eqns. 3.3-3.5, then analyze their structure to understand the causes of the Arctic's changing temperature inversion.

A visual schematic of a causal network, as well as its associated causal effects, is shown in Figure 3.4. The total causal effect ($\mathbf{TCE}(\tau)$) of any hypothetical perturbation is calculated by iteratively computing link coefficient matrix products from a causal network (Φ, Eqn. 3.5), given by:

$$\mathbf{TCE}(\tau) = \sum_{s=1}^{\tau} \Phi(s)\mathbf{TCE}(\tau - s). \tag{3.6}$$

$TCE_{j,i}(\tau)$ represents the total causal effect of perturbed variable ($X_i(t-\tau)$) on a response variable ($X_j(t)$). It should be noted that the structure of Eqn. 3.6 and Eqn. 3.5 are similar. Eqn. 3.5 is a full description of the causal network, where regression coefficients are calculated from 1 to $\tau_{\max}$. Eqn. 3.6 highlights that causal

effects can be calculated for any lag in the network, where each effect is the sum of regression coefficients up to (and only to) that specified time lag. We also use this framework to isolate the portion of a causal effect mediated by an intermediate network variable, defined as X_k. This calculation is accomplished by first setting all link coefficients through X_k to zero in matrix Φ (Eqn. 3.5), resulting in a modified coefficient matrix, Φ^k. We then repeat the total causal effect calculation (Eqn. 3.6) with this modified matrix. The difference between the modified and unmodified calculations yields the mediated causal effect, defined as:

$$MCE^k_{j,i}(\tau) = TCE_{j,i}(\tau) - TCE^k_{j,i}(\tau) \tag{3.7}$$

where $MCE^k_{j,i}(\tau)$ represents the causal effect of $X_i(t-\tau)$ on $X_j(t)$ mediated by network variable X_k. Note that $MCE^k_{j,i}(\tau)$ is equal to $TCE_{j,i}(\tau)$ if $X_k = X_j$. Relatedly, if $X_k = X_i$, then $MCE^k_{j,i}(\tau)$ indicates the contribution of autocorrelation (memory) in the perturbation of X_i.

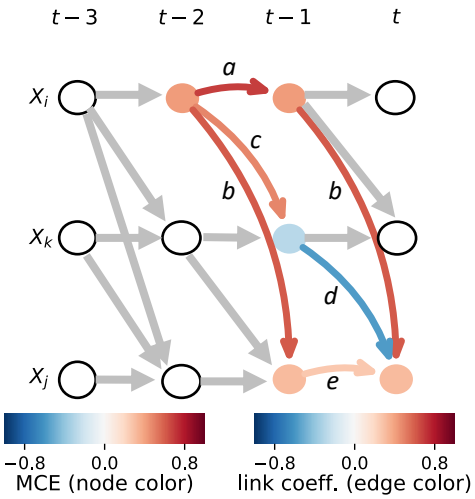

$$TCE_{j,i}(2) = ab + cd + be$$

$$MCE^{k}_{j,i}(2) = cd$$

Figure 3.4: Schematic of a causal network time series graph, as introduced in Runge et al. (2015a). Causal pathways are defined by the set of all arrows (gray and colored) and are quantified as the regression coefficient matrix of a VAR model (Φ, Eqn. 3.5) with N=3 variables (X_i,X_k,X_j) and τ_{max}= 3 weeks. Curved, colored arrows denote the specific pathways used to quantify the total causal effect of $X_i(t-2)$ on $X_j(t)$ ($TCE_{j,i}(2)$, Eqn. 3.6) and the causal effect mediated by intermediate variable X_k ($MCE^{k}_{j,i}(2)$, Eqn. 3.7). In this example, the link coefficient pathway quantifying MCE (cd, blue node at $X_k(t-1)$) reduces the magnitude of TCE (ab + cd + be) because the effects are opposite in sign. Many potential causal links aren't shown, as they are deemed insignificant by the PC algorithm (Eqs. 3.3 and 3.4) and excluded from the causal network, such as X_j causing X_k at any lag. Note that the color of affected nodes is constant for each variable (row), as it corresponds to MCE solely for the lag where the perturbation is initiated (t-2, in this case).

3.3 Results

3.3.1 The Causal Effect of Enhanced Arctic Heat Flux Convergence and Sea-Ice Loss

In our causal networks, we track remote Arctic warming sources by imposing a hypothetical $+1\sigma$ step increase in 500 hPa Arctic latent heat flux convergence ($-\nabla_{500} \cdot L[\overline{vq}]$) and a -1σ step decrease in sensible heat flux convergence ($-\nabla_{850} \cdot c_p[\overline{vT}]$), with the sign of the perturbations reflecting 21st century anthropogenic trends (Fig. 3.1b,c). Similarly, a -1σ step decrease in sea-ice extent is used to track the local impact of sea-ice loss. The magnitude of perturbations is equivalent to the annual standard deviation of each detrended time series variable. The total causal effect of each perturbation on 850 hPa Arctic temperature and inversion strength is shown in Figure 3.5. To account for the seasonality of Arctic warming, we calculate these causal effects after four separate implementations of the PC-algorithm, where the response variables (850 hPa temperature or inversion strength) are masked to only include data from summer (JJA), fall (SON), winter (DJF), and spring (MAM), respectively, following the approach of (Kretschmer et al. 2016). Network regression coefficients are fit for each season using Eqns. 3.3-3.5. Then, causal effects are calculated at each time lag using Eqn. 3.6. The causal effects analyzed in this section represent the time-lagged linear response of Arctic temperatures to an instantaneous step change in sea ice and/or poleward heat transport. Given the use of detrended time series data, these hypothetical step changes do not describe the transient temperature response to CO_2-forced changes. However, they nonetheless offer the advantage of isolating the impact of individual processes on

the lower troposphere in a fully coupled setting.

In Figure 3.5a, the total causal effect of enhanced latent heat flux convergence ($+1\sigma\ -\nabla_{500} \cdot L[\overline{vq}]$) is shown at lags of one to four weeks ($\tau = 1$ to $\tau_{\max} = 4$) for each CESM ensemble member, where our choice of $\tau_{\max}$ follows the observed timescale of moist intrusions into the Arctic (Woods et al. 2013). One week following a $+1\sigma$ step increase in latent heat flux convergence, the Arctic atmosphere responds by warming at 850 hPa in all seasons (black curves), with the total causal effect ($TCE_{j,i}(1)$) ranging from .077 K in summer to .25 K in winter for the ensemble mean. This response then quickly decays in the subsequent three weeks, reflecting the short timescale of the atmospheric perturbation. The initial warming impact at 850 hPa is robust, being detected in all forty CESM ensemble members. A similarly robust impact on boundary-layer inversion strength (green curves) is found in summer, fall, and winter. In summer, the inversion's response to latent heat flux convergence is similar to the 850 hPa temperature response, which indicates little-to-no warming near the surface. In summer, it is likely that an anomalous downward longwave radiation flux to the surface, associated with the 850 hPa temperature change, goes into sea-ice melt rather than warming. This mechanism is further detailed in the following section. In fall and winter, however, the initial ($\tau = 1$) positive inversion strength response is weaker than the 850 hPa temperature response. Furthermore, after four weeks ($\tau = 4$), the inversion strength response switches from positive to weakly negative in some CESM ensemble members, especially in winter. This change in sign implies that a secondary warming response to latent heat flux convergence appears near the Arctic surface. The near-surface warming response begins weaker than the 850 hPa warming response, but eventually exceeds 850 hPa

warming after four weeks. This fall/winter temperature response follows a similar timeline to prior observation-based studies of Arctic moist intrusions (Woods and Caballero 2016a): the temperature response is initially slower at the surface than in the troposphere, but the situation eventually reverses. Such related studies have focused strictly on strong, highly localized moist intrusions, which produce surface temperature anomalies up to an order of magnitude larger than the warming tracked by our causal effect networks. The moist transport perturbations in this study are less strictly defined, as our networks track the response to any positive anomaly in Arctic-averaged latent heat flux convergence at 500 hPa. In spring, the inversion strength response to latent heat flux convergence is weak or insignificant (i.e., zero), with causal effects detected in only half of CESM ensemble members.

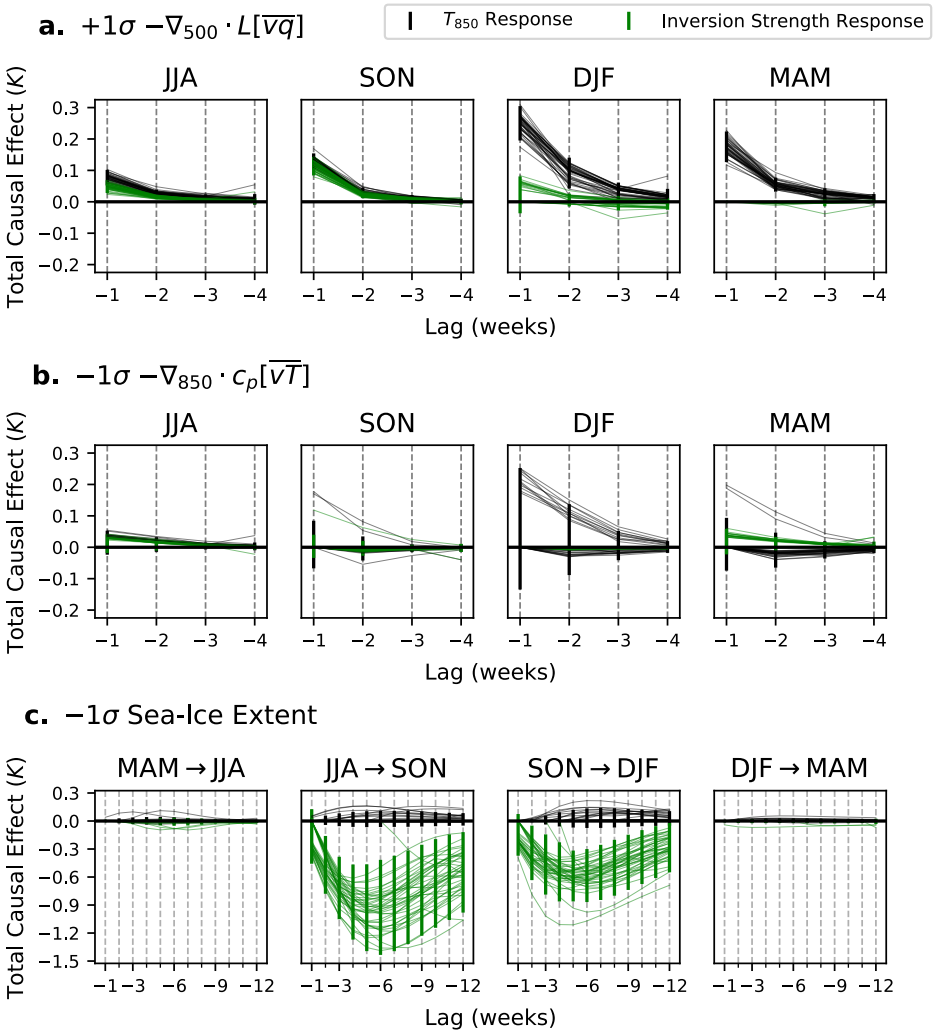

Figure 3.5: The predicted change in Arctic atmospheric temperature caused by (a) an imposed $+1\sigma$ step increase in 500 hPa Arctic latent heat flux convergence ($-\nabla_{500} \cdot L[\overline{vq}]$), (b) a -1σ step decrease in 850 hPa sensible heat flux convergence ($-\nabla_{850} \cdot c_p[\overline{vT}]$), and (c) a -1σ step decrease in sea-ice extent. In (a) and (b), the 850 hPa temperature response (T_{850}, black) and boundary-layer inversion strength response (green) are shown for perturbations at one to four week lags in summer (JJA), fall (SON), winter (DJF) spring (MAM). In (c), the temperature responses are shown for perturbations at one to twelve week lags, across each seasonal transition (note the different y-axis scaling). Curves display the causal effects for individual ensemble members, if they are non-zero. At each time lag, vertical error bars denote the spread in estimated causal effect ($\pm$ 2σ) across 40 CESM ensemble members, where insignificant causal effects are defined as zero.

The total causal effect of weakened sensible heat flux convergence is shown in Figure 3.5b (-1σ $-\nabla_{850} \cdot c_p[\overline{vT}]$) for the same time lags. In all seasons, fewer en-

semble members detect a significant causal impact on Arctic temperatures, and the significant causal effects are generally smaller in magnitude and inconsistent in sign. For instance, 11 out of 40 ensemble members detect a wintertime 850 hPa warming response to weakened sensible heat flux convergence, while the remaining ensemble members detect a cooling effect or no effect at all. The causal effect signal is even weaker if sensible heat transport is instead evaluated in the midtroposphere instead of at 850 hPa (-1σ $-\nabla_{500} \cdot c_p[\overline{vT}]$, Fig. S1). Sensible heat flux convergence anomalies only cause robust temperature changes when they are evaluated on shorter (daily) timescales, where, with the exception of spring (MAM), decreases in sensible heat flux convergence partially compensate the opposite-signed impacts of a latent heat flux convergence increase (Fig. S2). Therefore, our networks suggest that Arctic sensible heat flux convergence anomalies have small impacts on lower-tropospheric temperature on sub-monthly timescales. Instead, temperatures are more sensitive to the latent component (Fig. 3.5a). This result is somewhat counterintuitive, given the relative magnitudes of climatological heat flux convergences (Fig. 3.1b,c). However, prior energy budget analyses have suggested that latent energy transport influences Arctic climate more strongly than dry static energy transport (Graversen and Burtu 2016; Yoshimori et al. 2017). The total causal effects shown in Figure 3.5a,b are consistent with these findings and are robust to tests that use a more equatorward spatial averaging boundary (60°-90°N, Fig. S3). The mechanism determining the differential warming impacts are explored in Section 3.3.2.

We expect a -1σ step decrease in sea-ice extent to influence Arctic temperatures over a longer time range compared to the atmospheric perturbations in Figure 3.5a,b. We therefore calculate the total causal effect of sea-ice loss over a

longer range of time lags, up to twelve weeks ($\tau_{\max} = 12$). Since more time elapses between a hypothetical sea-ice perturbation and the expected Arctic warming response, causal networks with $\tau_{\max} = 12$ capture the influence of sea-ice loss across seasons. This interseasonal influence is shown with the total causal effects in Figure 3.5c. Here, most CESM ensemble members detect causal effects from sea-ice loss in the summer-to-fall (JJA→SON) and fall-to-winter (SON→DJF) transitions, demonstrating a link between fall/winter Arctic temperature changes and sea-ice loss in the preceding melt season. During these seasonal transitions, the Arctic warming response to sea-ice loss peaks four-six weeks after the imposed perturbation, where ensemble-mean 850 hPa temperature changes are comparable in magnitude to those caused by enhanced latent heat flux convergence (Fig 3.5a). However, the causal effect of sea-ice loss at 850 hPa is dwarfed by concurrent decreases in boundary-layer inversion strength, with total causal effects at $\tau = 6$ ranging from 0.5K - 1.5K. The inversion strength response indicates a larger warming response to sea-ice loss near the surface. Similar results are obtained when testing causal effects at coarser time resolution ($\tau_{\max} = 12$ months, not shown), where causal effects are largely confined to lags of 1-4 months, consistent with Figure 3.5c.

In summary, the perturbations imposed to our causal networks demonstrate that 850 hPa warming is caused by both sea-ice loss (Fig. 3.5c) and enhanced latent heat flux convergence in the Arctic midtroposphere (Fig. 3.5a). All else being equal, 850-hPa warming increases the strength of the Arctic's boundary-layer temperature inversion. However, these causal effects are outweighed by strong near-surface warming caused primarily by sea-ice loss in the melt season, which weakens the temperature inversion in fall and winter. Even though anthropogenic trends

are removed from our network time series, the seasonality of the total causal effects in Figure 3.5 are similar to the seasonality of surface-amplified warming under RCP8.5 forcing (Fig. 3.1a). The inversion strength response to -1σ sea-ice perturbations is approximately an order of magnitude smaller than the twenty-first century changes simulated in CESM1-LE (Fig. 3.5c, Fig. 3.3d), but this difference is consistent with sea-ice perturbations being similarly small in comparison to projected sea-ice loss (Fig. 3.3j). The causal effects therefore suggest that the Arctic vertical warming structure shown in Figure 3.1a can be produced by the cumulative impact of seasonal sea-ice retreat over many years, until the Arctic becomes ice free. Similarly, projected twenty-first century increases in midtroposphere latent heat flux convergence are approximately a factor of five larger than imposed causal network perturbations (Fig. 3.3b), implying that the cumulative impact of many moist transport events are a significant driver of Arctic temperature trends at 850 hPa, especially in winter and spring (Fig. 3.5a, Fig. 3.3c).

Finally, it is important to note that the spatial domain of our causal networks includes both ice-covered and ice-retreat regions at the end of the 21st century (Fig 3.2a). Accordingly, we additionally explore the extent to which the inversion strength response to sea-ice loss is related to weaker inversions over sea ice or to the exposure of newly open ocean. We test the sensitivity of our causal effects to open-ocean exposure by assessing sea-ice loss over ice-covered and ice-retreat regimes only (Fig. S4). The sensitivity test shows that weaker inversions do occur over sea ice, and do not require the appearance of open ocean. This result is consistent with related research that found positive Arctic lapse rate feedbacks over both ice-covered and ice-retreat regions across CMIP5 (Boeke et al. 2020).

3.3.2 The Mediating Role of Surface Energy Fluxes

After quantifying the Arctic temperature response to causal network perturbations, we identify which parts of the surface energy budget mediate the temperature response to latent heat flux convergence and sea-ice loss, respectively. Examining these causal pathways in greater detail reveals the physical mechanisms connecting atmospheric heat transport and sea-ice loss to Arctic warming. For each perturbation introduced in section 3.3.1, we calculate the causal effect mediated by each energy budget term. We use Eqn. 3.7 to identify the key mediating pathways in each causal network at $\tau_{\max}$= 4 weeks for latent heat flux perturbations (corresponding to Figure 3.5a, Figure 3.6), and at $\tau_{\max}$= 12 weeks for sea-ice loss perturbations (corresponding to Figure 3.5c, Figure 3.7). We focus on the most important mediating pathways, where $MCE^{k}_{j,i}(\tau)$ is non-zero for a majority ($> 50\%$) of CESM ensemble members. Then, we visualize the causal pathways in a directed time series graph (right-hand panels of Fig. 3.6 and Fig. 3.7), which depicts the causal structure for a characteristic ensemble member. Each ensemble member may feature distinct causal pathways that are not seen in other members. Accordingly, the best visual aid is provided by a characteristic causal network that features the most common mediating effects. We limit this analysis to the fall and winter implementations of the PC-algorithm, as these seasons feature robust causal effects from both enhanced latent heat flux convergence (Fig. 3.5a) and sea-ice loss (Fig. 3.5c). During these seasons, we find that causal effects of each perturbation are mediated by changes in both turbulent and longwave heat fluxes at the surface, while changes in the shortwave energy budget play no significant role.

The variables mediating the 850 hPa temperature response to enhanced latent heat flux convergence are shown in Figure 3.6a,b and the variables mediating the inversion strength response are shown in Figure 3.6c,d at a lag of four weeks. As noted in the previous section, the total causal effect of latent heat transport is typically positive (warming) at 850 hPa (gray-shaded row of Fig. 3.6a) in both fall and winter, while the inversion strength response features both weakly positive (strengthening) and negative (weakening) causal effects across the CESM ensemble (gray-shaded row of Fig. 3.6c). The total response in each temperature variable is explained by the mediating impact of progressive changes in the surface longwave radiative flux and sea-ice extent. Initially, both T_{850} and inversion strength feature a direct, positive response to $-\nabla_{500} \cdot L[\overline{vq}]$, which is damped by the negative autocorrelation (memory) of the atmospheric perturbation in subsequent weeks (Fig. 3.6b,d). Therefore, the total effect in grey shading (row 3, Fig. 3.6a) can be regarded as the direct impact of latent heat flux convergence on T_{850}, minus the negative impacts of autocorrelation (row 2, Fig. 3.6a) and the mediating effect of $\mathrm{LW}_{\mathrm{net}}$ (row 4, Fig. 3.6a). In Figure 3.6c,d, the initial strengthening of the inversion is also accompanied by a reduction of net longwave cooling at the surface. The decrease in longwave cooling then causes sea ice to melt, in turn weakening the inversion strength (Fig. 3.6d) through near-surface warming. Consequently, after 4 weeks, near-surface warming exceeds 850 hPa warming in a majority of CESM ensemble members, and inversion strength has decreased below its initial value (Fig. 3.6c).

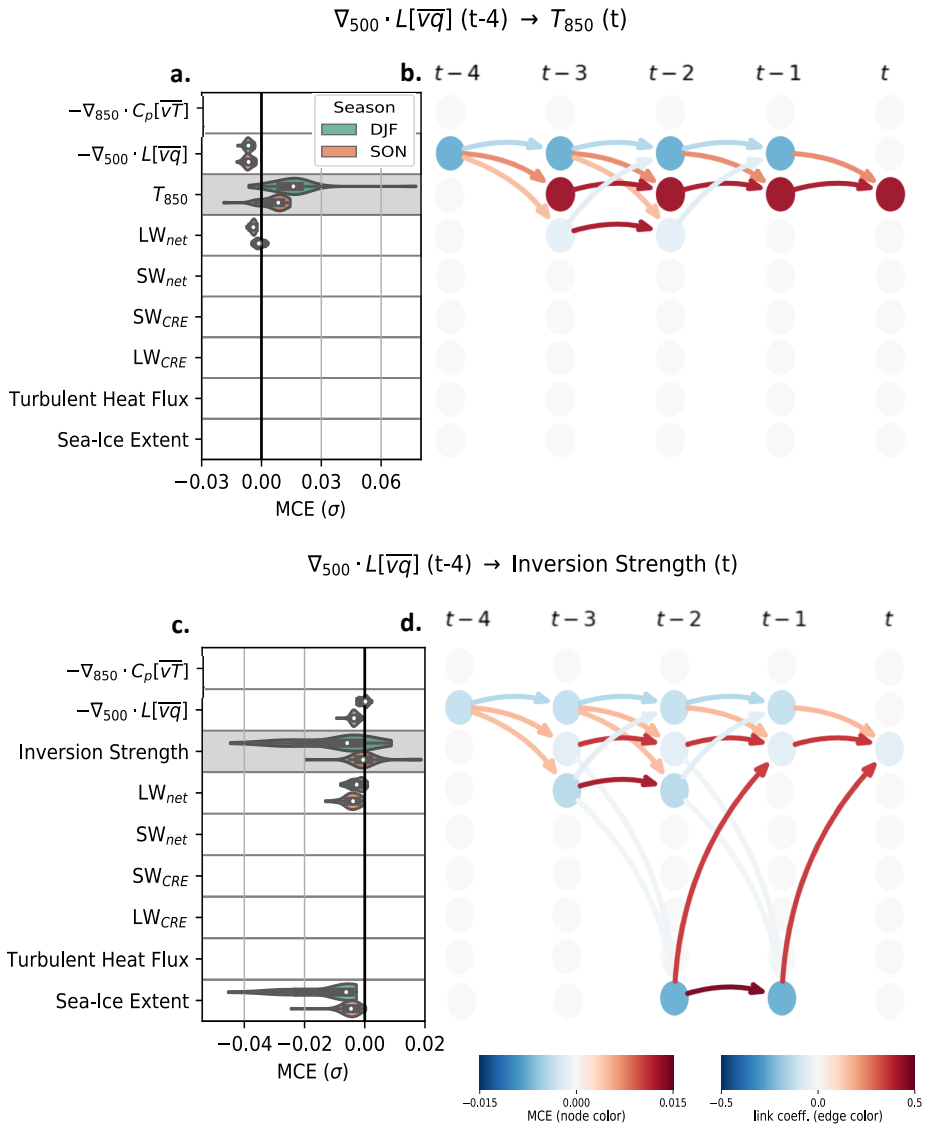

Figure 3.6: Causal pathways mediating the response of 850 hPa Arctic temperature T_{850} (a,b) and inversion strength (c,d) to an imposed $+1\sigma$ step increase in 500 hPa Arctic latent heat flux convergence ($-\nabla_{500} \cdot L[\overline{vq}]$) at a lag of four weeks. Panels (a) and (c) show the distribution of mediated causal effects in fall (SON) and winter (DJF) using violin plots, where white circles indicate a median, whiskers indicate an interquartile range, and colors indicate a probability distribution function, calculated as a non-parametric kernel density estimate. Mediated causal effects are only shown if they are non-zero in a majority ($> 50\%$) of CESM ensemble members. Note that causal effects mediated by T_{850} and inversion strength (gray-shaded row in a,c) are equivalent to the total causal effects shown in Figure 3.5a at τ_{max}=4 weeks. Panels (b) and (d) illustrate mediating causal pathways in a time series graph for CESM ensemble member 12 in fall.

The magnitude of the indirect causal effect on inversion strength varies by season. The distribution of mediated causal effects of sea-ice loss on inversion strength features larger (more negative) values in winter than in fall (compare green and orange distributions, Figure 3.6c). In other words, the total causal effect of enhanced latent heat flux convergence produces more greatly weakened temperature inversions in winter than in fall. This result suggests that latent heat transport activates a local water vapor feedback, whereby moisture increases longwave opacity in the Arctic atmosphere, warms the surface, and melts sea ice. This water vapor greenhouse effect characterizes both the reduction in net longwave surface cooling and the resultant sea-ice loss seen in Figure 3.6d. A minority of ensemble members additionally detect a mediating role for longwave cloud radiative effect in the causal pathways (row 7, Fig. 3.6a,c, effects not shown), which may represent the transition from a "radiatively clear" to a "cloudy opaque" state in the Arctic boundary layer following a moist intrusion event (as previously highlighted in Stramler et al. (2011) and Yoshimori et al. (2017)).

Using the same visual representation, Figure 3.7 highlights the surface energy fluxes that mediate the Arctic temperature response to a sea-ice perturbation (-1σ) in the summer-to-fall and fall-to-winter transitions, at a lag of twelve weeks. As expected, the sea-ice perturbation features large, positive autocorrelation compared to the transport perturbation in Figure 3.6, and the effects are sustained through the entirety of the time domain in the causal networks. In the first week following a -1σ perturbation, sea-ice loss causes an increase in surface longwave cloud radiative effect ($\mathrm{LW_{CRE}}$) and upward turbulent heat fluxes (t-11, Fig. 3.7b), which then mediate the eventual 850 hPa temperature response. After six weeks,

these two primary mediating effects are supplemented by small changes in net longwave surface cooling and midtroposphere latent heat flux convergence (not shown). The latter effect is most likely associated with a poleward transport of moisture from marginal ice zones toward even higher latitudes, where the enhanced moisture supply originates from newly open ocean following a negative sea-ice extent anomaly. The cloud and turbulent heat flux changes typically facilitate a warming response at 850 hPa, but the ensemble-mean response is weaker in the summer-to-fall transition, where a small subset of ensemble members feature weak cooling instead (orange distribution, Fig. 3.7a). Hence, the sign and magnitude of the 850 hPa temperature response is strongly linked to the seasonal mediated causal effects. The seasonal difference is particularly strong for the longwave cloud radiative effect, which tends to produce more 850 hPa cooling in the summer-to-fall transition and more 850 hPa warming in the fall-to-winter transition. However, clouds still facilitate summer-to-fall warming in some CESM ensemble members, as is the case for the example in Figure 3.7b.

The weakened boundary-layer inversion response to sea-ice loss (Fig. 3.7c,d) is shaped by the same surface energy flux changes as the 850 hPa temperature response (Fig. 3.7a,b), but in a different manner. In both the summer-to-fall and fall-to-winter transitions, enhanced turbulent heat fluxes and longwave cloud radiative effect serve to counteract the negative total causal effect on inversion strength (Fig. 3.7c). In other words, the increase in upward surface energy fluxes that accompany sea-ice loss reduce the weakening of the temperature inversion. This mediating effect is accomplished by facilitating heat transfer from the near-surface to 850 hPa, consistent with the RCP8.5-forced changes in surface heat flux shown in Figure 3.2b

and Figure 3.3i. The radiative impact of clouds also appears to reduce the surface-amplified warming response to sea-ice loss, despite seasonal differences in the sign and magnitude of their impact at 850 hPa (Fig. 3.7a). In the following section, we attribute these seasonal differences to the vertical structure of cloud properties and associated changes in atmospheric heating rates.

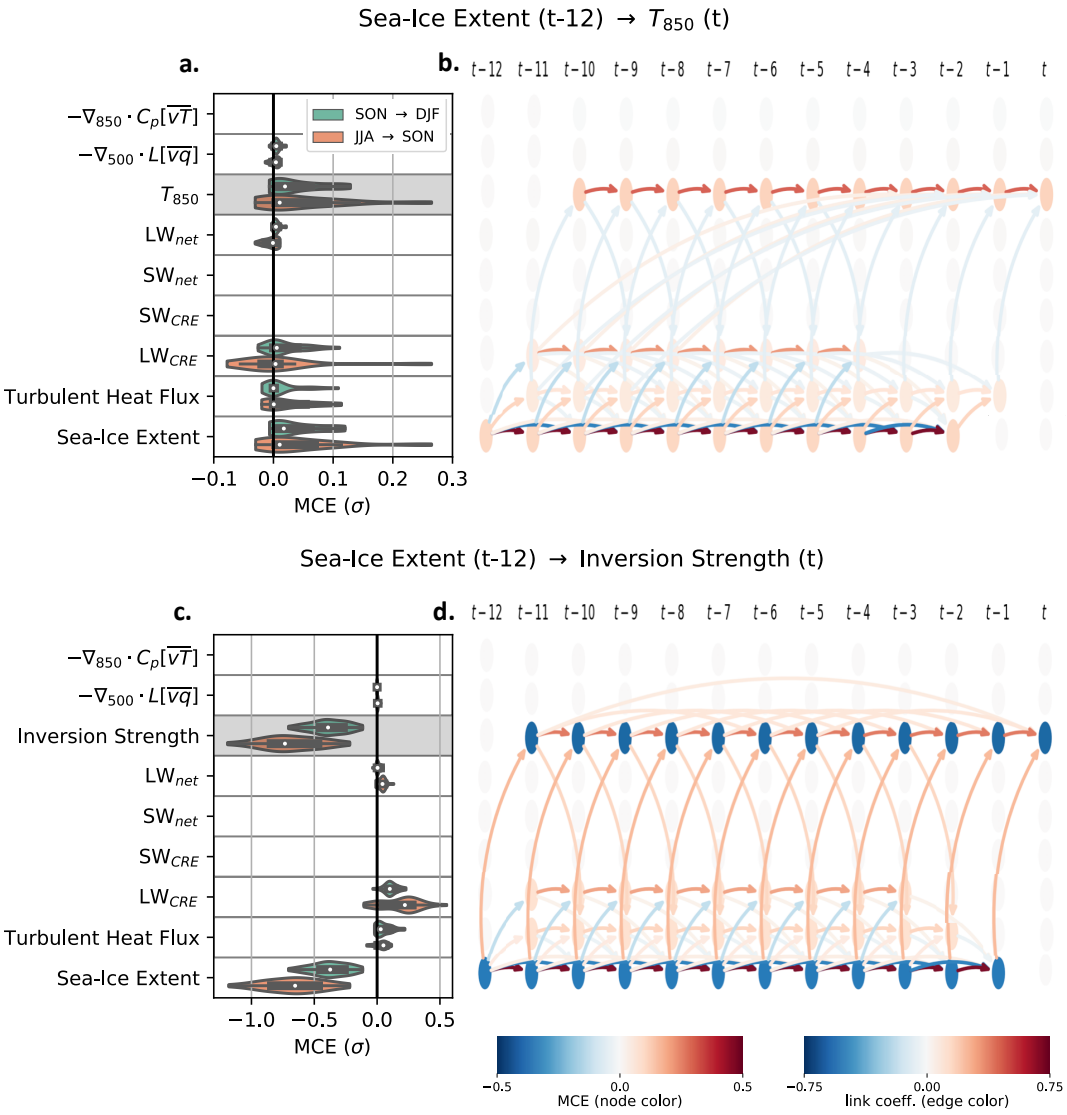

Figure 3.7: Causal pathways mediating the response of 850 hPa Arctic temperature T_{850} (a,b) and inversion strength (c,d) to an imposed -1σ step decrease in sea-ice extent at a lag of twelve weeks, shown as in Figure 3.6. Panels (a) and (c) show the distribution of mediated causal effects (MCE) separately for the summer-to-fall (JJA→SON) and fall-to-winter (SON→DJF) transitions. Panels (b) and (d) show the time series graph for CESM ensemble member 3 in the fall-to-winter transition. For simplicity, visualization in panels (b) and (d) is limited to the primary causal pathways (MCE(12) $> \pm.01$).

3.3.3 Characteristics of CO_2-forced Reduction in Boundary-Layer Stability

Our causal networks reveal that Arctic boundary-layer inversions are weakened because of their sensitivity to sea-ice perturbations in the melt season, which promote surface-amplified warming (Fig. 3.5c, Fig. 3.7c). However, the magnitude of the impact also depends on associated increases in longwave cloud radiative effect and turbulent heat fluxes, which preferentially warm 850 hPa, rather than the surface, in many CESM ensemble members (Fig. 3.7a,b). For the final component of our analysis, we contextualize this result by investigating the CO_2-forced response of the Arctic lower troposphere over the course of the CESM climate change simulation. This examination provides insight into the vertical extent of the atmospheric response to a step-decrease in sea-ice extent, as well as its relationship to the seasonal reductions in boundary-layer stability illustrated in Figure 3.1a.

First, we investigate how increases in longwave cloud radiative effect could counteract the weakening inversion due to sea-ice loss (Fig. 3.7c), while, at the same time, facilitating seasonally dependent temperature responses at 850 hPa (Fig. 3.7a). Since increases in the longwave cloud radiative effect imply enhanced downward longwave surface radiation, additional mechanisms must be considered to explain these peculiar mediating effects. Figure 3.8 shows projected changes in cloud altitude and total water content averaged over the Arctic Ocean. These variables are particularly useful for resolving the ambiguity because they are the primary contributors to positive longwave cloud feedbacks (Zelinka et al. 2012). In CESM-LE, the altitude of maximum Arctic Ocean cloud coverage shifts upward during fall and

winter (Fig. 3.8a). In the same seasons, cloud water content increases throughout the lower and mid-troposphere, with the largest increases in water content (10 g m^{-2}) occurring near 850 hPa (Fig. 3.8b). These connections are supported by reanalysis products and satellite observations in marginal sea-ice zones during Arctic fall, where a deepened atmospheric boundary layer permits upward shifts in both cloud coverage and relative humidity (Schweiger et al. 2008). Cloud changes are also reflected in the changing vertical structure of atmospheric heating rates over the 21st century, which features increased evaporative cooling near the Arctic surface and increased condensational heating near 850 hPa (Fig. 3.9a, blue curves). We find that variability in LW_{CRE} is strongly correlated with 850 hPa condensational heating over sea-ice regions, especially in fall ($r > .6$) and winter ($r > .8$, not shown). This correlation suggests that the near-surface warming impact of sea-ice driven LW_{CRE} increases is outweighed by concurrent increases in condensational heating at the cloud deck height (Fig. 3.8). Indeed, 850 hPa condensational heating experiences larger forced changes than longwave cooling rates (Fig. 3.9a, brown curves), which are likely associated with Arctic cloud emissivity (Curry et al. 1996; Turner et al. 2018). The RCP8.5 changes thus provide a physically plausible explanation for how an increase in LW_{CRE} may be associated with a reduced weakening of the inversion (Fig. 3.7c,d). We note that cloud properties and heating rates are not included in our causal networks, which prevents them from distinguishing cloud-driven longwave cooling (weakening inversion strength) from cloud-driven condensational heating (increasing inversion strength). However, the vertical profiles in Figure 3.8 and Figure 3.9 suggest condensational heating as the dominant mechanism.

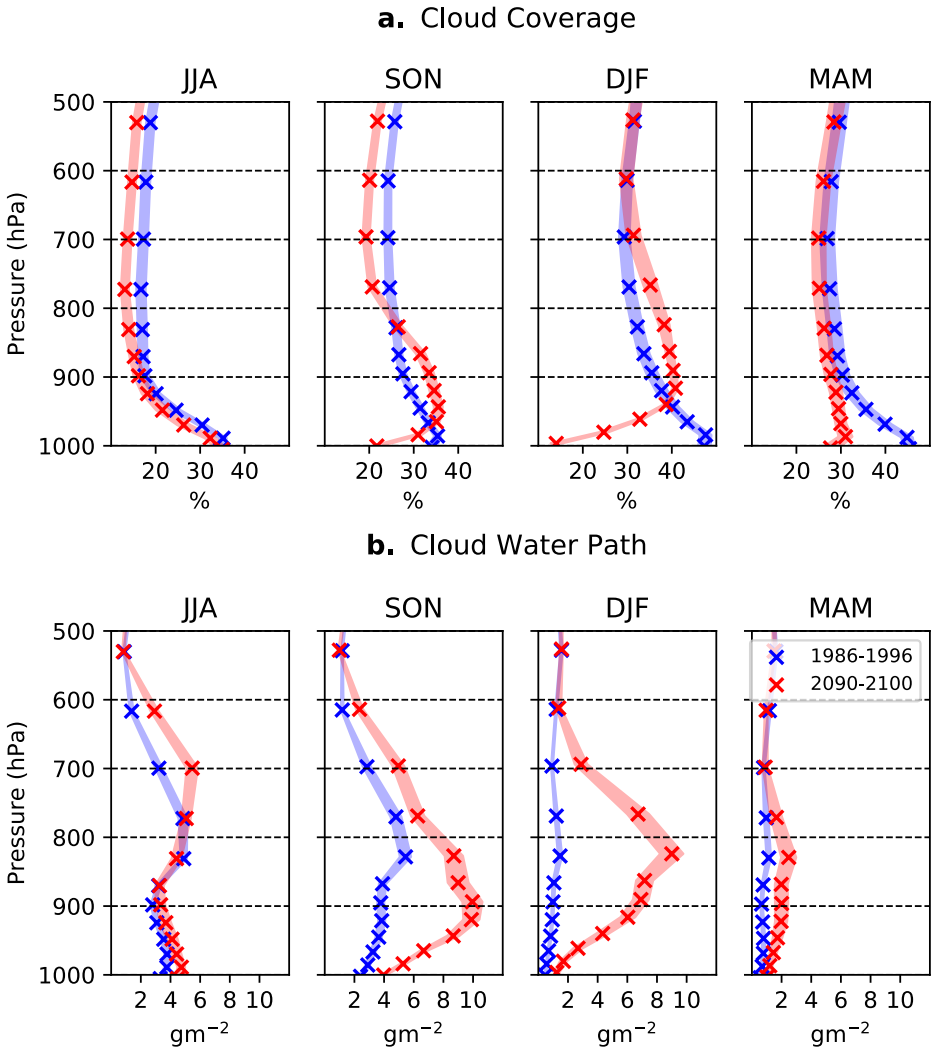

Figure 3.8: The 21st century, RCP8.5-forced change in Arctic atmospheric (a) cloud coverage ($CLOUD$) and (b) in-cloud total water path (liquid+ice, $ICLDTWP$) in the Community Earth System Model, Large Ensemble (CESM-LE). Vertical profiles show the Arctic-average 1986-1996 (blue) and 2090-2100 (red) climatologies separately for each season, displayed as in Figure 3.1. For all vertical profiles, the Arctic is defined as the spatial average within the annual mean sea-ice edge (1986-1996 15% concentration contour).

Changes in evaporation and condensation are primarily compensated by the vertical diffusion of turbulent heat fluxes (Fig. 3.9a, green curves), consistent with the mediated causal effects shown in Figure 3.7. Enhanced vertical diffusion near the Arctic surface corresponds to enhanced upward turbulent heat fluxes

(Fig. 3.2b, Fig. 3.3i,Fig. 3.7c,d), accomplishing an upward transfer of heat away from the Arctic surface. Notably, no season features changes in shortwave heating rates (Fig. 3.9a, orange curves). The constant shortwave atmospheric heating over the 21st century is consistent with the minimal cloud changes seen in summer and spring (Fig. 3.8), as well as our causal networks, which show that shortwave processes do not mediate the atmospheric temperature response to enhanced latent heat flux convergence (Fig. 3.6) or sea-ice loss (Fig. 3.7).

The sum of these four atmospheric heating rate changes is displayed in Figure 3.9b. Not surprisingly, seasons with the largest, most vertically extensive increases in net vertical heating rate are the same seasons featuring changes in boundary-layer inversion strength (Fig. 3.1a). Winter features the largest 21st century decrease in boundary-layer inversion strength and the largest increase in lower tropospheric net vertical heating rate. Similar, smaller changes are seen in spring and fall. In summer, 21st century Arctic warming is vertically uniform, and Figure 3.9b shows negligible changes in the net heating rate. This relationship implies that when climatological temperature inversions are eroded, especially in winter, near-surface warming anomalies can be mixed upward through a larger depth of the troposphere.

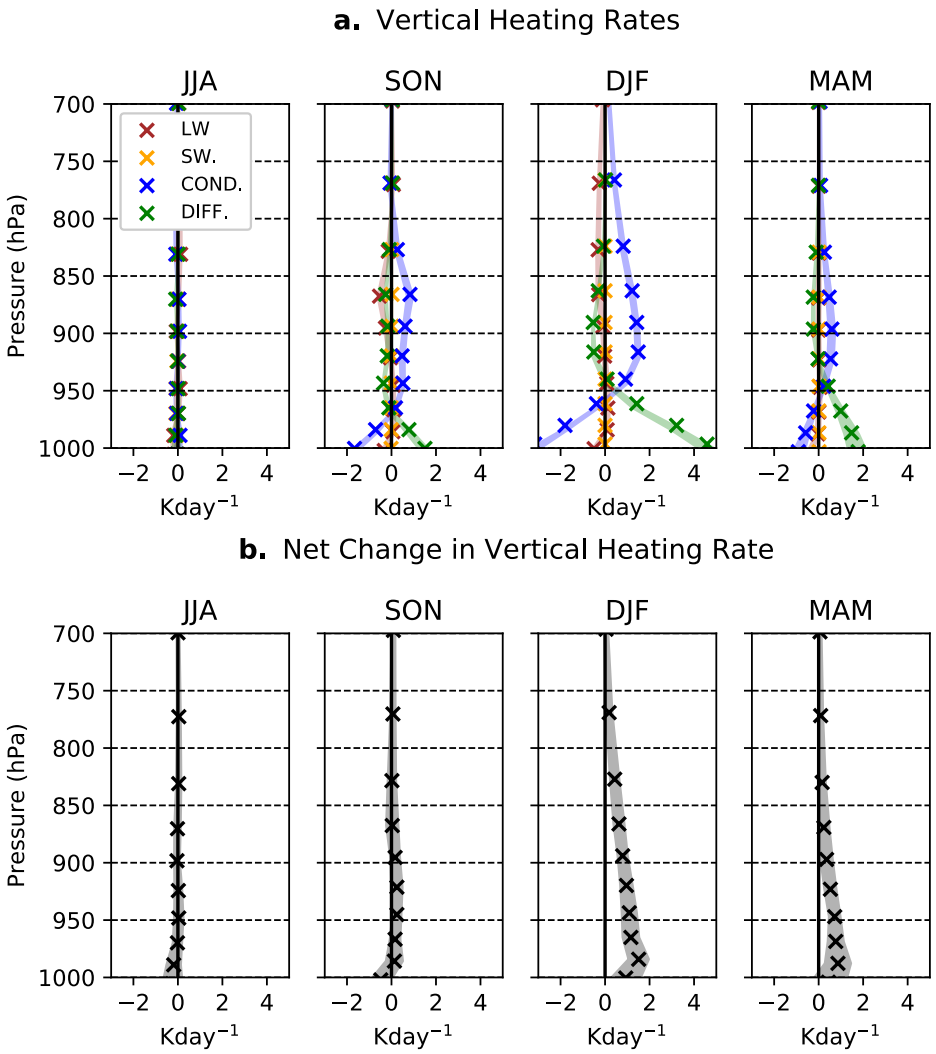

Figure 3.9: The 21st century, RCP8.5-forced change in vertical heating rates associated with longwave radiative cooling (LW, brown), shortwave radiative heating (SW, orange), condensational heating (COND, blue) and the vertical diffusion of turbulent heat fluxes (DIFF, green) in the Community Earth System Model, Large Ensemble (CESM-LE). Changes are calculated as the difference between the 2090-2100 and 1986-1996 climatologies and are shown for individual heating rates (a) and their sum (b, black). The CESM ensemble average and ensemble spread are separated for each season and displayed as in Figure 3.8.

3.4 Summary and Discussion

We use causal effect networks from a fully coupled climate change simulation to quantify the Arctic's temperature sensitivity to 1σ perturbations in sea-ice

extent and mid-tropospheric atmospheric heat flux convergence. First, we show that each warming source drives distinct changes in lower-tropospheric temperatures during fall and winter. In the weeks following a step-increase in latent heat flux convergence, the Arctic lower troposphere adjusts towards more uniform warming with small net changes in boundary layer inversion strength. By contrast, sea-ice loss in the melt season leads to surface-amplified warming in fall and winter, which weakens the climatological temperature inversion. Boundary-layer stability is maintained during spring and summer, which feature relatively less warming in response to sea-ice loss. Taken together, these causal effects imply that, of our two proposed drivers, local sea-ice loss is more important in setting the magnitude of the high-latitude lapse rate feedback. These results do not define an ultimate primary cause of Arctic-amplified warming, but rather characterize the proximate causes of T_{850} and inversion strength changes. It is ambiguous to define any variable in our causal networks as an independent control on the surface energy budget. For instance, a downward longwave radiation perturbation (associated with CO_2 forcing) could cause sea-ice loss and subsequent Arctic surface warming, but downward longwave radiation is itself tightly coupled to surface temperature (Vargas Zeppetello et al. 2019). Despite this challenge, our analyses are nonetheless able to provide a robust description of how various process interactively set the Arctic vertical warming structure.

After quantifying the total causal effect of local and remote perturbations, we examine how the net Arctic warming response is mediated by changes in the surface energy budget. On multi-week timescales, we find that midtropospheric latent heat flux convergence is able to warm the Arctic surface by reducing long-

wave surface cooling. This indirect warming pathway, characteristic of a local water vapor feedback, is comparable to the more immediate 850 hPa temperature response, leading to only small inversion changes in fall and winter (Fig. 3.10), consistent with prior observation-based research on Arctic moist intrusions (Woods et al. 2013; Woods and Caballero 2016a). The mediating impact of surface changes also demonstrates that moist transport can drive Arctic surface warming without lapse rate changes, even if the causal effect of sea-ice perturbations dominate on longer time scales. A similar role for fast atmospheric processes has been demonstrated in recent CMIP5 experiments, where transport-driven Arctic amplification emerges before sea-ice loss as a rapid response to instantaneous CO_2 quadrupling (Previdi et al. 2020). In observations and reanalyses, the fast processes are characterized by synoptic-scale atmospheric variability in Arctic moisture fluxes, which includes Rossby wave breaking and atmospheric blocking (Papritz 2020), atmospheric rivers (Baggett et al. 2016), and cyclone activity (Dufour et al. 2016).

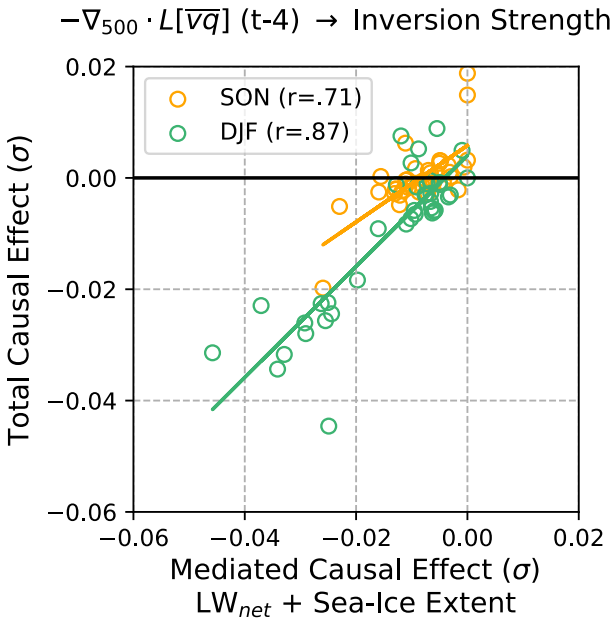

Figure 3.10: The causal effect of an imposed $+1\sigma$ step increase in 500 hPa Arctic latent heat flux convergence ($-\nabla_{500} \cdot L[\overline{vq}]$) on Arctic inversion strength at a lag of four weeks (y-axis) and the mediating impact of changes in surface conditions (net surface longwave radiative flux and sea-ice extent, x-axis). Negative causal effects indicate a weakening inversion and positive effects indicate a strengthening inversion. Values correspond to the causal effect distributions in Figure 3.6c and are shown for individual CESM ensemble members (open circles) in fall (SON) and winter (DJF). The relationship between the two quantities is illustrated with Pearson correlation coefficients (r) and linear lines of best fit for each season.

During both fall and winter, we find that the atmospheric response to sea-ice loss is facilitated by an increase in upward turbulent heat fluxes and cloud-driven condensational heating, with the vertical extent of atmospheric heating maximizing in winter; the large wintertime decreases in inversion strength are consistent with a higher cloud deck and a more extensive vertical diffusion of turbulent heat fluxes. Indeed, both observations and models have demonstrated that the cloud response to sea-ice loss is regime dependent, with lower tropospheric stability controlling the altitude of the cloud deck (Barton et al. 2012). This regime dependence is

also evident in the minimal cloud changes in summer, when high static stability is maintained throughout the 21st century. As noted in prior studies, Arctic cloud coverage and longwave optical depth can increase over newly open water if there is sufficient thermal coupling between the surface and the overlying atmosphere (Kay and Gettelman 2009; Morrison et al. 2019). As boundary-layer inversions erode under anthropogenic forcing, we expect this thermal coupling will increase.

This study only considers the physical representation of clouds in the CESM large ensemble, but cloud parameterization schemes remain bias-prone in the Arctic (Tan and Storelvmo 2019) and vary widely across models, causing substantial differences in climate sensitivity among them (Zelinka et al. 2020). Accordingly, future work is needed to diagnose similar cause-effect relationships across a range of climate models and observations. The atmospheric component of CESM1 (CAM5), for instance, is prone to lacking the cloudy state of the boundary layer in Arctic winter (Pithan et al. 2016). As a consequence, the strength of the DJF climatological temperature inversion at the start of our time series (1986-1996) is likely overestimated due to strong radiative cooling (Fig. 3.1a). Relatedly, the DJF in-cloud total water path climatology is likely underestimated (Fig. 3.8b). The newly released CESM2 has addressed some of these biases, demonstrating increased total cloud liquid, downwelling surface longwave radiation, and surface temperature (McIlhattan et al. 2020).

In conclusion, our causal networks provide evidence that the vertical structure of Arctic warming is strongly tied to sea-ice loss. At first, sea-ice loss leads to a surface-amplified warming that is characteristic of the positive high-latitude lapse rate feedback. Once warming is large enough to erode the temperature inversion,

the Arctic surface becomes more strongly coupled with the atmosphere aloft. Prior feedback studies have suggested that reduced boundary-layer inversion strength will slow the rate of Arctic warming in the future; as climatological stable stratification weakens, the high-latitude lapse rate feedback may become less positive (Bintanja et al. 2011; Bintanja et al. 2012). More recent research has argued that, because the polar atmosphere is in radiative-advective equilibrium (Cronin and Jansen 2016), lapse rate changes are dependent on the type of perturbation and may be influenced by surface-based processes (Boeke et al. 2020; Feldl et al. 2020), CO_2 and water vapor increases (Henry et al. 2021), and poleward atmospheric heat transport (Feldl et al. 2017b; Henry et al. 2021; Hahn et al. 2020). While our results indicate the predominance of local warming sources (i.e., sea ice loss), the atmosphere and cryosphere exhibit different timescales of variability. Future work will seek to integrate the causal effect of step-changes in climate drivers to predict the Arctic temperature response to transient forcings. Causal network analysis offers a flexible methodology for uncovering such relationships in any set of time series, observed or simulated, without the need for targeted modeling experiments. We encourage their continued use for understanding the future evolution of climate change in the 21st century.

Chapter 4

Atmospheric Blocking Variability Robustly Drives the Warm Arctic-Cold Eurasia Pattern in Models and Observations

Abstract

In recent decades, Arctic-amplified warming and sea-ice loss coincided with more frequent cold-air outbreaks over midlatitude continents, evidenced primarily by a prolonged wintertime Eurasian cooling trend. This observed Warm Arctic-Cold Eurasia pattern is often attributed to sea-ice forced changes in the midlatitude atmospheric circulation, implying an anthropogenic cause. However, comprehensive climate change simulations do not produce Eurasian cooling, and the observational record is too short to rule out a role for unforced atmospheric variability. This study seeks to clarify what climate conditions can produce the Warm Arctic-Cold Eurasia

pattern. We develop a statistical approach that enables like-for-like comparisons of causal relationships in both models and observations, quantifying Arctic-midlatitude interactions for a range of background climate states. Across these climate states, we find that Ural blocking drives sea ice and temperature anomalies consistent with the Warm Arctic-Cold Eurasia pattern, as well as a weakened stratospheric polar vortex. The impact of sea-ice loss on midlatitude circulation is comparatively weak and intermittent. We additionally identify distinct transient responses to Ural blocking variability, which can explain observation-model discrepancies in historical Eurasian temperature. From 1988-2012, observed Eurasian cooling occurs in response to a pronounced positive trend in Ural sea-level pressure, temporarily masking long-term midlatitude warming. In historical simulations, smaller sea-level pressure trends, both positive and negative, have little impact on the ensemble mean warming trend over Eurasia. These results highlight tropospheric variability as a key common driver of Arctic sea-ice loss and Eurasian cooling anomalies. By accounting for this variability, we are able to bring observed and simulated midlatitude temperature trends into agreement.

4.1 Main

Arctic sea-ice loss is one of the most dramatic manifestations of global climate change in the observational satellite record. Total sea-ice extent in late summer-early fall has declined by an unprecedented 25% (2 million km^2) from 1979-2019, while marginal ice zones have experienced statistically significant decreases in all seasons (Masson-Delmotte et al. 2021). This sea-ice loss can in turn exert its own

impact on Earth's atmosphere, further shaping the trajectory of climate change in the regions under its influence. Local atmospheric responses to Arctic sea-ice loss are a robust feature of both model and observations, characterized by enhanced surface absorption of solar radiation in summer (Manabe and Stouffer 1980; Duncan et al. 2020), ocean-atmosphere heat exchange in fall and winter (Dai et al. 2019; Chung et al. 2021), and attendant alterations to the polar atmosphere's vertical temperature structure (Graversen et al. 2014b; Feldl et al. 2017a; Kaufman and Feldl 2022). These cross-seasonal, sea-ice forced changes play a key role in accelerating Arctic warming relative to the global average (Pithan and Mauritsen 2014; Taylor et al. 2021). Surprisingly, recent Arctic warming and sea-ice loss have also coincided with wintertime cooling over midlatitude continents (Overland et al. 2015). This observed covariance has motivated the search for additional dynamical mechanisms that link Arctic warming and midlatitude cooling, whereby decreases in sea-ice extent drive changes in extratropical atmospheric circulation.

A range of mechanisms have been proposed to link the Arctic and midlatidues, including a weakening of the stratospheric polar vortex by vertical wave fluxes over regions of sea-ice loss (Kim et al. 2014) or the weakening of thermal wind by a reduced equator-to-pole temperature gradient (Yao et al. 2017). Additional proposed mechanisms highlight disruptions in zonal-mean zonal wind in the midlatitude troposphere by planetary-scale Rossby waves (Honda et al. 2009; Francis and Vavrus 2012; Francis and Vavrus 2015). In each case, sea-ice forced changes in atmospheric circulation are posited to facilitate cold-air outbreaks and extreme winter weather at lower latitudes. The most robust regional signature of this phenomenon involves negative sea-ice anomalies in the Barents-Kara Sea and

cold surface temperature anomalies over Eurasia, which are typically accompanied by atmospheric blocking over the Ural Mountains (Luo et al. 2016; Mori et al. 2019). Together, these metrics represent the Warm Arctic-Cold Eurasia pattern.

Proposed causal links between Arctic warming and midlatitude cooling have nonetheless been regarded with frequent skepticism in the scientific literature, with studies-to-date divided on the existence and strength of a forced response to sea-ice loss (Barnes and Screen 2015; Cohen et al. 2020; Outten et al. 2022). In particular, fully coupled climate change simulations neither reproduce the observed midlatitude cooling trends during the historical period nor simulate cooling in future projections, despite continuous Arctic warming (Sun et al. 2016; Boland et al. 2017). This model-observation discrepancy suggests a possible misinterpretation of causality in the observed statistical connections (Blackport and Screen 2021). For instance, atmospheric circulation features may drive both midlatitude temperature and sea-ice anomalies through internal variability alone, without anthropogenic forcing from the Arctic. Beyond fully coupled simulations, this alternative chain of causality has been demonstrated in both model experiments and empirical studies, which attribute the Warm Arctic-Cold Eurasia pattern to atmospheric drivers (Gong and Luo 2017; Luo et al. 2017; Peings 2019; Liu et al. 2022). A role for internal variability is also supported by the most recent years of the observational record; significant Eurasian cooling trends have largely ceased after the winter of 2012, while Arctic warming has continued unabated (Blackport and Screen 2020). These separate strands of evidence have furthered the idea that observed Eurasian cooling was a short-term fluctuation that briefly masked a long-term midlatitude warming trend.

Against this backdrop of conflicting studies, quantifying the true impact of sea-ice loss on midlatitude winter climate (or lack thereof) has proven difficult. Results from targeted perturbation experiments can demonstrate a midlatitude response to sea-ice loss, yet they are highly dependent on study design, such as the location of prescribed sea-ice loss (i.e, pan-Arctic vs. regional, Nishii et al. 2011; Screen 2017), inclusion of a dynamic ocean (Deser et al. 2016), or the vertical resolution of the climate model being used, which may impact stratosphere-troposphere coupling (Sun et al. 2015). Another challenge facing climate models involves separating the forced response to Arctic climate change from internal variability, which can require simulating many ensemble members with high computational costs (Liang et al. 2020; Peings et al. 2021). Meanwhile, observational studies are constrained by the relatively short length of the reliable satellite record, and empirical evaluations of these observations often lack robust attributions of causality that could be compared with climate model experiments.

This study seeks to quantify the relative importance of anthropogenic sea-ice loss and unforced atmospheric variability in producing wintertime Eurasian cooling. We conduct a like-for-like comparison of causal effects in observations and model output, accounting for the fact that sea-ice variability can both drive and respond to changes in midlatitude circulation. This comparison is advanced by combining a statistical causal inference method with linear convolution theory, which isolates the transient climate response to the time history of midlatitude circulation. Our flexible approach resolves several key challenges that have to this point obscured scientific understanding of the Arctic-midlatitude connections. First, we infer the direction and magnitude of causal effects without relying on targeted perturbation

experiments, enabling direct model-observation comparison. Second, we utilize the efficiency of our method to infer causal effects in a fully coupled large ensemble, separating forced responses from internal variability. Finally, we calculate the transient response to the time history of causal drivers, and in doing so we reveal the dependence of Arctic-midlatitude connections on different mean climate states.

4.2 Divergent Midlatitude Trends

We quantify Arctic-midlatitude linkages in observations provided by the NASA Global Modeling and Assimilation Office's latest reanalysis product: the Modern-Era Retrospective Analysis for Research and Applications, version 2 (MERRA-2, Gelaro et al. 2017). These linkages are compared with fully coupled model output from the CESM2 Large Ensemble Project (CESM2-LE, Rodgers et al. 2021), which simulates historical climate change in one hundred ensemble members. By applying our investigation across ensemble members, we can analyze forced climate responses (the ensemble mean), internal variability (the ensemble spread), and the degree to which observed historical trends lie within the bounds of simulated internal variability.

Our analysis focuses on the 1988-2012 time period, when observations exhibit the strongest trends associated with the Warm Arctic-Cold Eurasia pattern. Regional trends for relevant metrics are shown in Fig. 4.1 for boreal winter (DJF), highlighting key similarities and differences between MERRA-2 and CESM2-LE. Observed and modeled trends both exhibit Arctic sea-ice loss in marginal ice zones (Fig. 4.1a,b) and Arctic-amplified warming below 850 hPa (red contours, Fig. 4.1e,f),

consistent with the bottom-heavy warming profiles associated with sea-ice loss. In the Barents-Kara Sea region (black polygon, Fig. 4.1a,b) observed trends in near-surface air temperature (1.1 °C per decade) are well within the ensemble spread of CESM2-LE, where the mean trend and standard deviation are 1.0±0.84 °C per decade. The Barents-Kara Sea also experiences the largest regional sea-ice loss in both observations and models, featuring an observed sea-ice trend of -1.5 $\times$ 10^5 km^2 and smaller simulated trends of 0.74 ±0.59 $\times$ 10^5 km^2 per decade.

By contrast, large model-observation discrepancies are evident in near-surface air temperature and sea-level pressure trends in the midlatitudes (Fig. 4.1c,d). In observations, the Ural mountain region (dashed black polygon, Fig. 4.1c,d) features a prominent positive sea-level pressure trend of 5.0 hPa per decade (green contours, Fig. 4.1c), whereas CESM2-LE features a range of positive and negative sea-level pressure trends, with negligible changes in the ensemble mean (-0.27±1.4 hPa per decade, Fig. 4.1d). Over central Eurasia (solid black polygon, Fig. 4.1c,d), observations feature a significant cooling trend of -1.3 °C per decade (Fig. 4.1c), while CESM2-LE showcases near-surface warming throughout the Northern Hemisphere (Fig. 4.1d). Additional notable differences can be found in the lower stratosphere (Fig. 4.1e,f); observations indicate a secondary polar warming peak aloft and a corresponding weakening of the stratospheric polar vortex, where polar-cap averaged $[u_{10}]$ decreases by -4.7 ms^{-1} per decade (Fig. 4.1e). Neither of these features are apparent in the CESM2-LE ensemble mean (Fig. 4.1f), where trends associated with the Warm Arctic-Cold Eurasia pattern are largely absent.

We proceed by examining the time-lagged relationships between five spatially aggregated climate indices associated with the Warm Arctic-Cold Eurasia pat-

tern: Barents-Kara sea-ice extent (65°-85°N,10°-90°E), Eurasia near-surface (2m) air temperature (40°-60°N, 60°-120°E), Ural sea-level pressure (55°-70°N,40°-90°E), stratospheric polar vortex strength ($[u_{10}]$, 60°-80°N), and the phase of the North Atlantic Oscillation (NAO)[1]. While neither observations nor model output show clear trends in the phase of the NAO, which would manifest as a sea-level pressure dipole associated with Icelandic Low and the Azores High (green contours, Fig. 4.1c,d), we account for its influence given the NAO is a prominent large-scale mode of climate variability in our region of interest.

[1]The NAO time series is calculated by projecting sea-level pressure anomalies in each gridcell onto the the first empirical orthogonal function mode of December–March sea-level pressure for the 65°-85°N,85°W-60°E domain (Peings 2019). Our remaining indices follow the regional definitions used in Blackport and Screen (2021), shown with the black polygons in Fig. 4.1.

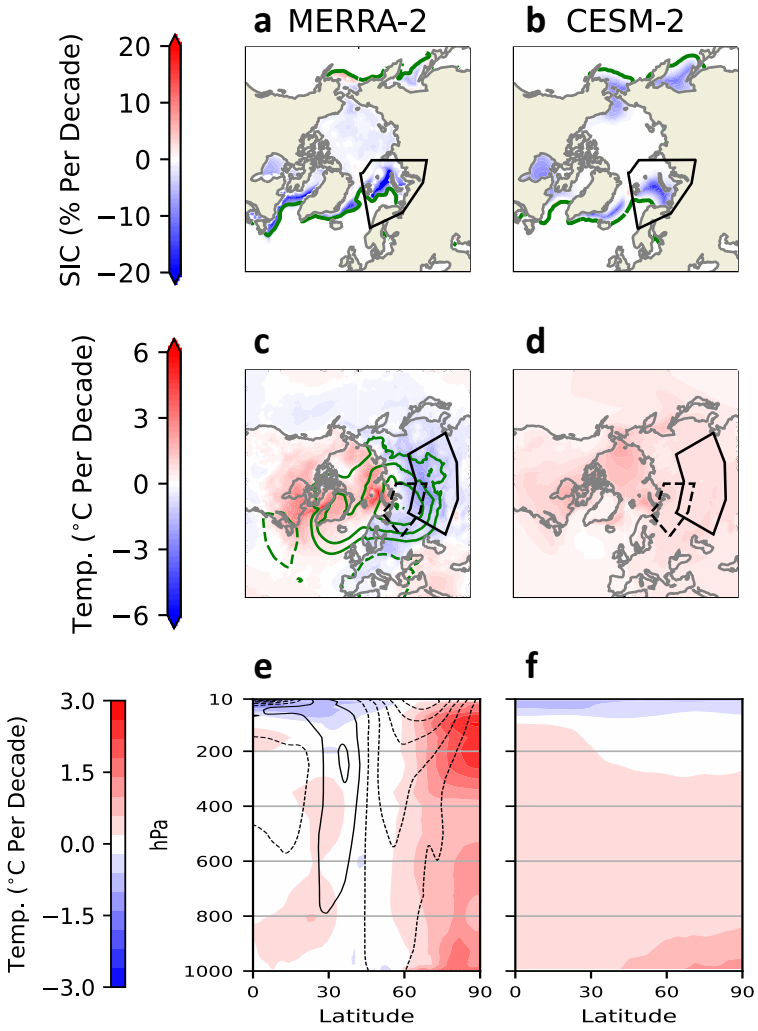

Figure 4.1: **Trends in 1988-2012 winter (DJF) climate in MERRA-2 observations and the ensemble-mean of one hundred CESM2-LE historical simulations**. **a-b**, Trends in Arctic sea-ice extent (red and blue contours, % per decade) and the climatological DJF sea-ice extent over the entire time period (5% concentration contour, green). **c-d**, Trends in near-surface air temperature (red and blue contours, °C per decade) and sea-level pressure (green contours, hPa per decade), displayed in intervals of 1.5 hPa from -6 to 6 (zero omitted). **e-f**, Vertical profiles of zonal mean trends in temperature (red and blue contours, °C per decade) and zonal wind (black contours, ms^{-1} per decade), displayed in intervals of 1 ms^{-1} from -7.5 to 7.5. The dashed black polygon indicates the Ural blocking region (**c-d**); the solid black polygons indicate the Barents-Kara Sea region (**a-b**) and central Eurasia region (**c-d**).

4.3 A Robust Causal Driver of the Warm Arctic-Cold Eurasia Pattern

For MERRA-2 observations and each CESM2-LE ensemble member, we construct causal networks from the five aforementioned 1988-2012 time series (Fig. 4.2), which highlight the drivers of the Warm Arctic-Cold Eurasia pattern. To address signal intermittency in the short observational record, we employ a bootstrapping procedure (Siew et al. 2020) that generates one hundred observation-based time series samples to accompany the one hundred CESM2 ensemble members. Causality is inferred using the PCMCI algorithm (Runge et al. 2017), which calculates time-lagged partial correlations in a series of iterative conditional independence tests (see Methods). The causal links identified by this algorithm are given by the lagged, linear correlations that remain significant after controlling for indirect mediators, common drivers, and auto-correlation (memory). We evaluate relationships amongst detrended anomalies at quarter-monthly (i.e., weekly) lags of one to twelve weeks, accommodating both the shorter timescale of atmospheric variability and the longer timescale of sea-ice variability. Lastly, we restrict correlation calculations to the months of September-March, encompassing the seasons of maximum Arctic sea-ice loss (early fall) and the active Warm Arctic-Cold Eurasia Pattern (winter).

The causal networks identify two significant causal relationships as remarkably robust in both models and observations, appearing in 99-100% of MERRA-2 bootstrap samples (Fig. 4.2a) and CESM2-LE ensemble members (Fig. 4.2b). Both links are associated with anomalies in Ural sea-level pressure (Node 2.), which predict opposite-signed anomalies in both Barents-Kara sea-ice extent (2. $\rightarrow$ 1.) and

central Eurasia T_{2m} (2. $\rightarrow$ 3.). The causal links are strongest at a lag of one week, where the average partial correlation coefficient ($\overline{r}$, link color) between Ural sea-level pressure and Barents-Kara sea-ice is -0.35 in both MERRA-2 and CESM2-LE. The lag-1 partial correlations are similar between Ural sea-level pressure and central Eurasia T_{2m}, with an $\overline{r}$ of -0.33 and -0.32 for MERRA-2 and CESM2-LE, respectively. Interpreted physically, these two robust links indicate that Ural blocking events (positive sea-level pressure anomaly) can drive both sea-ice loss (Warm Arctic, 2. $\rightarrow$ 1.) and midlatitude cooling (Cold Eurasia, 2. $\rightarrow$ 3.) on weekly timescales.

Interestingly, atmospheric responses to Barents-Kara sea-ice anomalies (Node 1., Fig. 4.2) are comparatively weak and intermittent. In MERRA-2, Ural blocking anomalies are caused by Barents-Kara sea-ice loss (1. $\rightarrow$ 2.) at lags of seven to ten weeks ($\overline{r}$ = -0.21 at lag-10), but this relationship is only detected in 37% of MERRA-2 bootstrap samples. Barents-Kara sea-ice loss also predicts a negative NAO phase in MERRA-2 (1. $\rightarrow$ 4.), but this signal is similarly intermittent, being featured in 42% of MERRA-2 bootstrap samples. Neither causal link is present in CESM2-LE. Connections between Arctic sea-ice loss and the stratospheric polar vortex (Node 5., Fig. 4.2) are even more tenuous. In 71% of MERRA-2 bootstrap samples and 44% of CESM2-LE ensemble members, a weakened polar vortex state is caused by positive anomalies in Ural sea-level pressure (2. $\rightarrow$ 5.), with additional contributions from a negative NAO phase in observations (4. $\rightarrow$ 5., Fig. 4.2a). These stratosphere-troposphere connections are consistent with an anomalously meridional flow pattern. However, direct causal links between the polar vortex and Barents-Kara sea-ice extent are nearly non-existent. These weak atmospheric responses are

robust to our choice of timestepping interval, season selection, and averaging region used to define the Barents-Kara Sea.

Our causal network analysis can thus be summarized as follows. Positive Ural sea-level pressure anomalies (Ural blocking) are a robust atmospheric driver of the Warm Arctic-Cold Eurasia pattern in both observations (Fig. 4.2a) and models (Fig. 4.2b). In MERRA-2 observations, a smaller subset of time samples feature a two-way interaction, whereby Ural blocking events both drive and respond to negative Barents-Kara sea-ice anomalies (Fig. 4.2a). In these cases, Ural blocking could, in theory, also mediate a Eurasian cooling response to anthropogenic sea-ice loss. However, the generally weak signal-to-noise ratio of this causal pathway (and many others) suggests that Ural blocking variability is largely internally driven, or responding to a remote, non-Arctic forcing that is beyond the focus of our analysis. Accordingly, this unforced Ural blocking variability may be able to explain the model-observation discrepancy in historical Eurasian cooling (Fig. 4.1c,d).

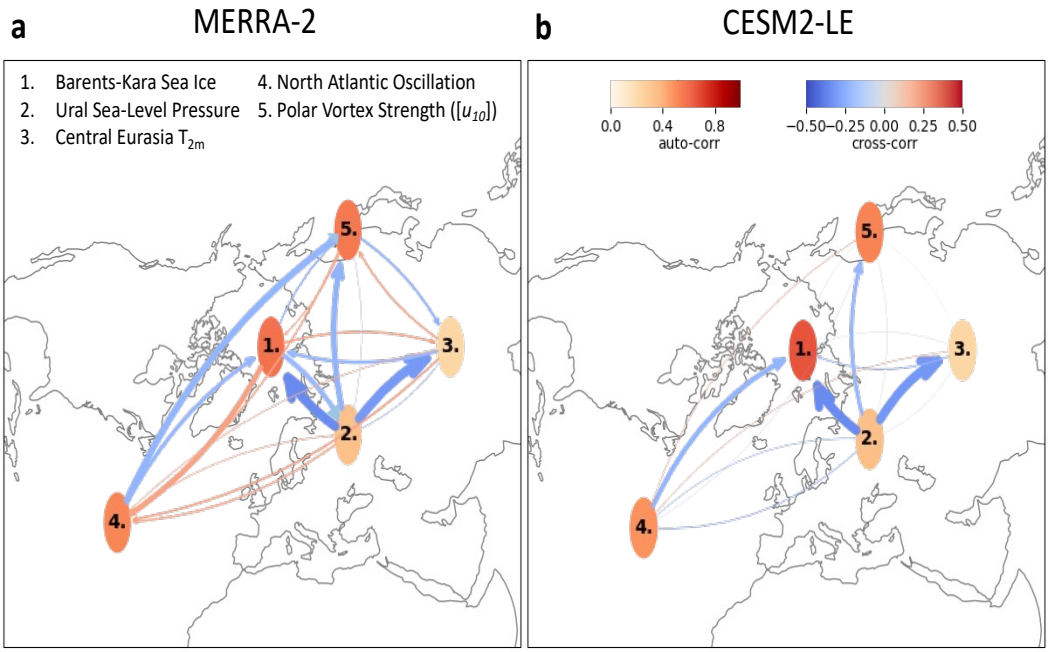

Figure 4.2: **Time-lagged causal links between Barents-Kara Sea ice, Ural sea-level pressure, Central Eurasia 2m air temperature, NAO Phase, and polar vortex strength ($[\mathbf{u_{10}}]$) in MERRA-2 observations and one hundred CESM2-LE historical simulations**. Potential causal relationships are evaluated by the PCMCI algorithm over lags of one to twelve weeks for the 1988-2012 period in the months of September-March. Arrows denote the direction and strength of causal links deemed significant at the α=.01 level. Arrow thickness indicates the frequency of link detection among the one hundred bootstrap samples from MERRA-2 (**a**) and one hundred CESM2-LE ensemble members (**b**), with the thickest arrows appearing in 99-100% of samples. Arrow color indicates the average partial correlation coefficient at the time lag with the largest signal; specific lags associated with each link are described in Section 4.3. Node color indicates the magnitude of autocorrelation (memory) associated with each variable.

4.4 The Transient Response to Ural Blocking

We next assess how historical trends in Barents-Kara sea ice and Eurasian temperature depend on the time history of Ural blocking. This component of our analysis advances the use of linear convolution theory, whereby the transient response of variable Y to forcing, F, can be estimated as the convolution of a Green's

Function (G) with the time history of the forcing, assuming the response is linear:

$$\hat{Y}(t) \approx \sum_{\tau=1}^{\tau_{\max}} G(\tau)F(t-\tau)\Delta\tau. \tag{4.1}$$

Green's Function $G(\tau)$ is the step-response of Y to a one standard deviation perturbation in forcing F (Ural sea-level pressure, in our case) at time lag τ (weeks), and $\hat{Y}(t)$ is the transient response to the time history of Ural sea-level pressure: $F(t-\tau)$. When derived from isolated model perturbation experiments or lagged linear regressions, $G(\tau)$ has been described as a climate response function, (Marshall et al. 2014; Kostov et al. 2018; Rye et al. 2020). Here, we derive $G(\tau)$ from our causal inference framework, where it represents the total causal effect of of a hypothetical $+1\sigma$ anomaly in Ural sea-level pressure. Specifically, we fit a sparse vector autoregressive model to the five time series analyzed in Section 4.3, then iteratively multiply the regression matrix products from $\tau = 1$ to $\tau_{max} = 12$ weeks (see Methods).

The $G(\tau)$ step responses to Ural sea-level pressure are shown in Fig. 4.3 for Eurasian 2m air temperature (Fig. 4.3a) and Barents-Kara sea ice (Fig. 4.3b). The Eurasian cooling response to a Ural blocking anomaly peaks at $\tau = 1$ week, with values of -3.1 °C for MERRA-2 and -2.3 °C for the CESM2-LE ensemble mean, before gradually decaying to zero by $\tau = 7$. Barents-Kara sea ice also decreases in response to Ural blocking, with a $\tau = 2$ peak of -0.28 $\times$ 10^5 km^2 in MERRA-2 and a $\tau = 1$ peak of -0.24 $\times$ 10^5 km^2 for the CESM2-LE ensemble mean. In both datasets, the sea-ice step responses persist over a longer time period than the temperature responses, which is consistent with the longer decorrelation length scale associated with sea-ice anomalies (node color, Fig. 4.2). The MERRA-2 responses to a step

increase in Ural sea-level pressure are larger than the CESM2-LE ensemble mean, but still well within the ensemble spread, indicating a qualitative similarity (compare black and blue curves, Fig. 4.3a,b).

Despite the similar step responses, observed and simulated Ural sea-level pressure time histories (Fig. 4.3c) exhibit large differences. Over the entire historical period (1920-2012), there is a 48% chance of observing a positive 25-year trend in wintertime Ural sea-level pressure in CESM2-LE (blue histogram, Fig. 4.3c), but only a 0.14% chance of observing a positive trend as large as the 5.0 hPa per decade trend seen in 1988-2012 observations (vertical dashed line, Fig. 4.3c). In other words, even if models and observations have a similar sensitivity to Ural blocking, their transient response to the Ural blocking time histories can be quite different. This difference becomes particularly apparent when the Green's functions (Fig. 4.3a,b) are convolved with the Ural blocking time histories (Fig. 4.3c).

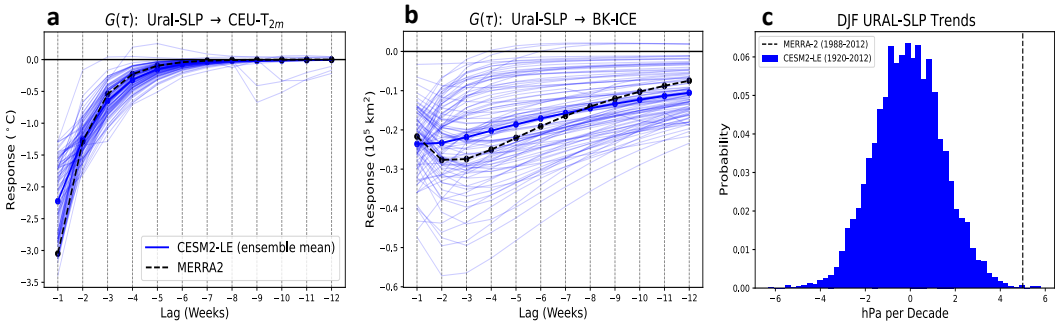

Figure 4.3: **Green's functions and time histories associated with Ural blocking**. **a-b** $G(\tau)$, the estimated response of Central Eurasia T_{2m} and Barents-Kara sea ice to a hypothetical $+1\sigma$ step increase in Ural sea-level pressure at lags of one to twelve weeks. Response functions are shown with thin blue lines for one hundred individual CESM2-LE ensemble members, thick blue lines for the CESM2-LE ensemble mean, and dashed black lines for MERRA-2 observations. **c** Probability distribution of 25-year trends in winter (DJF) Ural sea-level pressure (hPa per decade) over the entire historical period in CESM2-LE (1920-2012, blue histogram). The 1988-2012 Ural sea-level pressure trend from MERRA-2 observations is shown with a dashed vertical line for comparison.

The linear convolutions (Eqn. 4.1) yield the transient response of Eurasian temperature and Barents-Kara sea ice to the time history of Ural blocking (Fig. 4.4). As previously noted, the observed winter trend in Central Eurasia temperature is cooling (-1.3 °C per decade, black curve, Fig. 4.4a), and the ensemble mean simulated trend is warming (0.80 °C per decade, blue curves, Fig. 4.4a). Notably, these divergent midlatitude trends can be reconciled by distinct transient temperature responses to Ural blocking. In observations, Eurasia cools strongly, by -1.9 °C per decade, in response to Ural blocking (black curve, Fig. 4.4b). By contrast, the wide range of Ural sea-level pressure trends in CESM2-LE (Fig. 4.3c) produce both negative and positive temperature responses (thin blue curves, Fig. 4.4b), with a weak positive response in the ensemble mean (0.27 °C per decade, thick blue curve, Fig. 4.4b). Once the transient effects of Ural blocking are removed, both observed and simulated Eurasian temperature trends feature a remarkably similar warming signal: 0.89 and 0.67 °C per decade in MERRA-2 and the CESM2-LE ensemble mean, respectively (Fig. 4.4c). We interpret these warming signals as the trend due to anthropogenic forcing, which, for observations, was masked by Ural sea-level pressure variability in Fig. 4.4a.

Unlike Eurasian temperature, models and observations agree that 1988-2012 winter sea-ice retreat occurred in the Barents-Kara sea, as previously shown in Fig. 4.1a,b. However, the observed December-March trend in sea-ice extent (-1.4 $\times$ 10^5 km^2 per decade, black curve, Fig. 4.4d) is larger than in the CESM2-LE ensemble mean (-0.67 $\times$ 10^5 km^2 per decade, blue curves, Fig. 4.4d). Here too, accounting for the transient response to Ural blocking helps to brings models and observations into agreement. MERRA-2 features the largest transient response to

Ural blocking (-0.74 $\times$ 10^5 km^2 per decade, Fig. 4.4e), which explains 50% of the observed 1988-2012 winter trend. CESM2-LE has a negligible transient response to Ural blocking in the ensemble mean. When the effect of Ural blocking is removed, observed and simulated trends in sea-ice loss are similar (-0.65 and 0.72 $\times$ 10^5 km^2 per decade; Fig. 4.4f). This similarity implies that the larger sea-ice loss trend in observations (Fig. 4.4d) can be attributed to Ural blocking variability (Fig. 4.4e). In other words, the large positive Ural sea-level pressure trend in MERRA-2 (Fig. 4.3c) amplified observed 1988-2012 Barents-Kara sea-ice loss.

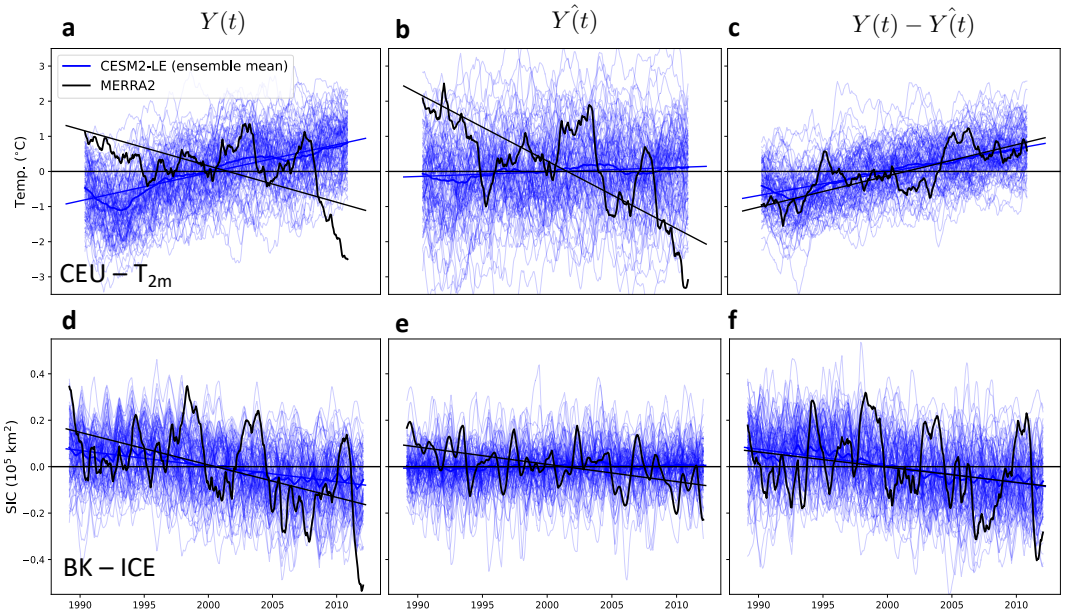

Figure 4.4: **Transient temperature and sea-ice responses to Ural blocking variability. a-c** 1988-2012 time series of Central Eurasia T_{2m} in CESM2-LE (blue) and MERRA-2 observations (black), shown as weekly December-March anomalies relative to the 1988-2012 climatology. The left column ($Y(t)$, **a**) shows observed and simulated trends, while the middle column ($\hat{Y(t)}$, **b**) shows the transient response to the time history of Ural sea-level pressure. The right column shows the difference ($Y(t)$ - $\hat{Y(t)}$, **c**), indicating the temperature trends with the effects of Ural blocking variability removed. **d-f** The same as **a-c**, but for 1988-2012 time series of Barents-Kara Sea Ice. For ease of visualization, a 12-month rolling mean is applied to the weekly temperature anomalies (**a-c**) and a 2-month rolling mean is applied to the weekly sea-ice anomalies (**d-f**).

4.5 Summary and Discussion

We use a causal inference algorithm to identify a common atmospheric driver of the Warm Arctic-Cold Eurasia Pattern: Both Barents-Kara sea-ice loss and Central Eurasian cooling are caused by positive anomalies in Ural sea-level pressure on weekly timescales. While sea-ice loss itself may also effect Ural sea-level pressure (a two-way interaction), the signal associated with this causal pathway is intermittent and weak compared to background variability. Second, we show that the observed positive trend in Ural sea-level pressure was abnormally large between the winters of 1988 and 2012. The transient response to this Ural blocking trend produced a midlatitude cooling tendency that temporarily masked the long-term warming trend, whilst simultaneously amplifying the rate of anthropogenic sea-ice loss. The time history of Ural blocking produces smaller responses in a set of fully coupled large ensemble simulations, which are unable to outweigh anthropogenic trends. These results highlight the importance of atmospheric variability for assessing the likelihood of opposing temperature trends in the Arctic and midlatitudes.

Our analysis builds upon the prior causal inference studies of Kretschmer et al. (2020) and Siew et al. (2020), which highlight intermittent, two-way interactions between Barents-Kara sea-ice extent and midlatitude circulation. In spite of this intermittency, we identify an atmospheric driver of the Warm Arctic-Cold Eurasia pattern that is robust across climate states in both models and observations. This key role of Ural blocking is consistent with the mechanisms identified in a variety of targeted model experiments. For instance, Peings (2019) imposed Ural blocking anomalies in an otherwise stable climate, producing temperature anomalies

consistent with the Warm Arctic-Cold Eurasia pattern, as well as a weakened stratospheric polar vortex. This circulation pattern shapes the midlatitude storm track in a manner that favors moist intrusions into the Barents-Kara sea, where anomalous poleward eddy fluxes lead to sea-ice melt in winter (Woods and Caballero 2016b; Luo et al. 2017). Meanwhile, Ural blocking simultaneously promotes cold-air outbreaks along its eastern flank, leading to cooling over Eurasia. Our causal networks show that Ural blocking impacts also extend to the upper atmosphere, weakening stratospheric winds, with minimal contributions from sea-ice loss. Unlike the bottom heavy signal of sea-ice loss, moist energy transport from lower latitudes, including intrusions promoted by Ural blocking, tend to cause more vertically extensive Arctic warming (Feldl et al. 2020; Kaufman and Feldl 2022). The Arctic temperature response to poleward energy flux anomalies can extend to the stratosphere, leading to sudden stratospheric warming events and a weakening of the polar vortex (Cardinale et al. 2021). Consistent with this dynamical pathway, Eurasian cooling does occur in model experiments with deep tropospheric warming in the Arctic, which cannot be produced through sea-ice loss alone (He et al. 2020; Labe et al. 2020).

Lastly, our results suggest that prolonged Eurasian cooling will become less likely in a warming world. The cold-air outbreaks that produce such cooling primarily depend on atmospheric circulation variability associated with Ural blocking. As both the Arctic and midlatitude continue to warm, the likelihood that such variability will be able to mask these warming trends will decrease. Additionally, Barents-Kara sea-ice loss plays only a small role in shaping this atmospheric variability. Even if the abnormally pronounced circulation trends in 1988-2012 were in part due to sea-ice loss, sea-ice impacts are likely non-linear and state-dependent.

Once the Barents-Kara sea becomes seasonally ice free, its influence on midlatitude circulation is expected to decrease (e.g., Kretschmer et al. 2020). Our analysis focuses on the historical period, where we identify atmospheric blocking variability as the dominant driver of the 1988-2012 Eurasian cooling trend. We therefore conclude that the Warm Arctic-Cold Eurasia pattern is an ephemeral phenomenon, unlikely to occur again in the future.

4.6 Methods:

4.6.1 PCMCI algorithm:

The PCMCI algorithm (Runge et al. 2017) is applied in Section 4.3 to identify robust causal relationships underlying the Warm Arctic-Cold Eurasia Pattern. One hundred distinct causal networks are constructed for each CESM2-LE ensemble member (historical simulations) and each MERRA-2 bootstrap sample (observations), using five input time series spanning 1988-2012. The MERRA-2 bootstrap samples consist of twenty-four randomly selected years from the reanalysis period (with replacement). Before input to PCMCI, all time series variables normalized by subtracting linear trends and dividing by the standard deviation for each component of the seasonal cycle. PCMCI is characterized by a two-step causal discovery procedure: the PC-stable causality test (named after its creators, Peter Spirtes and Clark Glymour; Spirtes et al. 2000), followed by the Momentary Conditional Independence (MCI) test (Runge et al. 2017). In the following description, Equations 4.2 and 4.3 are associated with step one (PC-stable), and Equation 4.4 is associated with step two (MCI).

PC-stable identifies a set of potential causal drivers for each variable, x, in the causal network using a series of iterative correlation calculations. In iteration one, every possible time-lagged linear auto-correlation and cross-correlation, from τ=1 to $\tau = \tau_{\max}$, is calculated as:

$$\rho(X_i(t-\tau), X_j(t)) \tag{4.2}$$

where ρ is the Pearson correlation coefficient, τ is a time lag (weeks), and $X_i(t-\tau)$ are lagged time series with a potential causal influence on $X_j(t)$. Contemporaneous links are not considered. If the value of ρ is found to be insignificant, $X_i(t-\tau)$ is eliminated from the set of potential causal drivers of $X_j(t)$.

In iteration two, the correlations are re-calculated for the remaining potential drivers as:

$$\rho(X_i(t-\tau), X_j(t)|Z_1) \tag{4.3}$$

where $Z_1 \neq X_i(t-\tau)$ is the auto or cross-link possessing the strongest unconditional correlation with $X_j(t)$ in Equation 4.2. The vertical line in Equation 4.3 denotes removing the linear influence of Z_1 from both $X_i(t-\tau)$ and $X_j(t)$ and testing the correlation between their residuals. If Z_1 makes the formerly significant link insignificant, the two variables are said to be conditionally independent, and the link is subsequently removed. This process is repeated over n iterations by adding an increasingly stringent number of conditions, Z_2, Z_3, ..., Z_n to the partial correlation tests until no more links can be removed. The PC-algorithm finishes when it converges to a final set of significant links for each variable, which are defined as the "parents" of each variable: $\mathbf{P}(X_j(t))$.

Standalone implementations of PC-stable in previous climate studies have treated the level of statistical significance, α, as a user-selected free parameter, typically with values of .01 or .05 (Kretschmer et al. 2016; Samarasinghe et al. 2018; Kaufman and Feldl 2022). In the context of PCMCI, used here, PC-stable is conducted for a range of less strict significance levels, where hyperparameter α = [0.1,0.2,0.3,0.4]. The ultimate choice of significance level is then optimized objectively by fitting a regression model to the parents associated with each value of α, which are compared using the Akaikie Information Criterion (AIC). The choice of α associated with the minimum AIC value defines the parents of each variable, $\mathbf{P}(X_j(t))$.

In the second step of the PCMCI algorithm, the MCI test, the full set of lagged auto-correlations and cross-correlations is calculated a final time, conditioned on each variable pairs' parents identified in step one:

$$\rho(X_i(t-\tau), X_j(t)|\hat{\mathbf{P}}(X_j(t)), \mathbf{P}(X_i(t-\tau))) \tag{4.4}$$

where $\hat{\mathbf{P}}(X_j(t))$ are the parents of , $X_j(t)$, excluding $X_i(t-\tau)$, and $\mathbf{P}(X_i(t-\tau)))$ are the parents of $X_i(t-\tau)$. In the MCI test, α returns to being user-defined, with α=.01 in our study. Lastly, the statistical significance of each correlation is adjusted using the Hochberg–Benjamini false discovery rate (FDR) control (Benjamini and Hochberg 1995). The final set of significant links identified Equation 4.4 are considered the causes of $X_j(t)$, shown for our system of interest in Fig. 4.2. This designation is based on the causal Markov condition, which states that X_j is independent of all network variables, except X_j's effects, when conditioned on the causes of X_j (Spirtes et al. 2000). Ultimately, the PCMCI algorithm improves

the stability of inferred causal relationships relative to standalone implementations of PC-stable. Additionally, PCMCI is particularly effective at accounting for strong auto-correlation effects, such as those associated with sea-ice variability on weekly timescales. The Tigramite coding and graphics package for PCMCI (`https://jakobrunge.github.io/tigramite/`) is used to produce the data discussed in Section 4.3 and the causal network visualizations in Fig. 4.2.

4.6.2 Climate Response Functions

A climate response function can be regarded as a quasi-Green's function, $G(\tau)$, which we use to describe the hypothetical response of temperature and sea ice to a $+1\sigma$ step increase in Ural sea-level pressure at time lag τ (Section 4.4, Fig. 4.3a,b). In this study, the calculation of $G(\tau)$ takes place within a causal inference framework, as introduced in Pearl (2013) and Runge et al. (2015b), and corresponds to the "total causal effect" metric described in Kaufman and Feldl (2022).

After uncovering each variable's causal predictors with PCMCI, we quantify causal effects using a VAR model:

$$\mathbf{X}(t) = \sum_{\tau=1}^{\tau_{\max}} \Phi(\tau)\mathbf{X}(t-\tau) + \epsilon_t \tag{4.5}$$

where $\mathbf{X}$ is a vector of shape (N, t) containing time series for N variables, Φ is a standardized regression coefficient matrix of shape $(N, N, \tau_{\max})$, and ϵ_t are independent, identically distributed error terms, which describe the uncorrelated probability distributions of each causal network variable's anomalies. An individual regression coefficient, or link coefficient, $\Phi_{j,i}(\tau)$, indicates the expected change in variable $X_j(t)$

caused by a hypothetical 1σ perturbation in $X_i(t-\tau)$ with all other variables held constant. $\tau_{\max}$ refers to the time domain over which link coefficients are added. Importantly, $\Phi_{j,i}(\tau) = 0$ unless $X_i(t-\tau)$ causes $X_j(t)$, as determined by PCMCI. This key feature of matrix Φ frees the VAR model from having to fit negligible parameters, thus allowing it to accommodate a large number of variables and time lags.

The causal inference framework also allows us to account for coupled interactions modulating the responses to a step change in a causal network variable. The full set of climate response functions associated with the causal network, $\mathbf{G}(\tau)$ is found by multiplying the link coefficient matrices ($\Phi(\tau)$) in Equation 4.5:

$$\mathbf{G}(\tau) = \sum_{s=1}^{\tau} \Phi(s)\mathbf{G}(\tau - s). \tag{4.6}$$

Note that Equation 4.6 shown above is equivalent to Equation 3.6 in Chapter 3, except total causal effect ($\mathbf{TCE}(\tau)$) is redefined as $\mathbf{G}(\tau)$ to emphasize its mathematical resemblance to Green's functions, which is relevant for the linear convolutions conducted in Section 4.4. $\mathbf{G}(\tau)$ can be further decomposed into Green's functions for individual pairs of driver and response variables, which is accomplished by restricting Φ to the specific causal pathways that connect them. In Section 4.4, we isolate Green's functions for the Eurasian temperature and Barents-Kara sea-ice response to a Ural sea-level pressure anomaly (Fig. 4.3a,b).

Chapter 5

Executive Summary

In this thesis, I present works that advance scientific understanding of sea ice and its central role in governing polar climate variability and change. In Chapter Two, I use a high-resolution preindustrial control simulation to describe how multidecadal Southern Ocean climate variability depends on deep convection and open-ocean polynya formation in the Weddell Sea. In Chapter Three, I highlight sea ice's dominant role in shaping the vertical structure of Arctic atmospheric warming in comprehensive climate change simulations. Finally, in Chapter Four, I explore the dynamical connections between Arctic warming and midlatitude climate, reconciling key differences between models and observations over the historical period. These studies reveal the fascinating, complex interactions between atmosphere, ocean, and sea ice that shape the spatial pattern of anthropogenic trends.

Throughout this PhD, my research on polar climate has been propelled by an interest in causal discovery techniques, particularly those based on the statistical theories of Clive Granger and Judea Pearl. Until recently, such data-driven approaches have been seldom used in climate science. However, they've enabled me

to address some of the central challenges in my field of study. Today's climate scientists face a situation where large-scale experiments on the real-world Earth system are unethical or impractical; at the same time, climate models of varying complexity present inevitable tradeoffs between prediction and understanding, and their ouput is often difficult to compare with observations. By applying causal inference in the context of atmosphere-ocean dynamics, I am able to overcome these barriers. In particular, my integration of causal inference with linear convolution theory (Chapter Four) is a novel contribution that will greatly expand the applicability of the category of research tools that includes climate response functions.

The work in this thesis has opened an array of new research questions. For instance, I found that deep convection is an important driver of Southern Ocean variability in a preindustrial climate simulation (Chapter Two), but it remains unclear how deep convection, and Southern Ocean circulation in general, will respond to future anthropogenic changes. My upcoming research will investigate how anthropogenic freshwater fluxes from the Antarctic ice sheet alter the density stratification of the Southern Ocean. These changes may impede deep convection, with important implications for the trajectory of projected Southern Hemisphere sea ice and temperature trends. The methodological tools developed throughout my PhD will be essential for investigating these topics.

Meanwhile, in the Arctic, I show that sea-ice loss can decrease the stable stratification that typically characterizes Arctic boundary-layer climatology in winter, increasing surface-atmosphere coupling (Chapter Three). As this sea-ice loss continues, the new Arctic climate regime may feature new phenomena that would not be possible today, such as polar convective thunderstorms, which are thought

to have occurred in earlier warm periods of Earth's geologic history. In addition, I show that sea-ice loss plays a minimal role in driving cold-air outbreaks over midlatitude continents, suggesting that events like the 1988-2012 Eurasian cooling trend will becoming increasingly unlikely in a warming world (Chapter Four). As the observational record of climate change continues to grow, new opportunities will arise to test the robustness of these interpretations, enabling me to continue advancing our scientific understanding of sea ice's role in the climate system.

Bibliography

Alexeev, V., P. L. Langen, and J. R. Bates (2005). "Polar amplification of surface warming on an aquaplanet in "ghost forcing" experiments without sea ice feedbacks". In: *Climate Dynamics* 24.7-8, pp. 655–666.

Armour, K. C. and C. M. Bitz (2015). "Observed and projected trends in Antarctic sea ice". In: *US CLIVAR Variations* 13, pp. 12–19.

Armour, K. C., J. Marshall, J. R. Scott, A. Donohoe, and E. R. Newsom (2016). "Southern Ocean warming delayed by circumpolar upwelling and equatorward transport". In: *Nature Geoscience* 9.7, p. 549.

Armour, K. C., N. Siler, A. Donohoe, and G. H. Roe (2019). "Meridional atmospheric heat transport constrained by energetics and mediated by large-scale diffusion". In: *Journal of Climate* 32.12, pp. 3655–3680.

Arrhenius, S. (1896). "XXXI. On the influence of carbonic acid in the air upon the temperature of the ground". In: *The London, Edinburgh, and Dublin Philosophical Magazine and Journal of Science* 41.251, pp. 237–276.

Auclair, G. and L. B. Tremblay (2018). "The role of ocean heat transport in rapid sea ice declines in the Community Earth System Model Large Ensemble". In: *Journal of Geophysical Research: Oceans* 123.12, pp. 8941–8957.

Baggett, C. and S. Lee (2017). "An identification of the mechanisms that lead to Arctic warming during planetary-scale and synoptic-scale wave life cycles". In: *Journal of the Atmospheric Sciences* 74.6, pp. 1859–1877.

Baggett, C., S. Lee, and S. Feldstein (2016). "An investigation of the presence of atmospheric rivers over the North Pacific during planetary-scale wave life cycles and their role in Arctic warming". In: *Journal of the Atmospheric Sciences* 73.11, pp. 4329–4347.

Barnes, E. A. and J. A. Screen (2015). "The impact of Arctic warming on the midlatitude jet-stream: Can it? Has it? Will it?" In: *Wiley Interdisciplinary Reviews: Climate Change* 6.3, pp. 277–286.

Barton, N. P., S. A. Klein, J. S. Boyle, and Y. Y. Zhang (2012). "Arctic synoptic regimes: Comparing domain-wide Arctic cloud observations with CAM4 and CAM5 during similar dynamics". In: *Journal of Geophysical Research: Atmospheres* 117.D15.

Benjamini, Y. and Y. Hochberg (1995). "Controlling the false discovery rate: a practical and powerful approach to multiple testing". In: *Journal of the Royal statistical society: series B (Methodological)* 57.1, pp. 289–300.

Bintanja, R, R. Graversen, and W Hazeleger (2011). "Arctic winter warming amplified by the thermal inversion and consequent low infrared cooling to space". In: *Nature Geoscience* 4.11, pp. 758–761.

Bintanja, R, E. Van der Linden, and W Hazeleger (2012). "Boundary layer stability and Arctic climate change: A feedback study using EC-Earth". In: *Climate dynamics* 39.11, pp. 2659–2673.

Bintanja, R, G. Van Oldenborgh, and C. Katsman (2015). "The effect of increased fresh water from Antarctic ice shelves on future trends in Antarctic sea ice". In: *Annals of Glaciology* 56.69, pp. 120–126.

Bintanja, R. and E. Van der Linden (2013). "The changing seasonal climate in the Arctic". In: *Scientific reports* 3.1, pp. 1–8.

Bjerknes, J (1964). "Atlantic air-sea interaction". In: *Advances in geophysics* 10, pp. 1–82.

Blackport, R. and J. A. Screen (2020). "Weakened evidence for mid-latitude impacts of Arctic warming". In: *Nature Climate Change* 10.12, pp. 1065–1066.

— (2021). "Observed statistical connections overestimate the causal effects of Arctic sea ice changes on midlatitude winter climate". In: *Journal of Climate* 34.8, pp. 3021–3038.

Boeke, R. C. and P. C. Taylor (2018). "Seasonal energy exchange in sea ice retreat regions contributes to differences in projected Arctic warming". In: *Nature communications* 9.1, pp. 1–14.

Boeke, R. C., P. C. Taylor, and S. A. Sejas (2020). "On the Nature of the Arctic's Positive Lapse-rate Feedback". In: *Geophysical Research Letters*, e2020GL091109.

Boland, E. J., T. J. Bracegirdle, and E. F. Shuckburgh (2017). "Assessment of sea ice-atmosphere links in CMIP5 models". In: *Climate Dynamics* 49.1, pp. 683–702.

Cabré, A., I. Marinov, and A. Gnanadesikan (2017). "Global atmospheric teleconnections and multidecadal climate oscillations driven by Southern Ocean convection". In: *Journal of Climate* 30.20, pp. 8107–8126.

Campbell, E. C., E. A. Wilson, G. W. K. Moore, S. C. Riser, C. E. Brayton, M. R. Mazloff, and L. D. Talley (2019). "Antarctic offshore polynyas linked to Southern Hemisphere climate anomalies". In: *Nature* 570.1476-4687.

Cardinale, C. J., B. E. Rose, A. L. Lang, and A. Donohoe (2021). "Stratospheric and Tropospheric Flux Contributions to the Polar Cap Energy Budgets". In: *Journal of Climate* 34.11, pp. 4261–4278.

Carsey, F. (1980). "Microwave observation of the Weddell Polynya". In: *Monthly Weather Review* 108.12, pp. 2032–2044.

Cheon, W. G., C.-B. Cho, A. L. Gordon, Y. H. Kim, and Y.-G. Park (2018). "The Role of Oscillating Southern Hemisphere Westerly Winds: Southern Ocean Coastal and Open-Ocean Polynyas". In: *Journal of Climate* 31.3, pp. 1053–1073.

Cheon, W. G. and A. L. Gordon (2019). "Open-ocean polynyas and deep convection in the Southern Ocean". In: *Scientific reports* 9.1, p. 6935.

Cheon, W. G., Y.-G. Park, J. Toggweiler, and S.-K. Lee (2014). "The relationship of Weddell Polynya and open-ocean deep convection to the Southern Hemisphere westerlies". In: *Journal of Physical Oceanography* 44.2, pp. 694–713.

Chung, E.-S., K.-J. Ha, A. Timmermann, M. F. Stuecker, T. Bodai, and S.-K. Lee (2021). "Cold-season Arctic amplification driven by Arctic ocean-mediated seasonal energy transfer". In: *Earth's Future* 9.2, e2020EF001898.

Cohen, J., X. Zhang, J. Francis, T Jung, R Kwok, J Overland, T. Ballinger, U. Bhatt, H. Chen, D. Coumou, et al. (2020). "Divergent consensuses on Arc-

tic amplification influence on midlatitude severe winter weather". In: *Nature Climate Change* 10.1, pp. 20–29.

Cronin, T. W. and M. F. Jansen (2016). "Analytic radiative-advective equilibrium as a model for high-latitude climate". In: *Geophysical Research Letters* 43.1, pp. 449–457.

Curry, J. A., J. L. Schramm, W. B. Rossow, and D. Randall (1996). "Overview of Arctic cloud and radiation characteristics". In: *Journal of Climate* 9.8, pp. 1731–1764.

Dai, A., D. Luo, M. Song, and J. Liu (Dec. 2019). "Arctic amplification is caused by sea-ice loss under increasing CO2". en. In: *Nature Communications* 10.1, p. 121. ISSN: 2041-1723.

De Lavergne, C., J. B. Palter, E. D. Galbraith, R. Bernardello, and I. Marinov (2014). "Cessation of deep convection in the open Southern Ocean under anthropogenic climate change". In: *Nature Climate Change* 4.4, p. 278.

Deser, C., L. Sun, R. A. Tomas, and J. Screen (2016). "Does ocean coupling matter for the northern extratropical response to projected Arctic sea ice loss?" In: *Geophysical Research Letters* 43.5, pp. 2149–2157.

Deser, C., R. Tomas, M. Alexander, and D. Lawrence (2010). "The seasonal atmospheric response to projected Arctic sea ice loss in the late twenty-first century". In: *Journal of Climate* 23.2, pp. 333–351.

Ding, Q., J. M. Wallace, D. S. Battisti, E. J. Steig, A. J. Gallant, H.-J. Kim, and L. Geng (2014). "Tropical forcing of the recent rapid Arctic warming in northeastern Canada and Greenland". In: *Nature* 509.7499, pp. 209–212.

Dong, Y., C. Proistosescu, K. C. Armour, and D. S. Battisti (2019). "Attributing historical and future evolution of radiative feedbacks to regional warming patterns using a Green's function approach: The preeminence of the western Pacific". In: *Journal of Climate* 32.17, pp. 5471–5491.

Dufour, A., O. Zolina, and S. K. Gulev (2016). "Atmospheric moisture transport to the Arctic: Assessment of reanalyses and analysis of transport components". In: *Journal of Climate* 29.14, pp. 5061–5081.

Duncan, B. N., L. E. Ott, J. B. Abshire, L. Brucker, M. L. Carroll, J. Carton, J. C. Comiso, E. P. Dinnat, B. C. Forbes, A. Gonsamo, et al. (2020). "Space-based observations for understanding changes in the Arctic-Boreal Zone". In: *Reviews of Geophysics* 58.1, e2019RG000652.

Durack, P. J., S. E. Wijffels, and R. J. Matear (2012). "Ocean salinities reveal strong global water cycle intensification during 1950 to 2000". In: *science* 336.6080, pp. 455–458.

England, M. R., I. Eisenman, N. J. Lutsko, and T. J. Wagner (2021). "The recent emergence of Arctic Amplification". In: *Geophysical Research Letters* 48.15, e2021GL094086.

Fan, T., C. Deser, and D. P. Schneider (2014). "Recent Antarctic sea ice trends in the context of Southern Ocean surface climate variations since 1950". In: *Geophysical Research Letters* 41.7, pp. 2419–2426.

Feldl, N., S. Po-Chedley, H. K. Singh, S. Hay, and P. J. Kushner (2020). "Sea ice and atmospheric circulation shape the high-latitude lapse rate feedback". In: *npj Climate and Atmospheric Science* 3.1, pp. 1–9.

Feldl, N., S. Bordoni, and T. M. Merlis (2017a). "Coupled high-latitude climate feedbacks and their impact on atmospheric heat transport". In: *Journal of Climate* 30.1, pp. 189–201.

Feldl, N., B. T. Anderson, and S. Bordoni (2017b). "Atmospheric eddies mediate lapse rate feedback and Arctic amplification". In: *Journal of Climate* 30.22, pp. 9213–9224.

Francis, D., C. Eayrs, J. Cuesta, and D. Holland (2018). "Polar cyclones at the origin of the reoccurrence of the Maud Rise Polynya in austral winter 2017". In: *Journal of Geophysical Research: Atmospheres*.

Francis, J. A. and S. J. Vavrus (2012). "Evidence linking Arctic amplification to extreme weather in mid-latitudes". In: *Geophysical research letters* 39.6.

— (2015). "Evidence for a wavier jet stream in response to rapid Arctic warming". In: *Environmental Research Letters* 10.1, p. 014005.

Gelaro, R., W. McCarty, M. J. Suárez, R. Todling, A. Molod, L. Takacs, C. A. Randles, A. Darmenov, M. G. Bosilovich, R. Reichle, et al. (2017). "The modern-era retrospective analysis for research and applications, version 2 (MERRA-2)". In: *Journal of climate* 30.14, pp. 5419–5454.

Gong, T., S. Feldstein, and S. Lee (2017). "The role of downward infrared radiation in the recent Arctic winter warming trend". In: *Journal of Climate* 30.13, pp. 4937–4949.

Gong, T. and D. Luo (2017). "Ural blocking as an amplifier of the Arctic sea ice decline in winter". In: *Journal of Climate* 30.7, pp. 2639–2654.

Gordon, A. L. (1982). "Weddell deep water variability". In: *Journal of Marine Research* 40, pp. 199–217.

Gordon, A. L., M. Visbeck, and J. C. Comiso (2007). "A Possible Link between the Weddell Polynya and the Southern Annular Mode". In: *Journal of Climate* 20.11, pp. 2558–2571.

Graversen, R. G. and M. Burtu (2016). "Arctic amplification enhanced by latent energy transport of atmospheric planetary waves". In: *Quarterly Journal of the Royal Meteorological Society* 142.698, pp. 2046–2054.

Graversen, R. G. and P. L. Langen (2019). "On the Role of the Atmospheric Energy Transport in 2× CO_2-Induced Polar Amplification in CESM1". In: *Journal of Climate* 32.13, pp. 3941–3956.

Graversen, R. G., P. L. Langen, and T. Mauritsen (2014a). "Polar amplification in CCSM4: Contributions from the lapse rate and surface albedo feedbacks". In: *Journal of Climate* 27.12, pp. 4433–4450.

Graversen, R. G., P. L. Langen, and T. Mauritsen (June 2014b). "Polar Amplification in CCSM4: Contributions from the Lapse Rate and Surface Albedo Feedbacks". en. In: *Journal of Climate* 27.12, pp. 4433–4450. ISSN: 0894-8755, 1520-0442.

Graversen, R. G. and M. Wang (2009). "Polar amplification in a coupled climate model with locked albedo". In: *Climate Dynamics* 33.5, pp. 629–643.

Hahn, L., K. C. Armour, D. S. Battisti, A. Donohoe, A. Pauling, and C. Bitz (2020). "Antarctic elevation drives hemispheric asymmetry in polar lapse rate climatology and feedback". In: *Geophysical Research Letters* 47.16, e2020GL088965.

He, S., X. Xu, T. Furevik, and Y. Gao (2020). "Eurasian cooling linked to the vertical distribution of Arctic warming". In: *Geophysical Research Letters* 47.10, e2020GL087212.

Held, I. M. and B. J. Soden (2006). "Robust responses of the hydrological cycle to global warming". In: *Journal of climate* 19.21, pp. 5686–5699.

Henry, M., T. M. Merlis, N. J. Lutsko, and B. E. Rose (2021). "Decomposing the Drivers of Polar Amplification with a Single-Column Model". In: *Journal of Climate* 34.6, pp. 2355–2365.

Heuzé, C., K. J. Heywood, D. P. Stevens, and J. K. Ridley (2013). "Southern Ocean bottom water characteristics in CMIP5 models". In: *Geophysical Research Letters* 40.7, pp. 1409–1414.

Holland, D. (2001). "Explaining the Weddell Polynya–a large ocean eddy shed at Maud Rise". In: *Science* 292.5522, pp. 1697–1700.

Holland, M. M. and C. M. Bitz (2003). "Polar amplification of climate change in coupled models". In: *Climate Dynamics* 21.3-4, pp. 221–232.

Honda, M., J. Inoue, and S. Yamane (2009). "Influence of low Arctic sea-ice minima on anomalously cold Eurasian winters". In: *Geophysical Research Letters* 36.8.

Hwang, Y.-T., D. M. Frierson, and J. E. Kay (2011). "Coupling between Arctic feedbacks and changes in poleward energy transport". In: *Geophysical Research Letters* 38.17.

Jena, B, M Ravichandran, and J Turner (2019). "Recent reoccurrence of large open-ocean polynya on the Maud Rise Seamount". In: *Geophysical Research Letters* 46.8, pp. 4320–4329.

Kaufman, Z. S. and N. Feldl (2022). "Causes of the Arctic's Lower-Tropospheric Warming Structure". In: *Journal of Climate* 35.6, pp. 1983–2002.

Kaufman, Z. S., N. Feldl, W. Weijer, and M. Veneziani (2020). "Causal interactions between Southern Ocean polynyas and high-latitude atmosphere–ocean variability". In: *Journal of Climate* 33.11, pp. 4891–4905.

Kay, J. E., C. Deser, A Phillips, A Mai, C. Hannay, G. Strand, J. M. Arblaster, S. Bates, G. Danabasoglu, J. Edwards, et al. (2015). "The Community Earth System Model (CESM) Large Ensemble Project: a Community Resource for Studying Climate Change in the Presence of Internal Climate Variability". In: *Bulletin of the American Meteorological Society* 96.8, pp. 1333–1349.

Kay, J. E. and A. Gettelman (2009). "Cloud influence on and response to seasonal Arctic sea ice loss". In: *Journal of Geophysical Research: Atmospheres* 114.D18.

Kim, B.-M., S.-W. Son, S.-K. Min, J.-H. Jeong, S.-J. Kim, X. Zhang, T. Shim, and J.-H. Yoon (2014). "Weakening of the stratospheric polar vortex by Arctic sea-ice loss". In: *Nature communications* 5.1, pp. 1–8.

Kim, D., S. M. Kang, Y. Shin, and N. Feldl (2018). "Sensitivity of polar amplification to varying insolation conditions". In: *Journal of Climate* 31.12, pp. 4933–4947.

Kostov, Y., D. Ferreira, K. C. Armour, and J. Marshall (2018). "Contributions of greenhouse gas forcing and the southern annular mode to historical southern ocean surface temperature trends". In: *Geophysical Research Letters* 45.2, pp. 1086–1097.

Kostov, Y., J. Marshall, U. Hausmann, K. C. Armour, D. Ferreira, and M. M. Holland (2017). "Fast and slow responses of Southern Ocean sea surface temperature to SAM in coupled climate models". In: *Climate Dynamics* 48.5-6, pp. 1595–1609.

Kretschmer, M., D. Coumou, J. F. Donges, and J. Runge (2016). "Using causal effect networks to analyze different Arctic drivers of midlatitude winter circulation". In: *Journal of Climate* 29.11, pp. 4069–4081.

Kretschmer, M., G. Zappa, and T. G. Shepherd (2020). "The role of Barents–Kara sea ice loss in projected polar vortex changes". In: *Weather and Climate Dynamics* 1.2, pp. 715–730.

Kurtakoti, P., M. Veneziani, A. Stössel, and W. Weijer (2018). "Preconditioning and Formation of Maud Rise Polynyas in a High-Resolution Earth System Model". In: *Journal of Climate* 31.23, pp. 9659–9678.

Labe, Z., Y. Peings, and G. Magnusdottir (2020). "Warm Arctic, cold Siberia pattern: Role of full Arctic amplification versus sea ice loss alone". In: *Geophysical Research Letters* 47.17, e2020GL088583.

Latif, M., T. Martin, and W. Park (2013). "Southern Ocean sector centennial climate variability and recent decadal trends". In: *Journal of Climate* 26.19, pp. 7767–7782.

Lee, S. (2012). "Testing of the tropically excited Arctic warming mechanism (TEAM) with traditional El Niño and La Niña". In: *Journal of Climate* 25.12, pp. 4015–4022.

Lee, S., T. Gong, S. B. Feldstein, J. A. Screen, and I. Simmonds (2017). "Revisiting the cause of the 1989-2009 Arctic surface warming using the surface energy

budget: Downward infrared radiation dominates the surface fluxes". In: *Geophysical Research Letters* 44.20, pp. 10–654.

Liang, Y.-c., Y.-O. Kwon, C. Frankignoul, G. Danabasoglu, S. Yeager, A. Cherchi, Y. Gao, G. Gastineau, R. Ghosh, D. Matei, et al. (2020). "Quantification of the Arctic sea ice-driven atmospheric circulation variability in coordinated large ensemble simulations". In: *Geophysical research letters* 47.1, e2019GL085397.

Liu, C. and E. A. Barnes (2015). "Extreme moisture transport into the Arctic linked to Rossby wave breaking". In: *Journal of Geophysical Research: Atmospheres* 120.9, pp. 3774–3788.

Liu, Z., C. Risi, F. Codron, Z. Jian, Z. Wei, X. He, C. J. Poulsen, Y. Wang, D. Chen, W. Ma, et al. (2022). "Atmospheric forcing dominates winter Barents-Kara sea ice variability on interannual to decadal time scales". In: *Proceedings of the National Academy of Sciences* 119.36, e2120770119.

Lu, J. and M. Cai (2009). "Seasonality of polar surface warming amplification in climate simulations". In: *Geophysical Research Letters* 36.16.

Luo, B., D. Luo, L. Wu, L. Zhong, and I. Simmonds (2017). "Atmospheric circulation patterns which promote winter Arctic sea ice decline". In: *Environmental Research Letters* 12.5, p. 054017.

Luo, D., Y. Xiao, Y. Yao, A. Dai, I. Simmonds, and C. L. Franzke (2016). "Impact of Ural blocking on winter warm Arctic–cold Eurasian anomalies. Part I: Blocking-induced amplification". In: *Journal of Climate* 29.11, pp. 3925–3947.

Manabe, S. and R. J. Stouffer (1980). "Sensitivity of a global climate model to an increase of CO_2 concentration in the atmosphere". In: *Journal of Geophysical Research: Oceans* 85.C10, pp. 5529–5554.

Manabe, S. and R. T. Wetherald (1975). "The effects of doubling the CO_2 concentration on the climate of a general circulation model". In: *Journal of the Atmospheric Sciences* 32.1, pp. 3–15.

Marshall, J., K. C. Armour, J. R. Scott, Y. Kostov, U. Hausmann, D. Ferreira, T. G. Shepherd, and C. M. Bitz (July 2014). "The ocean's role in polar climate change: asymmetric Arctic and Antarctic responses to greenhouse gas and ozone forcing". en. In: *Philosophical Transactions of the Royal Society A: Mathematical, Physical and Engineering Sciences* 372.2019, p. 20130040. ISSN: 1364-503X, 1471-2962.

Martin, T., W. Park, and M. Latif (2013). "Multi-centennial variability controlled by Southern Ocean convection in the Kiel Climate Model". In: *Climate dynamics* 40.7-8, pp. 2005–2022.

Masson-Delmotte, V., M. Kageyama, P. Braconnot, S Charbit, G. Krinner, C. Ritz, E Guilyardi, J. Jouzel, A. Abe-Ouchi, M Crucifix, et al. (2006). "Past and future polar amplification of climate change: climate model intercomparisons and ice-core constraints". In: *Climate Dynamics* 26.5, pp. 513–529.

Masson-Delmotte, V., P. Zhai, A. Pirani, S. L. Connors, C. Péan, S. Berger, N. Caud, Y Chen, L Goldfarb, M. Gomis, et al. (2021). "Climate change 2021: the physical science basis". In: *Contribution of working group I to the sixth assessment report of the intergovernmental panel on climate change* 2.

Matthewman, N. J. and G. Magnusdottir (2011). "Observed interaction between Pacific sea ice and the western Pacific pattern on intraseasonal time scales". In: *Journal of Climate* 24.19, pp. 5031–5042.

McGraw, M. C., C. F. Baggett, C. Liu, and B. D. Mundhenk (2020). "Changes in Arctic moisture transport over the North Pacific associated with sea ice loss". In: *Climate Dynamics* 54.1, pp. 491–506.

McGraw, M. C. and E. A. Barnes (2018). "Memory matters: A case for Granger causality in climate variability studies". In: *Journal of Climate* 31.8, pp. 3289–3300.

McIlhattan, E. A., J. E. Kay, and T. S. L'Ecuyer (2020). "Arctic clouds and precipitation in the Community Earth system Model Version 2". In: *Journal of Geophysical Research: Atmospheres* 125.22, e2020JD032521.

Meehl, G. A., J. M. Arblaster, C. T. Chung, M. M. Holland, A. DuVivier, L. Thompson, D. Yang, and C. M. Bitz (2019). "Sustained ocean changes contributed to sudden Antarctic sea ice retreat in late 2016". In: *Nature communications* 10.1, p. 14.

Merlis, T. M. and M. Henry (2018). "Simple estimates of polar amplification in moist diffusive energy balance models". In: *Journal of Climate* 31.15, pp. 5811–5824.

Moore, G., K Alverson, and I. Renfrew (2002). "A reconstruction of the air–sea interaction associated with the Weddell Polynya". In: *Journal of physical oceanography* 32.6, pp. 1685–1698.

Mori, M., Y. Kosaka, M. Watanabe, H. Nakamura, and M. Kimoto (2019). "A reconciled estimate of the influence of Arctic sea-ice loss on recent Eurasian cooling". In: *Nature Climate Change* 9.2, pp. 123–129.

Morrison, A., J. Kay, W. Frey, H Chepfer, and R Guzman (2019). "Cloud response to Arctic Sea ice loss and implications for future feedback in the CESM1 climate model". In: *Journal of Geophysical Research: Atmospheres* 124.2, pp. 1003–1020.

Nishii, K., H. Nakamura, and Y. J. Orsolini (2011). "Geographical dependence observed in blocking high influence on the stratospheric variability through enhancement and suppression of upward planetary-wave propagation". In: *Journal of Climate* 24.24, pp. 6408–6423.

Outten, S., C. Li, M. P. King, L. Suo, P. Y. Siew, R. Davy, E. Dunn-Sigouin, S. He, H. Cheung, E. Madonna, et al. (2022). "Reconciling conflicting evidence for the cause of the observed early 21st century Eurasian cooling". In: *Weather and Climate Dynamics Discussions*, pp. 1–32.

Overland, J., J. A. Francis, R. Hall, E. Hanna, S.-J. Kim, and T. Vihma (2015). "The melting Arctic and midlatitude weather patterns: Are they connected?" In: *Journal of Climate* 28.20, pp. 7917–7932.

Papritz, L. (2020). "Arctic lower-tropospheric warm and cold extremes: Horizontal and vertical transport, diabatic processes, and linkage to synoptic circulation features". In: *Journal of Climate* 33.3, pp. 993–1016.

Park, D.-S. R., S. Lee, and S. B. Feldstein (2015a). "Attribution of the recent winter sea ice decline over the Atlantic sector of the Arctic Ocean". In: *Journal of climate* 28.10, pp. 4027–4033.

Park, H.-S., S. Lee, S.-W. Son, S. B. Feldstein, and Y. Kosaka (2015b). "The impact of poleward moisture and sensible heat flux on Arctic winter sea ice variability". In: *Journal of Climate* 28.13, pp. 5030–5040.

Pearl, J. (2013). "Linear models: a useful microscope for causal analysis". In: *Journal of Causal Inference* 1.1, pp. 155–170.

Pearl, J. et al. (2000). "Models, reasoning and inference". In: *Cambridge, UK: Cambridge University Press*.

Peings, Y (2019). "Ural blocking as a driver of early-winter stratospheric warmings". In: *Geophysical Research Letters* 46.10, pp. 5460–5468.

Peings, Y., Z. M. Labe, and G. Magnusdottir (2021). "Are 100 ensemble members enough to capture the remote atmospheric response to+ 2° C Arctic sea ice loss?" In: *Journal of Climate* 34.10, pp. 3751–3769.

Pithan, F., A. Ackerman, W. M. Angevine, K. Hartung, L. Ickes, M. Kelley, B. Medeiros, I. Sandu, G.-J. Steeneveld, H. A. Sterk, et al. (2016). "Select strengths and biases of models in representing the Arctic winter boundary layer over sea ice: the Larcform 1 single column model intercomparison". In: *Journal of advances in modeling earth systems* 8.3, pp. 1345–1357.

Pithan, F. and T. Mauritsen (Mar. 2014). "Arctic amplification dominated by temperature feedbacks in contemporary climate models". en. In: *Nature Geoscience* 7.3, pp. 181–184. ISSN: 1752-0894, 1752-0908.

Previdi, M., T. P. Janoski, G. Chiodo, K. L. Smith, and L. M. Polvani (2020). "Arctic amplification: A rapid response to radiative forcing". In: *Geophysical Research Letters* 47.17, e2020GL089933.

Purich, A., W. Cai, M. H. England, and T. Cowan (Apr. 2016). "Evidence for link between modelled trends in Antarctic sea ice and underestimated westerly wind changes". en. In: *Nature Communications* 7.1, p. 10409. ISSN: 2041-1723.

Rodgers, K. B., S.-S. Lee, N. Rosenbloom, A. Timmermann, G. Danabasoglu, C. Deser, J. Edwards, J.-E. Kim, I. R. Simpson, K. Stein, et al. (2021). "Ubiquity of human-induced changes in climate variability". In: *Earth System Dynamics* 12.4, pp. 1393–1411.

Roe, G. H., N. Feldl, K. C. Armour, Y.-T. Hwang, and D. M. Frierson (2015). "The remote impacts of climate feedbacks on regional climate predictability". In: *Nature Geoscience* 8.2, pp. 135–139.

Runge, J., S. Bathiany, E. Bollt, G. Camps-Valls, D. Coumou, E. Deyle, C. Glymour, M. Kretschmer, M. D. Mahecha, J. Muñoz-Marí, et al. (2019). "Inferring causation from time series in Earth system sciences". In: *Nature communications* 10.1, pp. 1–13.

Runge, J., P. Nowack, M. Kretschmer, S. Flaxman, and D. Sejdinovic (2017). "Detecting causal associations in large nonlinear time series datasets". In: *arXiv preprint arXiv:1702.07007*.

Runge, J., V. Petoukhov, J. F. Donges, J. Hlinka, N. Jajcay, M. Vejmelka, D. Hartman, N. Marwan, M. Paluš, and J. Kurths (2015a). "Identifying causal gateways and mediators in complex spatio-temporal systems". In: *Nature communications* 6.1, pp. 1–10.

Runge, J., V. Petoukhov, J. F. Donges, J. Hlinka, N. Jajcay, M. Vejmelka, D. Hartman, N. Marwan, M. PaluÅ¡, and J. Kurths (2015b). "Identifying causal

gateways and mediators in complex spatio-temporal systems". en. In: *Nature Communications* 6.1, p. 8502. ISSN: 2041-1723.

Rye, C. D., J. Marshall, M. Kelley, G. Russell, L. S. Nazarenko, Y. Kostov, G. A. Schmidt, and J. Hansen (2020). "Antarctic glacial melt as a driver of recent Southern Ocean climate trends". In: *Geophysical Research Letters* 47.11, e2019GL086892.

Samarasinghe, S., M. McGraw, E. Barnes, and I Ebert-Uphoff (2018). "A study of links between the Arctic and the midlatitude jet stream using Granger and Pearl causality". In: *Environmetrics*, e2540.

Schweiger, A. J., R. W. Lindsay, S. Vavrus, and J. A. Francis (2008). "Relationships between Arctic sea ice and clouds during autumn". In: *Journal of Climate* 21.18, pp. 4799–4810.

Screen, J. A. (2017). "Simulated atmospheric response to regional and pan-Arctic sea ice loss". In: *Journal of Climate* 30.11, pp. 3945–3962.

Screen, J. A., C. Deser, D. M. Smith, X. Zhang, R. Blackport, P. J. Kushner, T. Oudar, K. E. McCusker, and L. Sun (2018). "Consistency and discrepancy in the atmospheric response to Arctic sea-ice loss across climate models". In: *Nature Geoscience* 11.3, pp. 155–163.

Serreze, M. C., A. P. Barrett, A. G. Slater, M. Steele, J. Zhang, and K. E. Trenberth (2007a). "The large-scale energy budget of the Arctic". In: *Journal of Geophysical Research: Atmospheres* 112.D11.

Serreze, M. C., M. M. Holland, and J. Stroeve (2007b). "Perspectives on the Arctic's shrinking sea-ice cover". In: *science* 315.5818, pp. 1533–1536.

Serreze, M., A. Barrett, J. Stroeve, D. Kindig, and M. Holland (2009). "The emergence of surface-based Arctic amplification". In: *The Cryosphere* 3.1, p. 11.

Siew, P. Y. F., C. Li, S. P. Sobolowski, and M. P. King (2020). "Intermittency of Arctic–mid-latitude teleconnections: stratospheric pathway between autumn sea ice and the winter North Atlantic Oscillation". In: *Weather and Climate Dynamics* 1.1, pp. 261–275.

Singh, H. K., C. M. Bitz, A. Donohoe, and P. J. Rasch (2017). "A source-receptor perspective on the polar hydrologic cycle: Sources, seasonality, and Arctic-Antarctic parity in the hydrologic cycle response to CO_2 doubling". In: *Journal of Climate* 30.24, pp. 9999–10017.

Small, R. J., J. Bacmeister, D. Bailey, A. Baker, S. Bishop, F. Bryan, J. Caron, J. Dennis, P. Gent, H.-m. Hsu, et al. (2014). "A new synoptic scale resolving global climate simulation using the Community Earth System Model". In: *Journal of Advances in Modeling Earth Systems* 6.4, pp. 1065–1094.

Smedsrud, L. H. (2005). "Warming of the deep water in the Weddell Sea along the Greenwich meridian: 1977–2001". In: *Deep Sea Research Part I: Oceanographic Research Papers* 52.2, pp. 241–258.

Smith, D. M., J. A. Screen, C. Deser, J. Cohen, J. C. Fyfe, J. García-Serrano, T. Jung, V. Kattsov, D. Matei, R. Msadek, et al. (2019). "The Polar Amplification Model Intercomparison Project (PAMIP) contribution to CMIP6: Investigating the causes and consequences of polar amplification". In: *Geoscientific Model Development* 12.3, pp. 1139–1164.

Spensberger, C., M. J. Reeder, T. Spengler, and M. Patterson (2020). "The Connection between the Southern Annular Mode and a Feature-Based Perspective

on Southern Hemisphere Midlatitude Winter Variability". In: *Journal of Climate* 33.1, pp. 115–129.

Spirtes, P., C. N. Glymour, R. Scheines, and D. Heckerman (2000). *Causation, Prediction, and Search*. MIT press.

Stössel, A., D. Notz, F. A. Haumann, H. Haak, J. Jungclaus, and U. Mikolajewicz (2015). "Controlling high-latitude Southern Ocean convection in climate models". In: *Ocean Modelling* 86, pp. 58–75.

Stramler, K., A. D. Del Genio, and W. B. Rossow (2011). "Synoptically driven Arctic winter states". In: *Journal of Climate* 24.6, pp. 1747–1762.

Stuecker, M. F., C. M. Bitz, K. C. Armour, C. Proistosescu, S. M. Kang, S.-P. Xie, D. Kim, S. McGregor, W. Zhang, S. Zhao, et al. (2018). "Polar amplification dominated by local forcing and feedbacks". In: *Nature Climate Change* 8.12, pp. 1076–1081.

Sun, L., C. Deser, and R. A. Tomas (2015). "Mechanisms of stratospheric and tropospheric circulation response to projected Arctic sea ice loss". In: *Journal of Climate* 28.19, pp. 7824–7845.

Sun, L., J. Perlwitz, and M. Hoerling (2016). "What caused the recent "Warm Arctic, Cold Continents" trend pattern in winter temperatures?" In: *Geophysical Research Letters* 43.10, pp. 5345–5352.

Tan, I. and T. Storelvmo (2019). "Evidence of strong contributions from mixed-phase clouds to Arctic climate change". In: *Geophysical Research Letters* 46.5, pp. 2894–2902.

Taylor, P. C., R. C. Boeke, L. N. Boisvert, N. Feldl, M. Henry, Y. Huang, P. Langen, W. Liu, F. Pithan, S. Sejas, et al. (2021). "Process drivers, inter-model spread, and the path forward: A review of amplified Arctic warming". In.

Tomas, R. A., C. Deser, and L. Sun (2016). "The role of ocean heat transport in the global climate response to projected Arctic sea ice loss". In: *Journal of Climate* 29.19, pp. 6841–6859.

Trenberth, K. E. and J. M. Caron (2001). "Estimates of meridional atmosphere and ocean heat transports". In: *Journal of Climate* 14.16, pp. 3433–3443.

Turner, D., M. Shupe, and A. Zwink (2018). "Characteristic atmospheric radiative heating rate profiles in Arctic clouds as observed at Barrow, Alaska". In: *Journal of Applied Meteorology and Climatology* 57.4, pp. 953–968.

Turner, J. and J. Comiso (2017). "Solve Antarctica's sea-ice puzzle". In: *Nature News* 547.7663, p. 275.

Vargas Zeppetello, L., A Donohoe, and D. Battisti (2019). "Does surface temperature respond to or determine downwelling longwave radiation?" In: *Geophysical Research Letters* 46.5, pp. 2781–2789.

Wang, G., H. H. Hendon, J. M. Arblaster, E.-P. Lim, S Abhik, and P. van Rensch (2019). "Compounding tropical and stratospheric forcing of the record low Antarctic sea-ice in 2016". In: *Nature communications* 10.1, p. 13.

Weijer, W., M. Veneziani, A. Stössel, M. W. Hecht, N. Jeffery, A. Jonko, T. Hodos, and H. Wang (2017). "Local atmospheric response to an open-ocean polynya in a high-resolution climate model". In: *Journal of Climate* 30.5, pp. 1629–1641.

Winton, M. (2006). "Amplified Arctic climate change: What does surface albedo feedback have to do with it?" In: *Geophysical Research Letters* 33.3.

Woods, C. and R. Caballero (2016a). "The role of moist intrusions in winter Arctic warming and sea ice decline". In: *Journal of Climate* 29.12, pp. 4473–4485.

— (June 2016b). "The Role of Moist Intrusions in Winter Arctic Warming and Sea Ice Decline". en. In: *Journal of Climate* 29.12, pp. 4473–4485. ISSN: 0894-8755, 1520-0442.

Woods, C., R. Caballero, and G. Svensson (2013). "Large-scale circulation associated with moisture intrusions into the Arctic during winter". In: *Geophysical Research Letters* 40.17, pp. 4717–4721.

Yao, Y., D. Luo, A. Dai, and I. Simmonds (2017). "Increased quasi stationarity and persistence of winter Ural blocking and Eurasian extreme cold events in response to Arctic warming. Part I: Insights from observational analyses". In: *Journal of Climate* 30.10, pp. 3549–3568.

Yoshimori, M., A. Abe-Ouchi, and A. Laîné (2017). "The role of atmospheric heat transport and regional feedbacks in the Arctic warming at equilibrium". In: *Climate Dynamics* 49.9-10, pp. 3457–3472.

Zelinka, M. D., S. A. Klein, and D. L. Hartmann (2012). "Computing and partitioning cloud feedbacks using cloud property histograms. Part II: Attribution to changes in cloud amount, altitude, and optical depth". In: *Journal of Climate* 25.11, pp. 3736–3754.

Zelinka, M. D., T. A. Myers, D. T. McCoy, S. Po-Chedley, P. M. Caldwell, P. Ceppi, S. A. Klein, and K. E. Taylor (2020). "Causes of higher climate sensitivity in CMIP6 models". In: *Geophysical Research Letters* 47.1, e2019GL085782.